Precision Calculations for Dark Matter Searches in Supersymmetry and in Simplified Models

Dissertation

der Mathematisch-Naturwissenschaftlichen Fakultät

der Eberhard Karls Universität Tübingen

zur Erlangung des Grades eines

Doktors der Naturwissenschaften

(Dr. rer. nat.)

vorgelegt von

Gabriele Coniglio

aus Palermo/Italien

Tübingen

2021

Gedruckt mit Genehmigung der Mathematisch-Naturwissenschaftlichen Fakultät der Eberhard Karls Universität Tübingen.

Tag der mündlichen Qualifikation:	13.12.2021
Dekan:	Prof. Dr. Thilo Stehle
1. Berichterstatterin:	Prof. Dr. Barbara Jäger
2. Berichterstatter:	Prof. Dr. Werner Vogelsang

Abstract

The study of physics beyond the Standard Model is one of the main focuses of particle physics, in which many questions remain unanswered and none of the proposed solutions has emerged as the most probable. Confirming or disproving whether a model is realised in nature requires a precise study of its phenomenology. In quantum field theory, such calculations are often performed using perturbative techniques. The high degree of precision necessary to assess the correctness of the predictions of a given model means, in this context, taking into account higher-order corrections in the interaction in consideration.

In this thesis, we calculate next-to-leading order corrections in the strong coupling (or NLO-QCD corrections, from quantum chromodynamics) for several processes in the context of supersymmetry and dark matter searches.

We calculate NLO-QCD corrections to the weakino-squark production processes in the Minimal Supersymmetrical Standard Model (MSSM), including the subtraction of the on-shell resonances appearing in the real emission corrections to this process. We match the fixed-order calculation to the parton-shower (PS) program `PYTHIA` using the `POWHEG` method. We can therefore calculate the NLO-QCD cross sections including PS effects for these processes and generate differential distributions at the NLO+PS level. These processes are responsible for interesting experimental signatures, like hard jets and large quantities of missing transverse momentum. Our code will be publicly available for future phenomenological and experimental studies.

Additionally, we study the phenomenology of dark matter pair-production processes at hadron colliders in the context of simplified models, studying the similarity between these processes and the production of neutralino-pairs in the MSSM. We perform this comparison at NLO-QCD accuracy, exploring a vaste range of supersymmetric scenarios. Simplified models are often interpreted as low-energy limits of a UV-complete theory, and we aim at understanding to what extent an s- and a t-channel model are able to reproduce the phenomenology of the far more complex MSSM.

We also investigate the same simplified models for dark matter in a completely different scenario, namely direct detection experiments. We calculate NLO-QCD corrections in the non-relativistic regime and match our results to the Wilson coefficients and operators of an effective field theory, to express our results in the terms generally used for experimental results in direct dark matter searches. We then perform a phenomenological study, comparing the limits set in collider searches and the ones set by the direct detection experiments CRESST and XENON.

Zusammenfassung

Die Erforschung der Physik jenseits des Standardmodells ist einer der Schwerpunkte der Teilchenphysik, bei der viele Fragen unbeantwortet bleiben und keine der vorgeschlagenen Lösungen sich als die wahrscheinlichste herausgestellt hat. Um zu bestätigen oder zu widerlegen, dass ein Modell in der Natur realisiert ist, ist eine genaue Untersuchung seiner Phänomenologie erforderlich. In der Quantenfeldtheorie werden solche Berechnungen häufig mit störungstheoretischen Methoden durchgeführt. Der hohe Präzisionsgrad, der erforderlich ist, um die Korrektheit der Vorhersagen eines bestimmten Modells zu beurteilen, bedeutet in diesem Zusammenhang die Berücksichtigung von Korrekturen höherer Ordnung in der betrachteten Wechselwirkung.

In dieser Arbeit berechnen wir Korrekturen der nächstführenden Ordnung (NLO) der Quantenchromodynamik (QCD) für mehrere Prozesse im Zusammenhang mit der Suche nach Supersymmetrie und dunkler Materie.

Wir berechnen NLO-QCD-Korrekturen für die Weakino-Squark-Produktionsprozesse im Minimalen Supersymmetrischen Standardmodell (MSSM), einschließlich der Subtraktion der On-Shell-Resonanzen, die in den reellen Emissionskorrekturen für diesen Prozess auftreten. Wir passen die Berechnung fester Ordnung an das Parton-Schauer-Programm (PS) `PYTHIA` unter Verwendung der `POWHEG`-Methode an. Wir können daher die NLO-QCD-Wirkungsquerschnitte einschließlich der PS-Effekte für diese Prozesse berechnen und differentielle Verteilungen auf dem NLO+PS-Niveau erzeugen. Diese Prozesse sind für interessante experimentelle Signaturen verantwortlich, wie zum Beispiel das Auftreten von harten Jets in Verbindung mit grossem fehlenden Transversalimpuls. Unser Code wird für zukünftige phänomenologische und experimentelle Studien öffentlich zugänglich sein.

Darüber hinaus untersuchen wir die Phänomenologie von Prozessen der Paarproduktion dunkler Materie an Hadronenbeschleunigern im Kontext vereinfachter Modelle und untersuchen die Ähnlichkeit zwischen diesen Prozessen und der Produktion von Neutralino-Paaren im MSSM. Wir führen diesen Vergleich auf NLO-QCD-Niveau durch und untersuchen eine Vielzahl von supersymmetrischen Szenarien. Vereinfachte Modelle werden oft als Niederenergie-Limits einer UV-kompletten Theorie interpretiert, und wir versuchen zu verstehen, inwieweit ein s- und ein t-Kanal-Modell in der Lage sind, die Phänomenologie des weitaus komplexeren MSSM zu reproduzieren.

Außerdem untersuchen wir die gleichen vereinfachten Modelle für dunkle Materie in einem völlig anderen Szenario, nämlich in Experimenten zum direkten Nachweis. Wir berechnen NLO-QCD-Korrekturen im nichtrelativistischen Bereich und passen unsere Ergebnisse an die Wilson-Koeffizienten und Operatoren einer effektiven Feldtheorie an, um unsere Ergebnisse in einer Form auszudrücken, die im Allgemeinen für experimentelle Ergebnisse bei der direkten Suche verwendet wird. Anschließend führen wir eine phänomenologische Studie durch, in der wir die Grenzwerte der Beschleuniger-Suche mit denen der direkten Nachweisexperimente CRESST und XENON vergleichen.

Contents

Chapter 1

Introduction

The recent history of particle physics is a fascinating one, in which experiments and theory played a complementary role. At times, surprising experimental observations have abruptly pushed our understanding forward: Ernest Rutherford claimed to be shocked by the results of his experiments, that led to the discovery of the atomic nucleus. On other occasions, experiments needed decades of technological advancements to verify theoretical predictions that turned out to be correct, such as the existence of the Higgs boson [1, 2].

Nowadays, a consistent description of the known elementary particles is given by the Standard Model (SM) of particle physics. We know, however, that this picture is not complete. Several phenomena cannot be explained by the SM or a simple extension of it. Among them, the most relevant for this work is the existence of dark matter (DM) [3–10]. Astrophysical observations suggest that DM is far more abundant than ordinary matter in the universe, but its nature remains unknown and it is very likely that it cannot be composed entirely of SM particles. The connection between DM and particle physics is therefore clear: particles that have not yet been observed are the most promising DM candidates. DM is not, however, the only issue that the SM cannot solve [11–17]. A long list of open questions has led to the development of the vast field of beyond the SM physics. One of the best known theories is supersymmetry [18, 19], which could address several of these open questions, including the nature of DM.

In order to test beyond the SM physics theories, including supersymmetry and DM models, it is necessary to have high precision theoretical predictions. Signals have to be distinguished from extremely complicated backgrounds, like in the context of collider searches, or they could be very faint, like in the context of direct searches for DM. The goal of this thesis is to provide accurate predictions for different scenarios concerning beyond the SM physics. We start by considering the production of a pair of two types of supersymmetric particles, namely a weakino and a squark, at hadron colliders. These processes are interesting not only as a test of supersymmetry, but also in the context of DM searches: Weakinos include an interesting DM candidate, the lightest neutralino. In this project, we also develope a ready-to-use tool that can be employed for future experimental and phenomenological studies of these processes. Moreover, we study the phenomenology of DM production in the context of simplified models at hadron colliders and how it compares to the phenomenology of the production of the lightest neutralino in the same context. Finally, we study DM simplified models in the framework of direct detection experiments. Our studies are carried out in the framework of perturbative quantum field theory. In particular, we will perform next-to-leading order (NLO) calculations in quantum chromodynamics (QCD). They are relevant in the context of precision calculations, as truncating the perturbative

expansion at leading order can lead to unreliable estimates of cross sections and large theoretical uncertainties. NLO-QCD corrections often result in a sizeable change in the prediction of production rates and in a sensible reduction of the dependence of the results on artifical parameters.

This thesis is organised as follows: Chapter 2 begins with an overview of the shortcomings of the SM. Afterwards, Supersymmetry as a possible solution to some of them is introduced, with a focus on the Minimal Supersymmetric Standard Model (MSSM). Chapter3 discusses the DM issue, emphasising the most relevant aspects for particle physics. Chapter4, contains a review of the techniques used to perform NLO calculations in quantum field theory. The remaining chapters are dedicated to the presentation of the original research work carried out within this thesis.

Chapter5 discusses our calculation of NLO-QCD corrections for weakino-squark production at hadron colliders [20]. This calculation is performed without any assumption with regard to masses of supersymmetric particles and includes the subtraction of on-shell resonances appearing in the real emission corrections. We also include a short phenomenological study, in which we also match our results to the Monte Carlo parton-shower program `PYTHIA` [21, 22] using the `POWHEG` method as implemented in the `POWHEG-BOX` [23–25].

Our work on DM pair production in the MSSM and in the context of simplified models [26] is presented in Chap. 6. We study whether an s- or a t-channel model can be seen as the low-energy limit of the MSSM and whether they are able to reproduce of neutralino-pair production in the MSSM for proton-proton collision with a centre-of-mass energy of 13 TeV, despite being significantly simpler and having fewer parameters.

Chapter 7 gives an overview of the DM direct detection experiments and discusses our calculation of NLO-QCD corrections for DM in simplified models in this context [27]. We match our results to the Wilson coefficients and operators of an effective field theory, which allows us to discuss our results as they are generally expressed in the framework of direct DM searches. We also perform a phenomenological study, showing the limits set by collider searches and comparing them with those set by the direct detection experiments CRESST [28] and XENON [29], including the case of a combined $s + t$-channel simplified model.

Finally, the conclusions of our work are given in Chap. 8.

Chapter 2

Supersymmetry

The Standard Model (SM) of particle physics is a very successful theory. The entire particle spectrum it predicts has been observed and the particles observed interact, to the current experimental accuracy, according to the SM predictions, including the still recent observation of the long-sought Higgs boson [1, 2]. Nevertheless, particle physics still presents a vast range of open problems that the SM cannot solve. Therefore, several theories for physics beyond the SM (BSM) have been formulated in the last decades. The most relevant of them in the context of this work is supersymmetry (SUSY).

In the following section, an overview of some of these problems will be given. Then, the main topic of this chapter will be supersymmetry, which is one of the most studied BSM theories and the most relevant in the context of this work. This small review, following mostly [30], will describe its main motivations and its most important characteristics.

2.1 Problems of the Standard Model

Despite its great success to predict and describe many natural phenomena, the SM is not able to account for some critical experimental observations. There are also theoretical concerns that need to be addressed. While the latter could seem a rather weak argument to justify the need for the extension of a model, these concerns can be a useful tool to identify parts of our theories in which our understanding is not deep enough, and new physics might be hidden behind fine-tuned adjustments.

The following list of open problems does not intend to be exhaustive, but it includes the most relevant ones for this work and some of the most widely discussed:

- Astrophysical observations from the galactic scale to the cosmological one show that a large fraction of the mass abundance of the universe is not made of ordinary matter, but of an unknown kind of matter which has been called **dark matter (DM)**. Since DM is one of the most important topics for this work, it will be discussed in detail in a separate chapter, Chapter 3. It is worth mentioning also that the SM model cannot explain dark energy, the form of energy that appears to be the dominant one in our universe [31], or give an alternative explanation to the observed energy density at the cosmological scale.

- Neutrinos oscillate between different flavours when they propagate [11, 12]. This means that their mass eigenstates differ from their flavour eigenstates and, therefore, that at least two of the three known neutrinos are massive. In the original

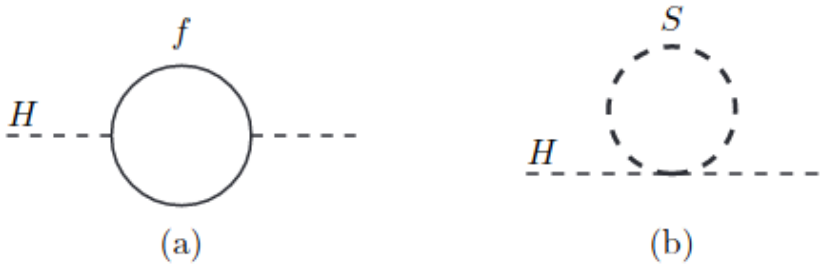

Figure 2.1: Loop corrections to the Higgs boson mass due to a fermion loop (a) or to a boson loop (b).

formulation of the SM, neutrinos are stricly massless and there is not a mechanism for the generation of their mass. Numerous models, all of which introduce new particles to the SM, have been proposed to solve this issue [32].

- One of the most ambitious goals of modern physics is to describe all fundamental interactions within a single theory. Despite being the most complete description of nature at the fundamental level that we currently have, the SM clearly has its shortcomings in this regard. It describes three of the fundamental interactions but, as will be discussed in Sec. 2.2, it does not predicts their unification at any energy scale. Moreover, the SM does not include one of the fundamental interactions, gravity. The formulation of a quantum theory of gravity is a difficult open problem in modern physics. At the present day, the standard description of gravitational phenomena is general relativity.

- A theoretically challenging aspect of the SM and, in general, of our current understanding of particle physics can be referred to as hierarchy problem [13–15]. Some fundamental energy scales of particle physics, such as the electroweak symmetry breaking scale ($\approx 10^2$ GeV) and the Planck scale ($\approx 10^{19}$ GeV), are separated by many order of magnitudes. However, low-scale physics appears to be severely affected by large-scale physics, for example in the calculation of the corrections to the Higgs boson mass, that comes from loops like the one shown in Fig. 2.1. These corrections are arising from loop contribution from Dirac fermions and are divergent for high values of the loop momentum. These divergencies can be regularised using a cut-off energy scale Λ_{UV}, but this leads to corrections to the Higgs boson mass of the kind:

$$\Delta m^2_{H,f} = -\frac{\lambda_f^2}{8\pi^2}[\Lambda^2_{UV} + \ ...]. \tag{2.1}$$

The additional terms are at most logarithmically divergent. The large corrections coming from the Λ^2_{UV} term can in fact be renormalised in such a way that the observed mass value of the Higgs boson, ≈ 125 GeV, can still be obtained from this calculation, but this requires a fine-tuning of the relative counterterms at every order of perturbation theory.

A possible simple solution consists in the introduction of carefully chosen complex scalar fields compensating for the fermionic degrees of freedom causing these corrections. Introducing two complex scalar fields for every fermion and assuming that their coupling λ_s satisfies $\lambda_s = \lambda_f$, they would lead to corrections of the form:

$$\Delta m^2_{H,s} = -\frac{\lambda_s^2}{16\pi^2}[\Lambda^2_{UV} + \ ...]. \tag{2.2}$$

The strongly divergent term arising from the fermionic degrees of freedom and the scalar ones would then cancel, thus avoiding the need for fine-tuning. It is also worth noting that the additional logarithmically divergent terms would then be proportional to the difference between the masses of the fermionic SM particles and the newly introduced bosonic particles. Therefore, the masses of the new particles should be equal, or at least close, to the mass of the SM ones.

- Another apparent issue concerning the SM is that the strong interaction does not violate the charge conjugation parity (CP) symmetry. A process is CP-symmetric if it is invariant under the exchange of all involved particles with the respective antiparticles and the mirroring of their spatial coordinates. This represent an issue, and is sometimes referred to as the strong CP problem, because CP-violating terms could naturally appear in the QCD Lagrangian [16, 17], such as the following:

$$\mathcal{L}_\theta = \theta \frac{g^2}{32\pi^2} G_a^{\mu\nu} \tilde{G}_{\alpha\mu\nu}, \tag{2.3}$$

where g is the coupling of the strong interaction, $G_a^{\mu\nu}$ is the gluon field-strength tensor and $\tilde{G}_{\alpha\mu\nu} = \frac{1}{2}\epsilon_{\mu\nu\sigma\rho}F_\alpha^{\sigma\rho}$ is the adjoint field-strength tensor. If the angle θ was not equal to zero, this term did not vanish and therefore CP-violating effects would occur. However, experimental bounds on the angle θ suggests that this parameter is either very small or equal to zero. The quest for an explanation for this peculiarly small value of θ is known as the strong CP problem. One solution to this problem predicts the existence of a particle called axion, which has assumed relevance in DM searches, as will be shortly discussed in Sec. 3.3.2.

2.2 Motivation for Supersymmetry

Supersymmetric models have been discussed widely since they have been first proposed almost 50 years ago [18]. The first application of SUSY to particle physics was formulated by Pierre Fayet in 1977 [19] to address the hierarchy problem, but one of the reasons for its succes is that it is, in principle, able to provide solutions for other open problems in the SM.

The main idea of SUSY is the introduction of a symmetry between fermionic and bosonic degrees of freedom in a given theory, thus requiring the existence of a new set of particles complementary to the SM particles, which should have the same mass and couplings as the standard fields. Some details about the underlying algebra will be given in Sec. 2.3 and the main phenomenological aspect of the Minimal Supersymmetric Standard Model (MSSM) will be given in Sec. 2.4. Before that, an idea of how SUSY would address various SM problems will be given.

As already mentioned, SUSY was originally devised to solve the hierarchy problem. The introduction of the new SUSY particles, which were initially assumed to have the same masses as the SM ones, should address this problem in the way described in the previous section in Eq. (2.2). Despite the fact that it has now been determined that SUSY particles cannot have the same masses as their SM counterparts, the argument that, because of the remaining logarithmic divergences, the mass difference between them and the SM particles should not be too large still suggests that SUSY could be realised at a relatively low energy scale.

SUSY may be able to offer a sensible DM candidate. In many supersymmetric scenarios, the lightest supersymmetric particle (LSP) is massive, stable and weakly

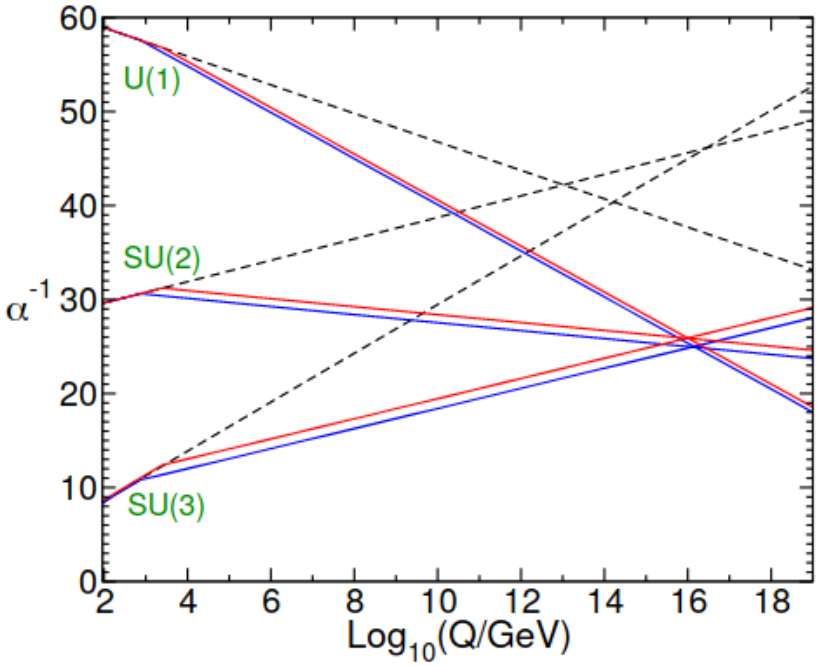

Figure 2.2: Running couplings of fundamental interactions according to the SM (dotted lines) and SUSY (coloured lines). The different colours are due to variations in some of the SUSY parameters. SUSY, differently from the SM, predicts the unification of all fundamental forces at a very high energy scale. Plot taken from [30]

.

interacting with the SM. These characteristics fit well with the requests for a DM candidate, and this will be discussed in greater detail in Sec. 3.3.2.

Another interesting feature of SUSY is that it might also lead to the unification of the three fundamental forces present in the SM. Electromagnetic interaction and weak interaction are unified above a certain energy scale, with a mechanism that is now well understood [33–35]. The dependence of the coupling parameter on the energy scale is described by the renormalisation group equations (RGEs). In the SM, there is no energy scale at which the strong interaction running coupling is equal to the other two couplings, i.e. the SM does not predict a unification of all its interactions at any energy scale. For this reason, it is said that the SM is not a Grand Unified Theory (GUT). SUSY, on the contrary, would require a modification of the RGEs, thus leading to the unification of all the fundamental forces at a high energy scale, as shown in Fig. 2.2.

There are also formal motivations that make SUSY particularly appealing. According to the Coleman-Mandula [36] and Haag-Łopuszański-Sohnius [37] theorems, the only possibility to extend the Poincaré group is the addition of a fermionic generator, which will create a symmetry between fermionic and bosonic particles. Some consequences of these theorems will be discussed in Sec. 2.3. Finally, considering SUSY as a local gauge symmetry leads to the natural inclusion of general relativity [38].

SUSY, being so strongly motivated, is probably the most studied extension of the SM. Moreover, it is appealing also from the experimental side, because it predicts a large number of new particles, some of which are electrically charged or coloured, and these particles should not be much heavier than their SM counterparts. This means that there are, in principle, many experimental possibilities to detect SUSY particles and

that, in absence of a signal, it is possible to establish constraints on SUSY parameter space.

To this day, no experimental evidence of the realisation of SUSY has been observed. Small deviations from the SM have been observed, but they lack the statistical significance to be classified as clear signals, and their interpretation as possible manifestations of SUSY are not widely accepted. It is worth noting that even the simplest supersymmetric theories have a large number of free parameters, which complicates the relative data analysis and damages the predictive power of the theory, as a theory with too many free parameters can be seen as descriptive rather than predictive. This small discussion serves as a first motivation to consider simpler models in the quest to solve specific open problems in particle physics, such as the DM problem. This discussion will be extended in Sec. 3.4.

2.3 Supersymmetric algebra

To introduce a SUSY transformation, one has to consider fermionic generators Q_a, which are two-component Weyl spinors. It is possible to have an arbitrary number $\mathcal{N}$ of Q_a generators and the theory that derives from it is then called an $\mathcal{N}$-supersymmetry.

The action of such a generator will be:

$$Q_a|J\rangle = |J \pm 1/2\rangle, \tag{2.4}$$

where J is the spin of the particle. To define the complete SUSY algebra, one must start from the Poincaré algebra:

$$\left[P_\mu, P_\nu\right] = 0, \tag{2.5}$$
$$\left[M_{\mu\nu}, P_\rho\right] = i\left(g_{\nu\rho}P_\mu - g_{\mu\rho}P_\nu\right), \tag{2.6}$$
$$\left[M_{\mu\nu}, M_{\rho\sigma}\right] = i\left(g_{\mu\sigma}M_{\nu\rho} + g_{\nu\rho}M_{\mu\sigma} - g_{\mu\rho}M_{\nu\sigma} - g_{\nu\sigma}M_{\mu\rho}\right), \tag{2.7}$$

where P_μ is the generator of space-time translations, $M_{\mu\nu}$ is the generator of Lorentz transformations and $g_{\mu\nu}$ is the metric tensor. It is then necessary to add:

$$\{Q_a, Q_b^\dagger\} = \left(\sigma^\mu\right)_{ab} P_\mu \tag{2.8}$$
$$\{Q_a, Q_b\} = \{Q_a^\dagger, Q_b^\dagger\} = 0, \tag{2.9}$$
$$\left[Q_a, P_\mu\right] = \left[Q_a^\dagger, P_\mu\right] = 0, \tag{2.10}$$
$$\left[M_{\mu\nu}, Q_a\right] = -i\,\Sigma^{\mu\nu}_{ab}\,Q_b, \tag{2.11}$$

where $\sigma^\mu = (\mathbb{1}, \sigma_i)$ contains the Pauli matrices σ_i and $\Sigma^{\mu\nu} = \frac{i}{4}\left[\gamma^\mu, \gamma^\nu\right]$. γ_μ are the Dirac matrices.

The practical consequence of this complex algebra is that the generators Q introduce supersymmetric partners for the well-known SM particles. Since the generators commute with P_μ, these supersymmetric partners have the same masses as the original SM particles. Moreover, the generators do not have an effect on the SM interactions, meaning that all the other quantum numbers are also conserved.

The possibility of having multiple generators, the complications present in the SM and various phenomenological contraints mean that the development of a supersymmetric theory has to be handled with care, and the derivation of the resulting particle spectrum is not trivial. The following section discusses one of the simplest practical realisation of a supersymmetric model implemented in the SM.

Supermultiplet	fermions	bosons	$SU(3)_C$,	$SU(2)_L$,	$U(1)_y$
q	(u_L, d_L)	$\tilde{u_L}, \tilde{d_L}$	3,	2,	1/3
$\bar{u}$	(u_R)	$\tilde{u_R}$	3,	1,	$-4/3$
$\bar{d}$	(d_R)	$\tilde{d_R}$	3,	1,	2/3
L	(ν_{e_L}, e_L)	$(\tilde{\nu_{e_L}}, \tilde{e_L})$	1,	2,	-1
$\bar{e}$	(e_R)	$(\tilde{e_R})$	1,	1,	-2
H_u	$\left(\tilde{H_u^+}, \tilde{H_u^0}\right)$	(H_u^+, H_u^0)	1,	2,	$+1$
H_d	$\left(\tilde{H_d^0}, \tilde{H_d^-}\right)$	(H_d^0, H_d^-)	1,	2,	-1
$\hat{G}^a$	$\tilde{g}$	g	8,	1,	0
$\hat{W}^i$	$\tilde{W^\pm}, \tilde{W^0}$	$W^\pm, W^0$	1,	3,	0
$\hat{B}$	$\tilde{B}$	B	1,	1,	0

Table 2.1: The particle content of the MSSM. For simplicity, only the first of three generations of quarks and leptons is shown [39].

2.4 The Minimal Supersymmetric Standard Model

The MSSM is an $\mathcal{N} = 1$ supersymmetry, i.e. only one generator Q is used and each SM particle has one superpartner. Since the SM particles cannot be arranged in supermultiplets because of numerous phenomenological problems [30], this model requires new particles.

2.4.1 Particle content

In the MSSM, SM particles and their SUSY counterparts are organised in supermultiplets, which are irreducible representations of the algebra introduced in the previous section. A supermultiplet will then contain particles that have the same mass and quantum numbers, but a different value of the spin. The particle content of the MSSM is shown in Table 2.1.

Squarks are the superpartners of the SM quarks. For each quark, there are two spin-0 bosons, because the left- and right-handed components of these fermions are independent degrees of freedom. Since squarks have spin 0, their chirality is not defined, but they are still commonly referred to as left- or right-handed, depending on the quark from which they have been generated.

Sleptons are the superpartners of the SM leptons. Similarly to squarks, there are two scalars for each charged lepton and an additional scalar for each SM neutrino.

The Higgs sector of the MSSM is more complicated than the SM one. In linear realisations of SUSY, it is necessary to add a second Higgs multiplet, because the invariance under SUSY transformations means that it is not possible for a single Higgs multiplet to generate the masses of both up- and down-type quarks. This means that there are multiple Higgs particles: one of the two CP-even states is identified with the 125 GeV scalar detected at the Large Hadron Collider (LHC) in 2012, and there are 3 additional scalars, two of which are eletrically charged, and a pseudoscalar. All these particles will have supersymmetric partners called higgsinos. Finally, the gauge bosons of the SM get fermionic partners. They are called **gluinos**, binos and winos. Electroweak symmetry breaking induces a mixing between electroweak gauge bosons, which in turn leads to a mixing between higgsinos, binos and winos. Their

mixing means that the actual physical particles will be the **neutralinos** ${\chi^0}_i$ and the **charginos** ${\chi^\pm}_i$, collectively called **weakinos**. There are four neutralinos, which can be seen as the partners of the photon, the Z boson and the neutral Higgs bosons, and two charginos, which can be seen as the partners of the $W^\pm$ bosons and the charged Higgs bosons.

2.4.2 SUSY breaking

The previous sections suggests that, in principle, the MSSM predicts a large number of particles that should have the same masses as their SM counterparts, and therefore should be easy to detect. The fact that they have not been detected means that their masses have to be higher and this can happen if SUSY is a *broken* symmetry. This means that there should be SUSY-breaking terms in the Lagrangian, but their exact form is unknown [40–43]. However, the form of these terms can be constrained. The breaking of SUSY is generally chosen to be *soft*, meaning that the symmetry-breaking term can only contain mass and interaction terms having positive mass dimension. This guarantees that the cancellation of the quadratic divergences, which was discussed in Sec. 2.1 and is one of the main advantages of SUSY, is preserved. The correction terms to the mass of the Higgs boson would then present no quadratic divergences, and the logarithmic ones would be proportional to the ratio between the electroweak scale, i.e. ≈ 100 GeV, and the mass scale of the SUSY breaking. In order to be able to solve the hierarchy problem as intended, SUSY would then have to be realised at an energy scale that is not too far from the electroweak scale. For this reason, the possibility to detect MSSM particles soon has been looked at with optimism. However, the current experimental searches seem to suggest that these particles, if they exist, are not within reach of the LHC.

It is important to note that the presence of two broken symmetries, i.e. electroweak symmetry and suspersymmetry, leads to the mixing of the interaction eigenstates of the SUSY particles. Therefore, the particles discussed in Sec. 2.4.1 are not necessarily mass eigenstates. For some particles, for example the squarks belonging to the first two generations, these effects are negligible, but they have very large effects for other particles, such as the stop squarks and, as already mentioned, the weakinos.

The insertion of soft SUSY breaking in the Lagrangian increase greatly the number of free parameters of the MSSM, which are in total over 120 [44]. For this reason, analyses in this parameter space are extremely hard to perform, and usually, some assumptions are made in order to reduce the number of free parameters, using what are called constrained SUSY models, which will be discussed in Sec. 2.4.4.

2.4.3 R-parity and the lightest neutralino χ_1^0

The naive introduction of the MSSM as it has been discussed until now would lead to a rapid decay of the proton, which has instead been proven to be stable or to have an extremely long lifetime. This would be caused by lepton-number- and baryon-number-violating interactions, which are in principle not forbidden in the MSSM Lagrangian. Therefore, a mechanism to prevent these terms from appearing has been considered, called R-parity conservation [45, 46]. A new quantum number is introduced as:

$$R = (-1)^{3B+L+2S}, \tag{2.12}$$

where B and L are, respectively, the baryon and lepton number of the particle and S is its spin. Every SM particle has R-parity of 1, while all SUSY particles have R-parity

equal to -1. If this quantum number is conserved, SUSY particles can only interact in pairs, and the stability of the proton is preserved. This is also the reason why the LSP is stable: an isolated SUSY particle cannot decay into SM particles.

This has a very important consequence in the context of this work. In many scenarios, the LSP is the lightest neutralino, ${\chi^0}_1$. This particle is then massive, stable and only weakly interacting and therefore a suitable DM candidate. Therefore, processes involving the production of ${\chi^0}_1$ are not only interesting to study the MSSM phenomenology, but also for DM searches.

In the context of this work, it is important to keep in mind that all the neutralinos are a mix of neutral higgsino, neutral wino and bino fields. At different parameter-space points, their composition will be different and this will have an important effect on their phenomenology.

In the MSSM Lagrangian, the term containing the fields mixing into the neutralinos can be written as:

$$\mathcal{L}_{\chi_i^0} = -\frac{1}{2}(\Psi^0)^T N_{i,j} \Psi^0 + h.c., \tag{2.13}$$

where

$$(\Psi^0)^T = \left(\tilde{B},\, \tilde{W}_1,\, \tilde{H}_1^0,\, \tilde{H}_2^0\right). \tag{2.14}$$

The $N_{i,j}$ matrix is a 4×4 symmetric matrix. The terms regarding the lightest neutralino are $N_{1,j}$. Specifically, $N_{1,1}$ will determine the fraction of bino content, $N_{1,2}$ the wino content, and the remaining two the higgsino content.

2.4.4 Constrained models and experimental searches

It has been mentioned that the large MSSM parameter space requires the use of simpler constrained models to make experimental analysis possible. Among the several existing, the ones that are relevant for this work, namely the contrained MSSM(CMSSM) [47] the phenomenological MSSM with 10 free parameters(pMSSM10) [48], and with 11 free parameters (pMSSM11) [49] will be introduced here.

CMSSM

The CMSSM is built upon constraints motivated by the coupling of a minimal supergravity to the MSSM, which is then seen as a low-energy manifestation of a GUT. These constraints mean that there are only five free parameters, defined at the GUT scale:

- $m_{\frac{1}{2}}$ is the value of all the soft SUSY breaking masses for fermions;
- m_0 is the value of all the soft SUSY breaking masses for bosonse;
- A_0 is the value of all trilinear scalar couplings at the GUT scale;
- $\tan\beta$ is the ratio between the vacuum expectation values (VEVs) of the two Higgs doublets;
- $sgn(\mu)$ is the sign of the Higgs mixing parameter.

pMSSM10

The pMSSM10 is based on the assumption of minimal flavour violation and CP conservation. They lead to a reduction of the parameter space to 19 free parameters. Further approximations can reduce the parameter space even more; an often studied contrained model is the phenomenological one containing 10 free parameters, which are:

- the squark masses for the first two generations are assumed to be equal to $m_{\tilde{q}_1}$; the squark masses for the third generation are equal to $m_{\tilde{q}_3}$;
- a unified slepton mass term $m_{\tilde{l}}$;
- three gaugino mass terms M_i with $i = 1, 2, 3$;
- the trilinear coupling A_0;
- the Higgsino mixing parameter μ;
- the pseudoscalar Higgs mass M_A;
- the ratio of the two Higgs doublets VEVs ($\tan(\beta)$.

pMSSM11

A slight complication over the pMSSM10 which has also been considered for some analyses in this work is the pMSSM11, which differs only in one assumption: the slepton mass term $m_{\tilde{l}}$ is no longer equal for all three generations, but only for the first two. The stau has a separate mass term $m_{\tilde{\tau}}$, rising the number of free parameters to eleven.

Supersymmetric searches have been performed extensively at the LHC, where the detection of SUSY particles has been considered very likely, because of the assumption that their mass should not be too large. Even if no signal has been detected so far, limits have been set on the parameter spaces of various contrained models. The limits set by the ATLAS experiment can be found in [50] and those set by the CMS experiment can be found in [51].

Figures 2.3 and 2.4 show mass limits for squarks and the LSP obtained by LHC experiments. These limits have been calculated in various simplified models, which are in general different from the constrained scenarios we just described. These models are described in the references provided in the plots and describing each one of them is beyond the scope of this work. A common assumption is, for example, having mass-degenerate light-flavour squarks. This means, however, that these limits only apply to the models in question and different limits would be obtained for different models. Therefore, it is very hard to make general statements on the MSSM and these bounds do not necessarily forbid the existence of particles with masses smaller than these limits.

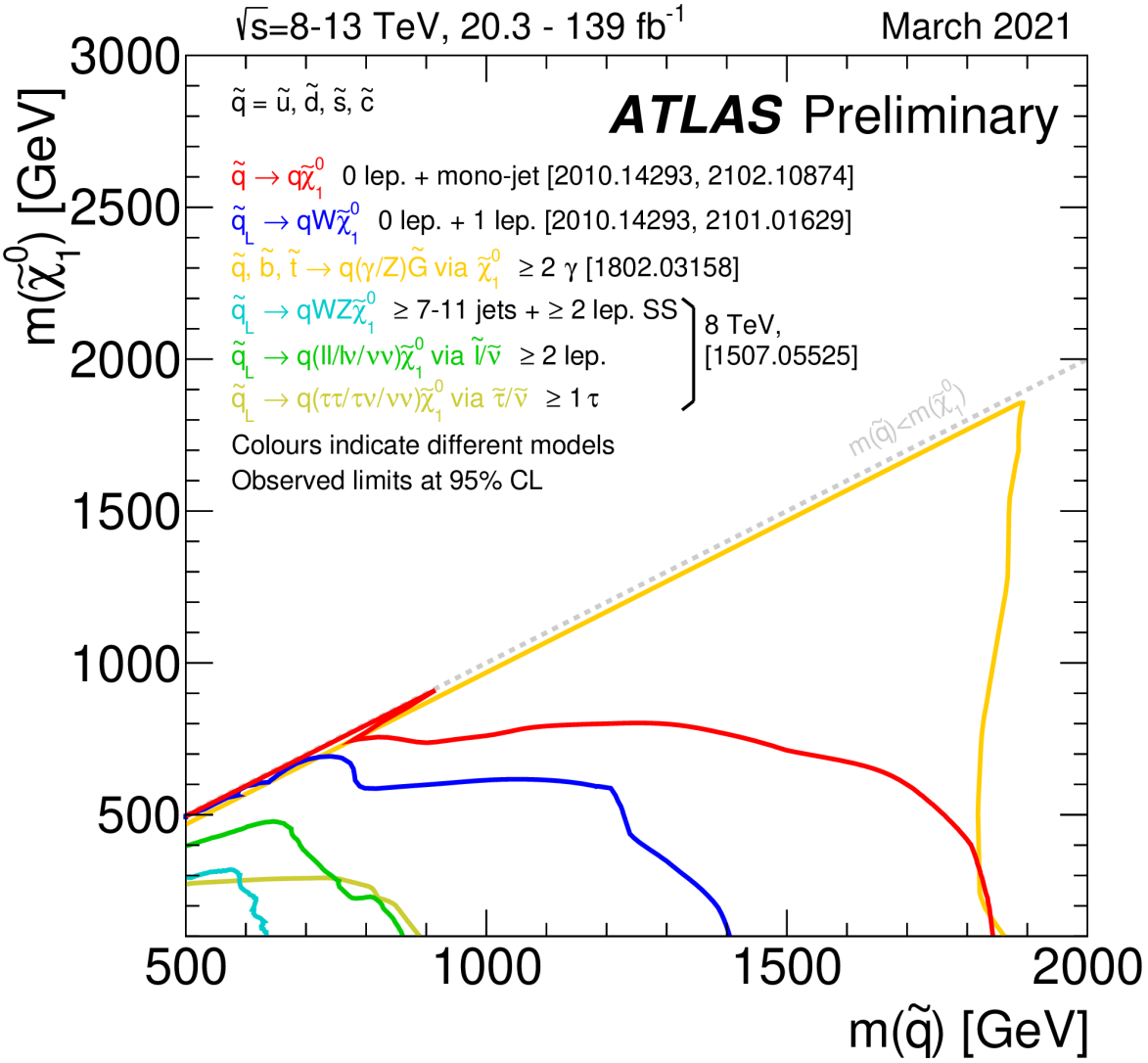

Figure 2.3: Exclusion limits for the masses of squarks and lightest neutralinos set by the ATLAS experiment [52].

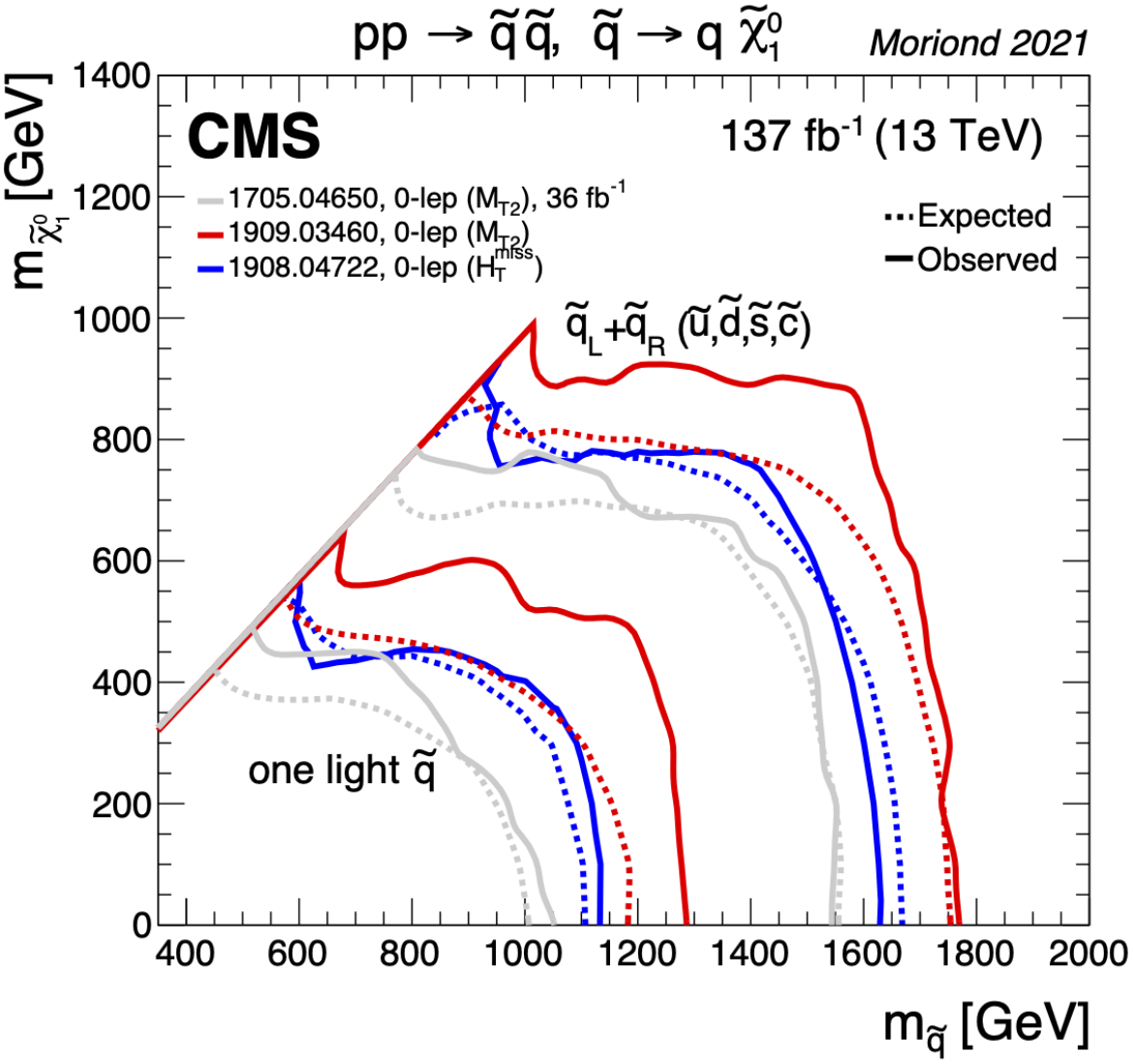

Figure 2.4: Exclusion limits for the masses of squarks and lightest neutralinos set by the CMS experiment [53].

Chapter 3

Dark Matter

The existence of dark matter (DM) represents one of the most striking problems in modern physics. The idea of dark bodies that consist of matter that does not interact electromagnetically that were necessary to explain the velocity dispersion of observed stars was suggested already in the late 1800s [54]. In the second half of the 20th century, with the improvement of astrophysical observations, it only became clearer that the observed matter content of the universe was not able to justify the gravitational effects observed at the galactic scale and, later, at even larger scales.

To explain gravitational effects that do not correspond to visible matter there are two major possibilties: the presence of additional matter or the formulation of a modified theory of gravity. A great effort in both directions has been made by the scientific community, but so far no conclusive answer has been reached. Notably, in the past, both approaches have provided answers to similar problems: additional matter, the planet Neptune, was conjectured, and then found, while studying the irregularities of the orbit of Uranus; a new theory of gravity, general relativity, provided an explaination to the observed precession of the perihelion of Mercury. Therefore, both lines of research could lead to a better understanding of the DM problem.

In the following section, an overview of the existing evidence for DM will be given. Afterwards, we will discuss some of the proposed solutions to the DM issue. In conclusion, the current strategies used to search for DM and their current status, with an emphasis on those relevant for this work, will be discussed.

3.1 Evidence for dark matter

The inability of the observed matter content of the universe to explain many astrophysical observations was, as already anticipated, clear for a long time. These observations concern relatively small astrophysical scales, such as the galactic scale, but also the geometric properties of the observed universe as a whole. The following list contains, without any intention of completeness, a collection of the best known and important evidence for the presence of DM. It will be assumed that the observed effects are due to the presence of additional matter; the possibility that instead it is necessary to formulate a new theory of gravity will be discussed briefly in Sec. 3.2.

- One of the most concrete evidence for dark matter comes from the rotation curves of galaxies. Starting from the observation of the Andromeda galaxy made by Rubin and Ford in 1970 [3, 4], these curves showed a clear inconsistence with the expectation. Finding the rotational velocity of stars in a galaxy is, in principle,

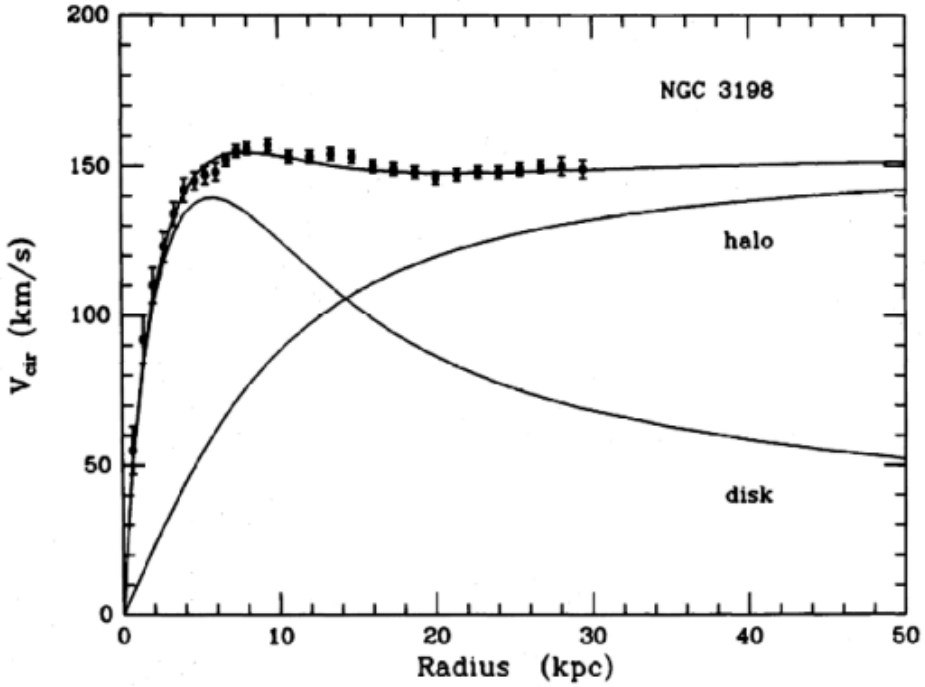

Figure 3.1: Rotation curve for the galaxy NGC 3198 [55].

trivial and should not be different from finding the orbital velocities of the planets in the solar system. The mass profile of the galaxy can be assumed to be spherically symmetric and, at a distance R from the centre, is then equal to:

$$M(R) = 4\pi \int_0^R r^2 \rho\,(r)\, dr, \tag{3.1}$$

where $\rho(r)$ is the mass density. The orbital velocity of stars can then be written as:

$$v(R) = \sqrt{\frac{GM(R)}{R}}. \tag{3.2}$$

Apparently, most of the mass content should be close to the centre, because most of the visible stars are. This would lead to a decrease of the orbital velocity with increasing R, like it happens in the solar system, where the outermost planets move more slowly than the inner ones as most of the mass of the system is contained in the Sun. However, as shown in Fig.3.1, for large R the orbital velocity remains constant. This has been found to be not a peculiar characteristic of a single galaxy, but rather the standard observed behaviour for galaxy rotation curves. The figure anticipates how the presence of a halo of non-visible matter surrounding the whole galaxy would explain the observed rotational velocity.

- Gravitational lensing is the bending of light that crosses a region of space that is deformed by a gravitational field. It was already predicted by Newtonian gravity, but with only a half of the observed effect, that is instead fully explained by general relativity [56]. Due to its observable effect on light that has been emitted by other objects, it is an excellent tool to study the gravitational effects of objects that do not emit electromagnetic radiation, or that emit faintly. As of today, many observations based on gravitational lensing have led to many discoveries, including a great number of exoplanets and the observation of the

Figure 3.2: The effect of weak lensing on the cluster 2218 Abell, credits: NASA, ESA, and Johan Richard (Caltech, USA) [58].

most distant individual star known [57]. The study of the latter and of many other observations clearly shows that the observed lensing effects cannot be explained by visible matter alone, to the point that it is now taken for granted that, when observing lensing from large scale structures, the main source of gravitational lensing is dark matter. An interesting example is the bullet cluster, that will be discussed later, or the phenomenon of weak lensing observed in clusters of galaxies. The latter, see Fig. 3.2, consists in the deformation of the shape of galaxies due to the presence of other gravitational fields, typically clusters of galaxies, between the observer and the observed galaxies. Since the galactic shapes present a certain amount of ellipticity, the presence of a systematic effect is only detectable if a great number of galaxies are observed, and their shapes are altered in a statistically significant way.

- The bullet cluster, shown in Fig. 3.3, which is actually the smaller of the two galaxy clusters that compose the cluster 1E 0657-56, has been widely discussed over the last 20 years [5–7]. Nowadays, it appears that it is not unique and similar properties have been observed in other clusters [59, 60]. However, the discussion about it is still instructive about the dark matter issue. 1E 0657-56 consists of two clusters that collided around $150 \cdot 10^6\, yrs$ ago; the smaller one is called bullet cluster because of its shape. Different components of the clusters are observed in different wavelenghts. The stars, that emit mostly visible light, have been scarcely affected by the collision, as they only interact gravitationally and collisions between stars are highly unlikely; the dominant observed matter component, the interstellar gas, has been more severely affected and has been slowed down more significantly, due to electromagnetic interactions. This has caused a displacement between the location of the majority of stars and the majority of the interstellar gas that is clearly observable. Moreover, the emissions from both components are affected by gravitational lensing. Despite the fact

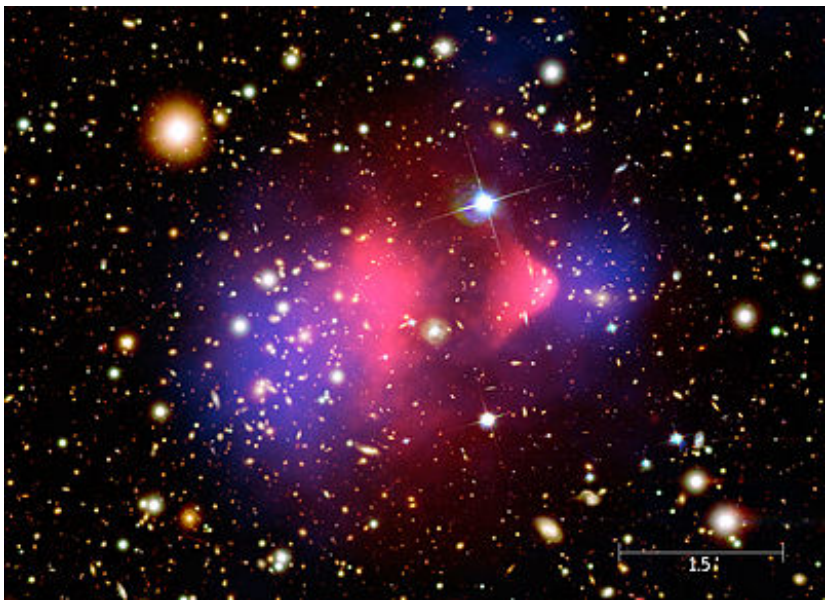

Figure 3.3: The bullet cluster showing the visible galaxies, the X-ray emission from the interstellar gas (pink) and the assumed dark matter halo (blue) [62].

that the interstellar gas was expected to be the dominant matter component, the lensing effects seem to suggest that most of the matter is located in the region containing the stars, indicating that a third form of matter, that interacted weakly and is not visible, is actually the dominant one. The phenomenology of the bullet cluster has then been considered as favouring the existence of dark matter over the necessity of a new theory of gravity, as in a new theory of gravity the lensing effects would anyway be stronger around the interstellar gas, that without the addition of new matter would still be the dominant matter form. However, after the initial discussion, it has been highlighted that the observed collision velocity would pose difficulties to the dark matter models as well [61]; it is likely that the discussion about the bullet cluster will continue in the future.

Modern cosmological observations also show a significant discrepancy between the observed matter and the actual matter content of the universe. This issue also involves dark energy [31], which is not relevant for this work. However, it is worth noting that the presence of dark matter alone would be far from providing a cosmological model in agreement with observations.

The most widely accepted cosmological model is the Λ-CDM model [8], which has also been called the standard model of cosmology. This model is based on the presence of a cosmological constant Λ, that plays the role of dark energy and explains the accelerated expansion of the universe, and cold dark matter (CDM), where the adjective cold means that dark matter is non relativistic. The correct theory of gravity is assumed to be general relativity, resulting in a Friedmann-Lemaître-Robertson-Walker metric. The numerical value of Λ is chosen specifically to obtain a geometrically flat universe. The success of this model stems from the fact that it provides a good explanation for many observed phenomena and it was used to make some successful predictions, like the existence of baryon acoustic fluctuations [63,64]. However, the Λ-CDM model does not provide any information on the nature of dark matter and dark energy, which have so far eluded experimental observations and theoretical predictions.

The Λ-CDM model explains some phenomena that concern dark matter and that also allow to estimate its amount in the universe, for example:

- The cosmic microwave background (CMB) is electromagnetic radiation permeating the whole universe, resulting from the recombination between electrons and protons to form the first hydrogen atoms. This has been considered as primary evidence sustaining the big bang theory; at its formation, the universe was extremely dense and began expanding and therefore cooling; approximately 380000 years after the big bang, its temperature was low enough ($\approx 3000K$) for the recombination to happen. The radiation emitted in this event has then been redshifted because of the continuous expansion of the universe, and it is now observable as the CMB. Nowadays, it can be observed as a nearly perfect black body spectrum corresponding to a temperature of $2.72K$, as measured by the WMAP collaboration [65] and the Planck satellite [66, 67]. Its irregularities, however small, contain extremely important information about the composition of the universe. Therefore they have been analysed and used to determine the matter content, including dark matter. The observed densities are then expressed in terms of the critical density of the universe, which is the density required for the universe to be flat. The observed matter content for baryonic matter and dark matter are, respectively, according to [67]:

$$(\Omega_b)\ h^2 = 0.02212 \pm 0.00022, \tag{3.3}$$
$$(\Omega_{DM})\ h^2 = 0.1206 \pm 0.0021, \tag{3.4}$$

  where $h = 0.674 \pm 0.014$ is the reduced Hubble constant. DM would then be, according to the Λ-CDM model, approximately 5 times more abundant than baryonic matter in the universe.

- The formation of large-scale structure has been reproduced performing N-body simulations using the Λ-CDM model to interpret the anisotropies of the CMB [9, 10]. These simulations show that to predict structure formation in agreement with the observed trends, i.e. the formation of gradually larger structures starting from small ones, one needs to consider predominantly cold DM and not relativistic (or hot) DM, which would lead to the formation of larger structures first, which would then break into smaller ones. Moreover, these simulations show that the dark matter haloes have the predominant role in the formation of structures. However, some elements of tension remain [68,69]. A small amount of hot DM would still be required to fully explain the observed structure, and it is still unclear if small scale structures, like dwarf galaxies, are well reproduced by simulations based on the Λ-CDM model, since they are much harder to resolve.

3.2 Proposals for modified gravity

Throughout the previous section, we implied that the observed phenomena are to be explained finding additional matter. However, the possibility that the current theory of gravity needs modification has not been ruled out. Despite the fact that the dark matter hypothesis has generally received more attention, alternative theories of gravity have also been constantly studied over the last decades. Even though these theories are not the subject of this work, it is worth mentioning some of them and giving a quick overview of their proposed solution to the DM problem.

One of the first proposals was the MOdified Newtonian Dynamics (MOND), formulated by Mordehai Milgron in 1983 [70]. In MOND, Newtonian gravity is a high-acceleration limit that does not describe properly systems where the accelerations are

much smaller. The MOND gravitational law is:

$$\vec{F} = m\vec{a}\,\mu\left(\frac{a}{a_0}\right), \tag{3.5}$$

where a_0 is a new fundamental constant with the dimension of acceleration and $\vec{F}$ is the force necessary to give an acceleration a to a body of mass m. The function $\mu(x)$ is not fixed and can be chosen in different ways, but it has to approach unity for large values of a, in order to recover the Newtonian second law, $\vec{F} = m\vec{a}$. To explain astrophysical observations, one also needs $\mu(x) \to x$ when $x \ll 1$ and the numerical value of a_0 to be very small, of the order of $10^{-10}\, ms^{-2}$. A possible functional form of μ is:

$$\mu\left(\frac{a}{a_0}\right) = \frac{1}{1+\frac{a_0}{a}}. \tag{3.6}$$

A star orbiting a galaxy would then be in the MONDian regime, where indeed $\mu\left(\frac{a}{a_0}\right) \to \frac{a}{a_0}$ and the gravitational law can be approximated as $F = m\frac{a^2}{a_0}$. Writing the mass of the star as m, the mass of the galaxy as M and the radius of the orbit of the star is r, the orbital velocity v of the star can be calculated from:

$$\frac{GMm}{r^2} = m\frac{\left(\frac{v^2}{r}\right)^2}{a_0}, \tag{3.7}$$

where $G = 6.67 \cdot 10^{-11}\ \mathrm{m^3 kg^{-1} s^{-2}}$ is the gravitational constant. This results in

$$v = \sqrt[4]{GMa_0}, \tag{3.8}$$

which does not depend on the radius, in agreement with the flat rotational curves observed.

MOND is not able to provide an explanation for many cosmological observations, but it is only efficient at the galactic scale. It also fails to account for the observation of the bullet cluster, where the gravitational lensing effects observed appear to be caused by invisible matter; this is not predicted by MOND. However, it should be noted that MOND is not a complete theory, but rather a solution to a specific problem. It would have to be embedded into a more complete framework that would, at a later stage, provide an explanation for many other phenomena and, possibly, a cosmological model.

A possible complete framework of which MOND would be a consequence, AQUAL (A QUAdratic Lagrangian), has been proposed by Milgrom himself and Bekenstein in 1984 [71]. In 2004 Bekenstein has formulated a relativistic theory that would reproduce MOND, called TeVeS (Tensor Vector Scalar gravity) [72]. An overview of TeVeS is contained in [73]. These theories have been used to tackle some of the issues mentioned in Sec. 3.1, with mixed results.

Naturally, there are many more proposals for modified gravity. Even if they have received less attention than the DM hypothesis they are the object of the work of a large fraction of the scientific community, and they have occasional surges of popularity, especially when the DM hypothesis is considered to be struggling.

3.3 The dark matter issue in particle physics

Assuming that the answer to the many issues raised in Sec. 3.1 is the DM hypothesis, the next step is to determine what the nature of DM is at the elementary level and to

look at DM from the particle physics point of view. A more complete discussion about DM can be found in [74], and many parts of the following sections follow this reference. A first natural attempt is to see if DM could be made of the ordinary matter that we already know, perhaps in some exotic form.

Amongst the Standard Model (SM) particles, the best suited candidates are (probably) the neutrinos: since they do not interact electromagnetically, they are indeed "dark". Nevertheless, they present some problems: they are massive [1], but their masses are, most likely, not large enough to account for the very large amount of DM that is expected to be present in the universe. Moreover, due to their lightness, they move at relativistic velocities, and therefore a neutrino-dominated DM would not be compatible with the observed formation of large scale structures [75]. As already mentioned, it appears that a small amount of hot DM is required to explain the formation of some smaller structures; therefore it is possible that a fraction of what we call DM is made of neutrinos, but they have been found non satisfactory as a single candidate to solve the entire issue.

Another hypothesis is the presence of large objects, made of ordinary matter, but very difficult to observe [76], such as black holes, neutron stars, brown dwarves, rogue planets and particularly faint white or red dwarves. Similarly to neutrinos, it is possible that these objects make up some fraction of the unobserved matter content of the galaxies, but they do not seem to be able to account for the large amount of DM expected to be found in the galaxy [77].

Most importantly, the anisotropies in the CMB and the observations of large scale structures actually put bounds on the amount of baryonic matter [67]. For this reason, it is generally assumed that DM is made of a new kind of matter, composed by yet unknown particles. The properties of these particles remain largely undetermined, but it is possible to use the knowledge that we have on DM abundance and on its interactions to establish a few starting requirements that have to be fulfilled by a particle to be a DM candidate.

An ideal DM candidate has to be massive, as it has to explain the observed gravitational effects and the modern cosmological models require DM to be made of matter and not, for example, radiation. It also needs to be non-relativistic; this means that the particles have to be relatively heavy or that, if they are light, they are not produced thermally. Finally, it needs to interact at most weakly with other particles, since only gravitational effects have been observed and electromagnetical and strong interactions are obviously excluded in a candidate for *dark* matter. These points will be discussed in more detail for various specific candidates that will be presented in the following section 3.3.2. A particle satisfying these requisites is usually called a WIMP, from weakly interacting massive particle.

3.3.1 Dark matter relic abundance

The study of a particle as a DM candidate requires some quantitative considerations about its abundance, or relic density. Depending on its mass and on its interactions, the relic density of a specific candidate can be calculated. Seeing how well the theoretical prediction compares with the observed DM abundance in the universe will be one of the key factors in determining if the object of the study is a suitable DM candidate or not. Relic densities can be calculated for all particles, but this calculation is heavily model dependent and in general not a trivial task. Several numerical tools can be used

[1] The SM describes the neutrinos as massless, but it is known from neutrino oscillations that they have a small but non-zero mass [11, 12].

to calculate relic densities of possible DM candidates, such as `MicrOMEGAs` [78, 79], `MadDM` [80] and `DarkSUSY` [81].

The importance and the difficulty of a relic density calculation has already been stated, and it is not the object of this work. The rigorous computation of this quantity requires solving a complicated Boltzmann equation. However, since a correct prediction of the observed relic abundance represents a key parameter in judging a DM candidate, we give here a short overview of an approximated calculation performed in a specific framework, considering as a DM candidate a WIMP. The WIMP category includes various candidates that satisfy the properties that have been listed before; in this specific case, we will consider a WIMP candidate that interacts with the SM via an annihilation process mediated by the weak interaction and electro-weak scale mass, closely following [74].

To perform this calculation, we assume that the Λ-CDM model correctly describes the evolution of the universe. In the early stage of the universe, DM and SM particles were in thermal equilibrium, through the process:

$$\chi\,\chi \;\longleftrightarrow\; f\,\bar{f}, \tag{3.9}$$

where χ is the DM particle and f is a SM fermion. If this process is characterised by a cross section σ, and n_χ is the density of DM particles, m_χ their mass and v_χ their velocity, the interaction rate $\Gamma = \sigma v_\chi n_\chi$ describes the probability of this process to occur. These quantities can be estimated using some assumptions:

- The cross section σ considers a weak interaction, that will cause the appeareance of the mass of the Z boson m_Z and of the cosine of the Weinberg angle c_w. Assuming an s-channel process (see e.g. the left diagram in Fig. 3.6)in Sec. 3.9, the cross section can be approximated as:

$$\sigma = \frac{\pi\alpha^2 m_\chi^2}{c_w^4 m_Z^4}. \tag{3.10}$$

- The density of DM particles at the equilibrium depends on the temperature T and on the mass of the particle, and also on the number of degrees of freedom g that it has. For a Majorana fermion $g = 2$, which will be assumed throughout the following section. The expression for the DM density at the thermal equilibrium is then:

$$n_\chi = g\left(\frac{m_\chi T}{2\pi}\right)^{\frac{3}{2}} e^{-\frac{m_\chi}{T}}. \tag{3.11}$$

- Finally, the velocity can be very roughly estimated as:

$$v_\chi = \sqrt{\frac{2T}{m_\chi}}. \tag{3.12}$$

Because of the expansion of the universe and its subsequent cooling, at a certain moment (or, equivalently, temperature) the density of the particles is no longer high enough to mantain this equilibrium and these different species *decouple*. The temperature of decoupling is defined as the temperature at which the interaction rate Γ is equal to the Hubble expansion parameter H:

$$H(T) = \frac{\pi}{\sqrt{90}M_{Pl}}\sqrt{g_{\text{eff}}\,(T)}T^2, \tag{3.13}$$

where M_{Pl} is the Planck mass and g_{eff} is the effective number of degrees of freedom, depending on the number of SM particles that are not yet decoupled.

To know the relic density at the current temperature T_0 one has to start from the value of n_χ at the last moment at which the equation for the density, Eq. (3.11), was valid, i.e. the time of decoupling. Starting from said value, it can be evolved to the present temperature and it can be established if the obtained result is compatible with the observations or not.

The condition for decoupling is $\Gamma(T_{\text{dec}}) \stackrel{!}{=} H(T_{\text{dec}})$. In this equality, the quadratic dependence on the temperature cancels out, and we are left with:

$$e^{-\frac{m_\chi}{T_{\text{dec}}}} = \frac{\pi\sqrt{\pi}}{\sqrt{90}\alpha^2}\frac{c^4{}_w m_Z^4}{m_\chi^3 M_{Pl}}\sqrt{g_{\text{eff}}\,(T_{\text{dec}})}. \tag{3.14}$$

The following step is to make an estimate of $\sqrt{g_{\text{eff}}\,(T_{\text{dec}})}$, which is smaller than the full number g_{eff}, because we expect that some of the heaviest SM particles, i.e. the top quark and the weak bosons, already decoupled at an earlier time. A reasonable estimate is then $\sqrt{g_{\text{eff}}\,(T_{\text{dec}})} \approx 85$. Also assuming for simplicity $m_\chi = 30\,\text{GeV}$, one obtains the result:

$$\frac{m_\chi}{T_{\text{dec}}} \approx 23. \tag{3.15}$$

At this point, plugging Eq. (3.14) into Eq. (3.11) and using the result in Eq. (3.15) yields approximately:

$$n_\chi(T_{\text{dec}}) \approx \frac{10^3}{23^{3/2}}\frac{m_Z^4}{M_{Pl}}. \tag{3.16}$$

To transpose this result into the present relic abundance of DM at the current temperature T_0, we consider that after decoupling the number density of a particle drops like a^{-3}, where a is the scale factor representing the expansion of the universe:

$$n_\chi(T_0) = n_\chi(T_{\text{dec}})\left(\frac{a(T_{\text{dec}})}{a(T_0)}\right)^3. \tag{3.17}$$

Finally, we need to consider that the combination $a(T)T$ is almost constant, and that it is possible to write:

$$\left(\frac{a(T_{\text{dec}})T_{\text{dec}}}{a(T_0)T_0}\right)^3 = \frac{g_{\text{eff}}(T_0)}{g_{\text{eff}}(T_{\text{dec}})} \approx \frac{1}{28}. \tag{3.18}$$

We can now write the actual density of dark matter $\rho_\chi(T_0)$:

$$\rho_\chi(T_0) = m_\chi\left(\frac{a(T_{\text{dec}})T_{\text{dec}}}{a(T_0)T_0}\right)^3\frac{T_0^3}{T_{\text{dec}}^3}n_\chi(T_{\text{dec}}) \approx 3\cdot 10^3\frac{m_Z^4}{m_\chi^2 M_{Pl}}T_0^3 \tag{3.19}$$

and transform it into the familiar form:

$$\Omega_\chi h^2 = \frac{\rho_\chi(T_0)h^2}{3M_{Pl}^2H_0^2} \approx 0.12\left(\frac{13\text{GeV}}{m_\chi}\right)^2. \tag{3.20}$$

A series of approximations have been made in this calculation, but it is interesting that the result of Eq. (3.20) does not differ drastically from the one obtained with the rigorous solution of the Boltzmann equation, that can also be found in [74].

This result has generated some enthusiasm, up to the point that it has been referred to as the "WIMP miracle": considering a DM candidate with a mass close to the

electroweak scale and interacting weakly with the SM, one obtains for the expected relic density of this particle a result that is very close to the observed one. The enthusiasm was also due to the fact that a popular extension of the SM, the MSSM, predicts the existence of a particle that would fit perfectly into this role, the lightest neutralino χ_1^0.

This calculation of the relic density has been inserted as an example to show how the cosmological bounds and these calculations can shed light on the adequacy of a particle as a DM candidate as discussed in the beginning of this section.

3.3.2 Dark matter candidates

Since the properties of DM particles are mostly undetermined, a large number of candidates remain available. Most of these hypothetical particles were initially conceived in the context of other BSM theories, and have been later adapted as DM candidates if their characteristics appeared appealing from the DM point of view.

Some models currently under consideration are:

- WIMP is a relatively broad definition, and this means that several particles fall into this category. The most popular, and relevant for this work, is the lightest neutralino from the MSSM, described in Sec. 2.4.3. The neutralino is a mixed state, which means that its dominant component could be either wino, bino or higgsino. The calculation of the neutralino relic density depends heavily on which component is assumed to be dominant. Independently from its composition, the neutralino is a reliable DM candidate when it is also the LSP: it is massive, weakly interacting and, because of R-parity conservation, stable. Other possibilities for WIMPs include a DM scalar that couples to the SM through the Higgs boson or a more complicated dark sector linked to the SM by new vector particles, such as Z' bosons or hidden photons [74].

- Axions are also interesting DM candidates. We mentioned the strong CP problem in Sec. 2.1 and that the axions have been postulated to address this problem; axion-like particles (ALPs), similar to the axion but not necessarily solving the strong CP problem, are also being considered as DM candidates [82]. A detailed discussion about axions and ALPs is beyond the scope of this work, but it is worth mentioning their key features as DM candidates; axions are electrically neutral, so they are "dark", but are also very light particles, which means that their production has to be non-thermal in order for them to be non-relativistic as demanded by the CDM framework.

- As for the modified gravity theories, there is no outstanding case for a specific DM candidate to be favoured over the others. This also means that many other possibilities are being considered and that frequently, new candidates are proposed. A more detailed overview of possible candidates can be found in [83].

3.4 Simplified models

Considering a DM candidate in an already studied BSM scenario is clearly appealing from a theoretical point of view: finding the wanted particle would mean solving more than one issue at the same time and would constitute a step further towards the formulation of a unified theory of particle physics. Nevertheless, this approach has its drawbacks: complete BSM theories are complicated and, as we mentioned specifically for the MSSM case, they usually have many free parameters. Analysing the results

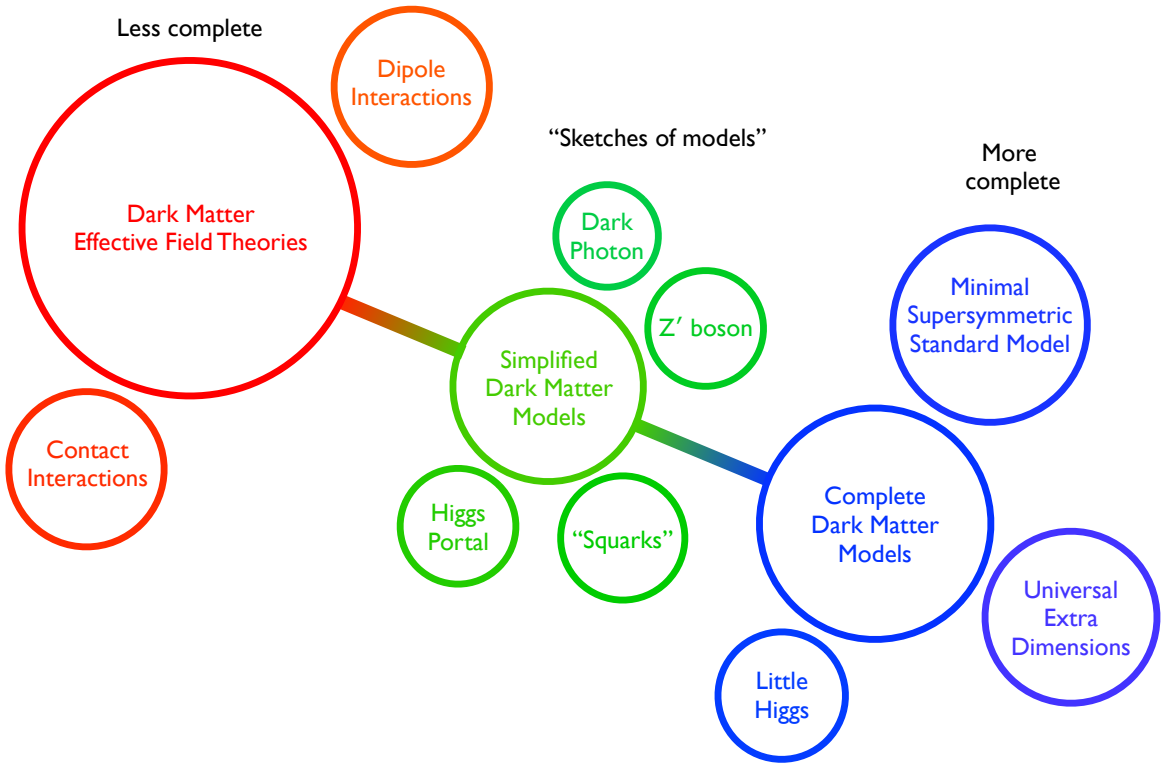

Figure 3.4: A pictorial representation of the DM theory space, highlighting that it is possible to choose not only different characteristics of the models, but also different degrees of complexity. Figure taken from [84].

is therefore much more complicated, and many aspects of the theories have small consequences on DM searches, if any at all. Given that we know very little about DM properties, a completely different approach is also worth consideration: using models that are as simple as possible, in order to deal with more manageable parameter spaces [84]. These models are not meant to be a complete description of BSM physics, but just provide a reasonable reproduction of DM phenomenology. Therefore, these models are likely to miss correlations between parameters and some theoretical aspects, i.e. the origin of the masses of the new particles, are left undetermined.

A pictorial representation of the DM model space is shown in Fig. 3.4, where the DM models are loosely divided in complete theories, simplified models and effective field theories. Complete theories, represented on the right hand side, represent the most complex end of the DM theory spectrum, which makes them less suitable for setting bounds on the DM parameters alone.

Simplified models, represented in the centre, are built specifically for DM, and they lack features of a complete BSM theory; usually, they include just a single DM particle and a mediator that constitutes its connection to the SM. They should be connected to a full theory, that is referred to as their UV-completion, but whose effects unrelated to DM are neglected. The Lagrangian associated with these models should respect all SM symmetries and eventually add new ones in case they are needed, e.g. in the case of a massive vector mediator, a new spontaneously broken $U(1)'$ symmetry has to be added to generate its mass. Often, these models are also required to have the same flavour changing neutral current structure as the SM, in order to avoid large flavour and CP violating effects; this is achieved by assuming minimal flavour violation (MFV) [84], which imposes contraints on the structure of the couplings between the new particles and the SM ones.

A further level of simplification is to consider effective field theories (EFTs), represented on the left-hand side. In EFTs, DM particles are considered to be the only accessible states and the interactions between DM and the SM are represented as point-like, integrating out possible heavy mediators. Thus, the EFTs are bound to break down at a high energy scale, but they are a useful tool in a low-energy framework, such as direct searches, that will be discussed in Sec. 3.5.

Two simplified models that have been used in this work will be described in the following sections. In both of these models, we will generally assume that the DM candidate is a Dirac fermion; this particle is a singlet under the SM gauge group, which means that additional fields will be necessary to mediate between the DM particles and the SM ones. Depending on the choice for the mediator, the resulting models will be substantially different; in particular, taking in consideration different mediators will result in different production modes for a DM pair and the resulting topologies are used to name the two models, see Fig. 3.6.

The names s- and t-channel model refer to the Mandelstam variables s and t, which are defined in the case of a $2 \to 2$ process and will often be referred to in this thesis. We will also refer to the third Mandelstam variable u. For a process in which the incoming particles are labelled a and b and the outgoing particles 1 and 2 (see Fig. 3.5), they are defined as:

$$s = (p_a + p_b)^2 = (p_1 + p_2)^2, \tag{3.21}$$
$$t = (p_a - p_1)^2 = (p_b - p_2)^2, \tag{3.22}$$
$$u = (p_a - p_2)^2 = (p_b - p_1)^2. \tag{3.23}$$

3.4.1 s-channel model

In our s-channel model, the interaction between DM and SM particles is mediated by a massive particle that can be either a scalar, a pseudoscalar or a vector. The mediator is also a singlet under the SM gauge group that only interacts with DM particles and the SM quarks; its mass generation mechanism is left undetermined. For a scalar or a pseudoscalar mediator, MFV requires its coupling to the quarks to be proportional to the quark masses; since the quarks are very light, the resulting cross sections for the relative processes will be heavily suppressed and the most relevant couplings between DM and SM involve top-quarks. A discussion of the potential signals arising from processes containing top-quark loops can be found in [84].

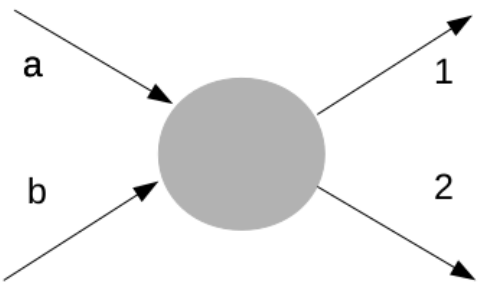

Figure 3.5: Sketch of a $2 \to 2$ process, in which the incoming particles are labelled a and b and the outgoing ones 1 and 2.

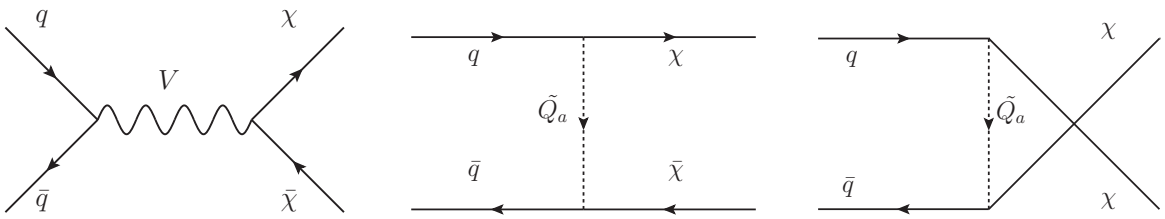

Figure 3.6: LO DM pair production processes at a collider for an s-channel model (left) and for a t-channel model (centre). In a t-channel model with a Majorana fermion, the u-channel process (right) would also be present. The Feynman diagrams present in this thesis have been generated using `JaxoDraw 2.0` [85, 86]

We instead focus on an s-channel model with a massive vector mediator, including also axial-vector components. The interaction terms in the Lagrangian of this model are [87]:

$$\mathcal{L}_V = \bar{\chi}\gamma^\mu \left[g_\chi^V - g_\chi^A\gamma_5\right]\chi V_\mu + \sum_q \bar{q}\gamma^\mu \left[g_q^V - g_q^A\gamma_5\right] q V_\mu, \tag{3.24}$$

where V denotes the vector mediator field, χ the fermionic DM field, q a quark field of a specific quark flavour, and $g_{\chi(q)}^{V(A)}$ the coupling strength between the vector (axial-vector) mediator and the DM particle (quark). The leading order (LO) production process in a collider is shown in Fig. 3.6.

3.4.2 t-channel model

In our t-channel model, instead, the mediators are assumed to be massive scalars that are coloured and flavoured, as they have to be in the same represention group as the quarks. The interaction terms in the Lagrangian are of the form [88–90]:

$$\begin{aligned}\mathcal{L}_{\tilde{Q}} &= -\left[\lambda_{Q_L}\bar{\chi}\left(\tilde{Q}_L^\dagger \cdot Q_L\right) + \lambda_{u_R}\tilde{Q}_{u_R}^*\bar{\chi}u_R + \lambda_{d_R}\tilde{Q}_{d_R}^*\bar{\chi}d_R + \text{h.c.}\right] \\ &= -\left[\lambda_{Q_L}\left(\tilde{Q}_{u_L}^*\bar{\chi}u_L + \tilde{Q}_{d_L}^*\bar{\chi}d_L\right) + \lambda_{u_R}\tilde{Q}_{u_R}^*\bar{\chi}u_R + \lambda_{d_R}\tilde{Q}_{d_R}^*\bar{\chi}d_R + \text{h.c.}\right],\end{aligned} \tag{3.25}$$

where $\tilde{Q}_{u_L}$, $\tilde{Q}_{d_L}$, $\tilde{Q}_{u_R}$, $\tilde{Q}_{d_R}$ are the scalar mediator fields, and $u_{L/R}$, $d_{L/R}$ are the left- and right-handed up- and down-type quarks. λ_{Q_L} is the Yukawa coupling for left handed quarks, which is equal for up- and down-type quarks, while λ_{u_R}, and λ_{d_R} are the couplings to the right-handed quark fields. $\tilde{Q}_L = (\tilde{Q}_{u_L}, \tilde{Q}_{d_L})^T$ and $Q_L = (u_L, d_L)^T$ are $\mathrm{SU}(2)_L \times \mathrm{U}(1)_Y$ doublets.

In this model, the DM particle has to be lighter than the mediators, otherwise a decay of the type $\chi \to \tilde{Q}q$ would be possible and χ, being unstable, would not be a good DM candidate. As previously stated, we generally consider χ to be a Dirac fermion, like in many experimental searches, but it is also interesting to study a t-channel model with a Majorana DM particle, because such a particle would then also be produced through a u-channel process, as shown in Fig. 3.6, with a potentially significant impact on the phenomenology of the model. Moreover, in this case the particle more closely resembles the supersymmetric neutralino, which is also a Majorana fermion.

Since simplified models are often understandable as a low-energy limit of a full theory, it is worth noticing that the MSSM and the simplified models that we have described in the last section present a similar DM candidate with similar production processes at a collider. The MSSM could therefore be interpreted as the UV-completion

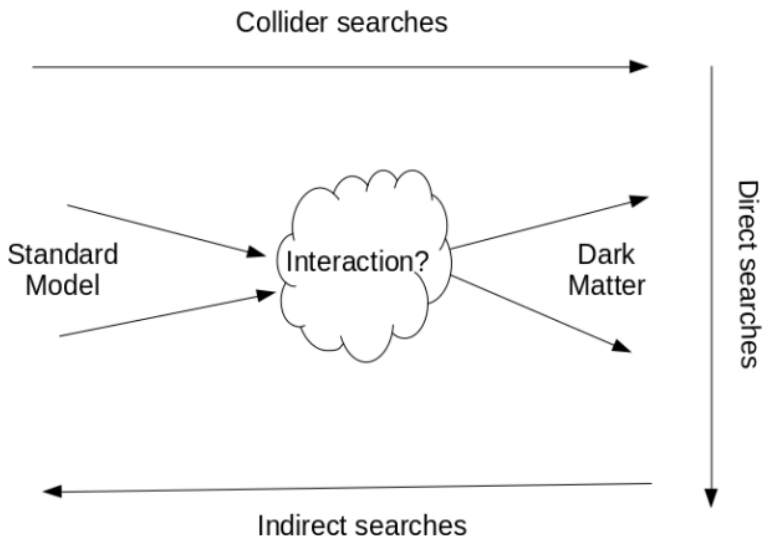

Figure 3.7: The different approaches in DM searches; observing the process from left to right would correspond to production of DM particles at a collider, from right to left to the observation of the results of DM annihilation (indirect detection) and from top to bottom the scattering of a DM particle off a SM target (direct detection).

of these simplified models. To investigate the soundness of this interpretation, we have compared the phenomenologies of simplified models and of the MSSM in one of our projects, which is described in Chap. 6.

3.5 Dark matter searches

Besides the theoretical considerations, a significant experimental effort is being carried out, aiming to find direct or indirect evidence of the existence of new particles that could constitute DM. Starting from the assumption that there is an interaction, however weak, between DM and SM particles, different approaches are applicable in order to find evidence for DM particles, schematically represented in Fig. 3.7. The main experimental strategies are described in the following sections. So far, no DM signal has been detected, but the different techniques have been used to set contraints on different areas of the considered parameter spaces of various DM models.

3.5.1 Indirect searches

Indirect searches aim to observe the products of DM annihilation into SM particles, i.e. a process observed from right to left in Fig. 3.7.

The average density of DM in the universe is very low, but should be significantly enhanced in the proximity of massive objects, such as the sun or the centre of galaxies. Therefore, in these regions there should be a significant amount of annihilation processes, which should give rise to an excess of pairs of photons or matter-antimatter pairs. The observation of this excess is in practice very difficult, as it is very hard to distinguish from the astrophysical background. The major hope relies on the observation of antimatter particles, which are far less common than matter particles or photons, or of very energetic electromagnetic radiation, such as gamma rays produced in the annihilation of two DM particles, for which also the background is considerably lower. The annihilation processes can be analysed considering the DM particles at rest, as

they are non relativistic and move slowly relative to galactic objects. An overview over the respective calculations can be found in [74] and references therein. Experiments looking for these kinds of excess include PAMELA [91], high-energy neutrino telescopes such as ANTARES [92] and gamma-ray telescopes, e.g. the Fermi gamma-ray Space Telescope [93].

3.5.2 Direct searches

Direct searches are trying to detect low-energy scattering events between nuclei and DM particles, i.e. a process observed from tom to bottom in Fig. 3.7.

In the hypothesis that our galaxy is submerged in a DM halo, there is a local density of DM particles ρ_0 everywhere in it, including the Earth. Thus, building a large detector, where the sources of background can be controlled, it could be possible to observe a few of this scattering events, even if the expected rate is very low. The rate depends on several factors, including the characteristics of the detector, but mostly on the cross section of these scattering events and on ρ_0. Assuming a fixed value for the local density of DM particles, limits on the cross section can be set. The direct detection experiments are usually built underground, to minimise the background caused by interference of cosmic rays, and use noble gases or cryogenic detectors. Such experiments include CRESST [28], XENON [29] and LUX [94], among many others. XENON and LUX both use a liquid xenon target chamber, while CRESST is based on cryogenic detectors using calcium tungstate ($CaWO_4$) crystals as absorbers. The different detectors allow to probe different regions of the DM parameter space; for example, CRESST is more sensitive to light DM, while XENON is used to test heavier DM candidates. The limits set by direct detection experiments have the advantage to be fundamentally model independent, as they represent upper limits on the scattering cross section between DM and SM particles as a function of the DM particle mass.

From the theoretical point of view, the low-energy nature of these events makes EFTs the most appropriate framework to study these interactions. The technical aspects of the relevant calculations are described in more detail in Chap. 7, which is dedicated to one of the projects contained in this thesis.

3.5.3 Collider searches

Another possibility would be to create DM particles in high energy collisions between SM particles, for example at the LHC [95], i.e. a process observed from left to right in Fig. 3.7.

If produced, however, the DM particles would escape the detectors because of their weak interactions with SM particles and therefore only an indirect signature of their production can be observed. If one or more visible particles are observed in the final state after DM particles have been produced, they will show an excess of transverse momentum. These particles are referred to as recoil particles and can be either jets, photons or vector bosons.

In the initial state of a collider process, the total transverse momentum p_T is zero, because the particles collide collinearly. Since during the collision p_T is conserved, the sum of the momenta of the detected final states can have a non-zero transverse component only if some particles produced must have escaped the detectors, with a certain amount of transverse momentum called missing p_T. However, DM particles are not the only source of missing p_T signatures in colliders. SM neutrinos lead to missing p_T signals and the detectors have a limited geometric range; therefore, the search for

DM at colliders consists in trying to disentangle any excess of missing p_T from the background due to SM particles and the technical features of the detectors. This is particularly difficult for low p_T regions, where the SM background is dominant.

Collider searches have been used to set limits on the DM parameter space. Differently from the direct detection case, these limits are heavily model-dependent, meaning that they rely on the specific model chosen and on the specific assumptions on the properties of the specific DM candidate. An example of the limits that can be set in the DM parameter space is shown in Fig. 3.8 by the ATLAS collaboration [95], where limits on the masses of the DM particle and of the mediator are shown in the case of the t-channel model.

Limits set in collider searches can also be reinterpreted in terms of direct searches. This procedure has to be performed with care, as there are some fundamental differences between the two approaches; guidelines are given in [96]. It is important to remember, as already mentioned, that also when translated into a direct detection parameter space, the collider limits remain model-dependent. Moreover, the DM relic density, which in the direct searches directly influences the number of expected events, has no impact on the collider searches. In general, for each different parameter space point in a specific model, the predicted relic density will be different and therefore, there is not a stable agreement between the predicted and the observed value. However, it can be assumed that mechanisms unrelated to the considered production mode are responsible for alternative DM annihilation processes in the early stages of the universe that bring the relic abundance to the correct value measured today.

Practically speaking, these translation is performed by calculating the DM-nucleon scattering cross section for parameter space points that have been excluded by collider searches. The exclusion plots obtained in this way will therefore depend on which expressions are used to calculate the cross section. In Chap. 7, we will perform this translation using the next-to-leading order (NLO) cross section that we have calculated in the context of simplified models.

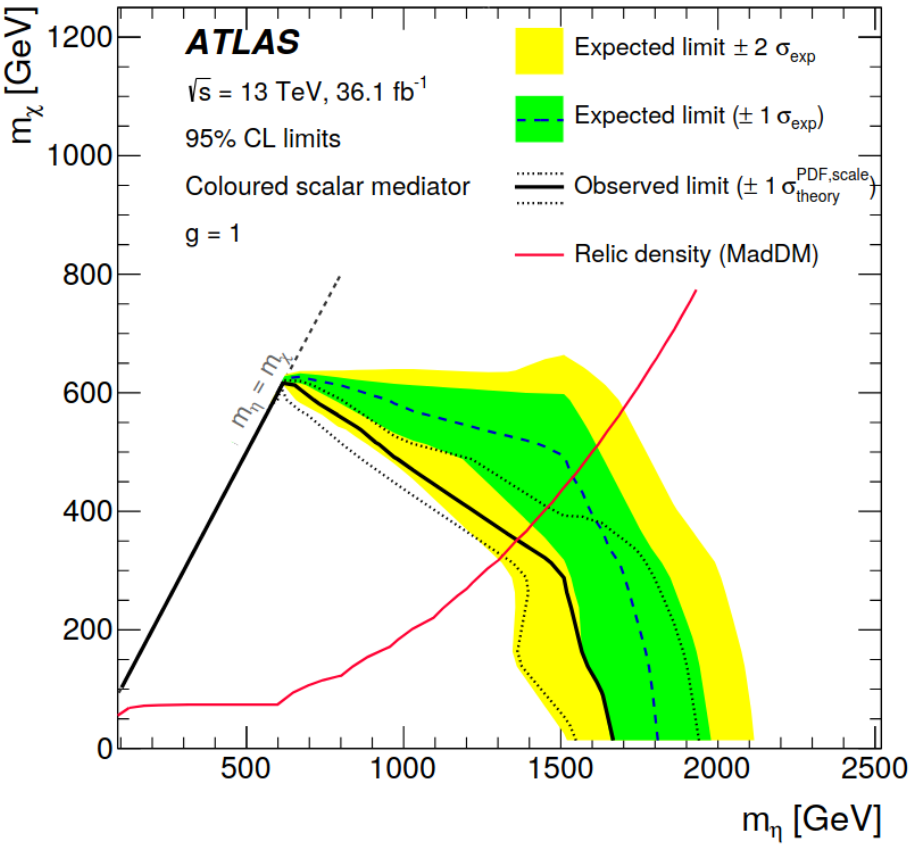

Figure 3.8: Exclusion limits for the simplified t-channel model with coupling set 1. Note that the relic density predicted by this model coincides with the observed one only by points marked by the red curve [95].

Chapter 4

Calculations in Quantum Field Theory

The precision calculations on which this thesis is based have been performed in the framework of perturbative quantum field theory (QFT). The necessary methods and techniques are described in this chapter, which will be the technical introduction to the work presented in Chaps. 5 and 6, and partially Chap. 7.

In Sec. 4.1, we will discuss how interactions at the partonic level are embedded into hadronic collisions. Then, in Sec. 4.2, we will discuss how next-to-leading order (NLO) calculations are performed in quantum chromodynamics (QCD) and some of the most relevant aspects concerning them. Ultraviolet divergences and infrared divergenes are discussed, respectively, in Secs. 4.3 and 4.4. Section 4.6 is a quick overview of parton showers (PS), which are necessary to provide more realistic simulations of hadronic events; the combination of NLO calculations and PS is discussed in Sec. 4.7, which is mostly dedicated to the POWHEG method.

4.1 Hadronic collisions

The production processes of SUSY particles and DM candidates happen at the partonic level, meaning that the interactions take place between quarks, gluons and other fundamental particles. Due to colour confinement, coloured partons cannot be observed in an isolated state, but are instead combined in colourless hadrons, such as protons. High energy processes involving coloured partons are usually studied in hadron colliders, which are the ones reaching the higher energies. To establish a connection between the hadronic cross sections and the partonic quantities that we will be calculating in the following chapters, it is necessary to know the composition of partons. Determining precisely the content of hadrons is a challenging task, since the interactions between partons in them, happenning at a low energy, cannot be described perturbatively. In the parton model, the interpretation of a proton as a bound state of two up-quarks and a down-quark - the so-called valence quarks - only holds for low energy probes. Already for collisions at energies higher than a few GeVs, a more complex substructure is revealed, in which there is a sea of additional quark-antiquark pairs and gluons.

In hadronic colliders, the momentum of the incoming hadrons is fixed, but the partons involved in the production of SUSY particles and DM particles will carry only a fraction of it. As we mentioned, the structure of hadrons cannot be studied with the perturbative techniques that we will discuss in the remainder of this chapter. However, the factorisation theorem [97] states that the non-perturbative and the perturbative regimes can effectively be separated. Therefore, the calculation of the partonic cross

section can be carried out without worrying about the low-energy regime and the description of the hadron structure necessary to determine the momenta carried by the partons does not directly affect the high-energy regime.

The necessary information about the structure of the hadrons is given by the parton distribution functions (PDFs), which are determined experimentally, and can be interpreted as the likelihood of finding a parton carrying a specific fraction of the momentum of the hadron at a specific energy. It is worth noting that the probabilistic interpretation of PDFs is helpful but somewhat simplistic and should therefore be treated cautiously. For example, when calculating NLO corrections, divergences may appear for a number of reasons. Some of them are removed by absorbing them into the PDFs, through a redefinition of the initial state (more details are given in Sec. 4.4). Moreover, PDFs can also assume negative values, which cannot be interpreted as probabilities. The PDFs are characteristics of a specific hadron and are then process independent.

Assuming that all the partons move in the same direction and are not interacting between them, the relation between the hadronic cross section and the partonic one is then given by:

$$d\sigma_{\text{had}} = \int_0^1 dx_1 \int_0^1 dx_2 \sum_{i,j} f_i(x_1, \mu_F) f_j(x_2, \mu_F) d\sigma_{ij\to n}(p_i, p_j), \tag{4.1}$$

where $d\sigma_{ij\to n}$ is the differential cross section relative to the scattering of the partons i and j into n final state particles, which depends on the momenta of the partons, p_i and p_j. The PDF $f_i(x_1, \mu_F)$ describes the probability of finding a parton i in the hadron 1 carrying a fraction x_1 of the total momentum of the hadron 1, at the energy μ_F, which is called the factorisation scale and is the energy at which the perturbative and non-perturbative regimes are separated. To obtain the total hadronic cross section, one has to sum over all the contributing partons and to integrate over the momenta fraction x_1 and x_2 from zero to one.

The partonic cross section can be written as:

$$d\sigma_{ij\to n} = \frac{1}{2s} d\Phi_n |\mathcal{M}_{ij\to n}|^2, \tag{4.2}$$

where $s = 2p_i \cdot p_j$ is the centre-of-mass energy squared and the flux factor $1/(2s)$ is obtained in the approximation of massless initial state particles. The Lorentz-invariant phase space element $d\Phi_n$ represents the necessity of integrating over all possible final-state configurations to obtain the total cross section. It can be written as:

$$d\Phi_n = (2\pi)^4 \delta^{(4)} \left(p_i + p_j - \sum_{k=1}^{n} p_k \right) \prod_{k=1}^{n} \frac{d\vec{p_k}^{\,3}}{(2\pi)^3 2p_k^0}. \tag{4.3}$$

Finally, the last unreferenced terms of Eq. (4.2) are the matrix elements squared $|\mathcal{M}_{ij\to n}|^2$. Because of the technical difficulties involved in their calculation, they are calculated perturbatively, expanding in the coupling strength of the considered interaction. The perturbative expansion can be truncated at leading order (LO), at next-to-leading order (NLO) or at even higher orders of perturbation theory. In this thesis, various matrix elements have been calculated up to NLO in the strong coupling. The technical requirements of such calculations are discussed in the following sections. There exist also frameworks in which the calculations in QFT are performed non-perturbatively, such as lattice-QCD [98], which are not the subject of this work.

4.2 NLO calculations

The matrix elements mentioned in the previous section are related to the interaction terms of the Lagrangian $\mathcal{L}_I$ of the model considered to study a specific process. The connection can be established starting from the scattering matrix $\hat{S}$, which is used to obtain the amplitude for a transition from the initial state i to the final state f:

$$S = \langle f|\hat{S}|i\rangle. \tag{4.4}$$

The operator $\hat{S}$ is defined as:

$$\hat{S} = \hat{T}\left[\exp\left(\int id^4x\mathcal{L}_I\right)\right], \tag{4.5}$$

where $\hat{T}$ is the time-ordering operator.

Eq. (4.5) is the basis of the perturbative expansion discussed in the previous section. Using the LSZ (Lehmann-Symanzik-Zimmermann) reduction formula [99], the matrix elements $\mathcal{M}_{ij\to n}$ are linked to the $\hat{S}$ matrix through:

$$\langle f|\hat{S}|i\rangle = \langle f|\mathbb{1}|i\rangle + \frac{i\mathcal{M}_{ij\to n}\delta^4(P_f - P_i)}{(2\pi)^3(2\pi)^{\frac{3n}{2}}}, \tag{4.6}$$

where the δ represents the momentum conservation, meaning that the initial state 4-momentum P_i and the final state one P_f have to be equal. The (2π) factors in the denominator come from the two initial state particles and the n final state ones, respectively. The particles i and j, as well as the n particles in the final state, must be on their mass shell. The term $\langle f|\mathbb{1}|i\rangle$ is the trivial part of the interaction, in which the initial and final state coincide.

In the perturbative approach, the Feynman rules are a particularly useful tool [100]. They are derived from the interaction terms of the Lagrangian and are used to read from Feynman diagrams the mathematical expressions corresponding to couplings, propagators and incoming and outgoing particles in the process of interest. In this way, the matrix elements and, consequently, the cross section of a scattering process can be calculated using the Lagrangian to draw Feynman diagrams up to the desired order in perturbation theory and then using the Feynman rules. The perturbative expansion is performed with respect to a specific coupling constant, e.g. to the strong coupling $\alpha_s = g_s^2/4\pi$, which therefore has to be small in order to keep the perturbative approach well-defined. The LO process will be the one in which the coupling appears as few times as possible, the NLO will have an additional occurrence of the coupling and so on. The size of the coupling constant also means that, with some exceptions [1], the LO cross section will be significantly larger than the other contributions. The running of the coupling constants results in the fact that the same interaction can or cannot be treated perturbatively depending on the energy scale: for example, we will consider NLO corrections to QCD in high energy scattering events, but the same techniques cannot be used to study PDFs in a low energy regime.

The NLO cross sections consists of the LO cross section, also called Born cross section, and real and virtual contributions, which represent the actual NLO corrections. The real corrections can be seen as the LO process with the emission of an additional

[1] In some cases, for example when new production channels are present at NLO, the corrections can be larger than the original LO cross section, as we will for example observe and discuss in our work, see Sec. 5.7.

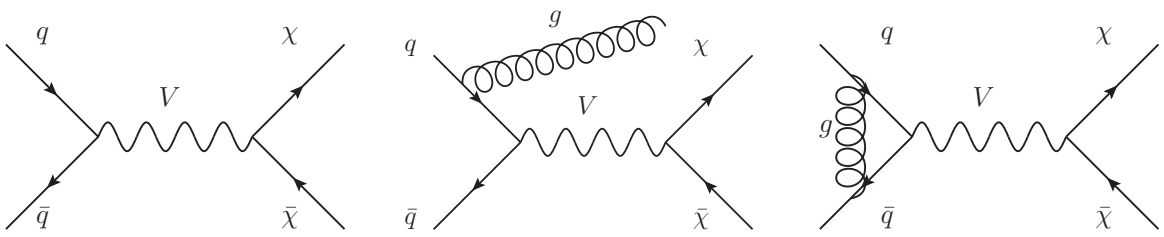

Figure 4.1: The LO Feynman diagram for an s-channel model (left) and the relative real (centre) and virtual (right) NLO-QCD corrections.

particle from the initial or the final state, while the virtual corrections are the LO process with an additional internal loop. The presence of the real corrections might be surprising: considering an additional particle in the final state effectively changes the nature of the process in consideration. However, they need to be taken into account. They are of the same order as the virtual corrections and, most importantly, the Kinoshita-Lee-Naunberg theorem [101, 102] states that only the sum of real and virtual corrections gives a finite results and is therefore the only meaningful quantity. This will be discussed in greater detail in Sec. 4.4.

An example is given in Fig. 4.1 using the s-channel model discussed in Sec. 3.4. We will be calculating NLO QCD corrections to this process: in the LO diagram, the strong coupling does not appear. It appears once in the real diagram, and twice in the virtual one. We label the corresponding matrix elements $\mathcal{M}_{LO}$, $\mathcal{M}_{\mathcal{V}}$ and $\mathcal{M}_{\mathcal{R}}$. A very important detail concerning the real corrections is that their final state has a different multiplicity: if the LO process has n particles in the final state, the real one will have $n+1$. This means that its phase space will be different and the respective integration has to be performed separately. At NLO, Eq. (4.2) can then be written as:

$$\sigma = \int d\Phi_n \frac{1}{2s} |\mathcal{M}_{LO} + \mathcal{M}_{\mathcal{V}}|^2 + \int d\Phi_{n+1} \frac{1}{2s} |\mathcal{M}_{\mathcal{R}}|^2. \tag{4.7}$$

The term on the right hand side is not, however, the NLO cross section. Expanding the term $|\mathcal{M}_{LO} + \mathcal{M}_{\mathcal{V}}|^2$, one obtains the following:

$$|\mathcal{M}_{LO} + \mathcal{M}_{\mathcal{V}}|^2 = |\mathcal{M}_{LO}|^2 + 2\Re[\mathcal{M}_{LO}\mathcal{M}_{\mathcal{V}}*] + |\mathcal{M}_{\mathcal{V}}|^2. \tag{4.8}$$

The last term does not actually belong to the NLO corrections, as it is proportional to a higher order of the coupling constant. For this reason, only the interference term between the Born and the virtual diagram is a genuine NLO correction. Eq. (4.7) becomes then:

$$\sigma_{NLO} = \int d\Phi_n \left\{ \frac{1}{2s} |\mathcal{M}_{LO}|^2 + 2\Re[\mathcal{M}_{LO}\mathcal{M}^*_{\mathcal{V}}] \right\} + \int d\Phi_{n+1} \frac{1}{2s} |\mathcal{M}_{\mathcal{R}}|^2. \tag{4.9}$$

The calculation of NLO corrections is complicated by the occurrence of divergences, that have to be dealt with to obtain finite and meaningful results.

4.3 Ultraviolet divergences

A first class of divergences that can appear in NLO amplitudes are the so-called ultraviolet (UV) divergences. They can appear while calculating diagrams containing

loops, like for example on the right side of Fig. 4.1. The origin of these divergences can be understood by looking at the Feynman rules corresponding to the presence of a closed loop. In most circumstances, the momenta of particles in Feynman diagrams are fixed, because they are connected to external momenta and constrained by momentum conservation. However, in a loop, an additional unconstrained momentum can flow, without any influence on the external, observable ones. To calculate the amplitude of Feynman diagrams containing loops, it is then necessary to integrate over all possible momenta flowing in the loop, meaning from zero to infinity.

The resulting integrals have, with great simplification, the following structure:

$$\int \frac{d^4k}{(2\pi)^4} f(k, p_1, p_2, \ldots, p_n) \prod_{i=0}^{n} \frac{1}{\left(\sum_{j=0}^{i} p_j - k\right)^2 - m_i^2 + i\epsilon}, \tag{4.10}$$

where k is the unconstrained loop momentum and the loop has n particles attached to it, with masses $m_i\,(i = 1, \ldots, n)$ and momenta $p_i\,(i = 1, \ldots, n)$. The $i\epsilon$ term is needed to regulate singularities of the denominator. The numerator function f contains a certain power of k, which may or may not be compensated by the powers of k present in the denominator. These integrals are often divergent for large values of the loop momentum, thus the name UV divergences. As a consequence of these divergences, the amplitude associated to a Feynman diagram containing such a loop could have an infinite result.

Non-finite results are obviously meaningless and cannot be used to interpret physical processes. However, the predictive power of QFT can be restored by removing these divergences, using sophisticated techniques that have been developed over the last decades.

4.3.1 Regularisation

The initial step in order to eliminate the divergences consists in identifying and isolating them through the procedure of regularisation. Different methods can be used, such as dimensional regularisation [103], dimensional reduction [104, 105], lattice regularisation [106] or Pauli-Villar regularisation [107]. In this work we will use dimensional regularisation, of which we will give a short description in this section. This scheme is commonly used because of its numerous advantages: it preserves all underlying symmetries of the theory, it preserves Lorentz invariance and it allows to easily identify the divergences.

The fundamental idea is to perform the integration over the loop momentum not in four dimensions, but in $D = 4 - 2\varepsilon$ dimensions, where ε is an arbitrarily small number. The substitution is performed as follows:

$$\int \frac{d^4k}{(2\pi)^4} \to \mu_R^{4-D} \int \frac{d^Dk}{(2\pi)^D}. \tag{4.11}$$

Performing the integration and then taking the $\epsilon \to 0$ limit, the divergences will appear as $1/\varepsilon^n$ poles, where n depends on the kind of original divergence, e.g. logarithmic or linear. μ_R is an arbitrary energy scale, called the renormalisation scale, which has to be inserted to keep the correct dimensionality of the result. The results obtained should be ultimately independent from μ_R but performing a perturbative expansion to a finite order usually spoils this independence; the leftover dependence from μ_R is usually called theoretical uncertainty.

The effectiveness of dimensional regularisation can be understood by looking, for example, at the so-called scalar one-point function A_0:

$$A_0(m) = \frac{(2\pi\mu_R)^{4-D}}{i\pi^2} \int d^D k \frac{1}{k^2 - m^2 + i\varepsilon}. \tag{4.12}$$

This integral diverges for $D = 4$. Carrying out the integration in D dimensions, however, one finds:

$$A_0(m) = m^2 \left(\log 4\pi - \log \frac{m^2}{\mu_R^2} + 1 - \gamma_E + \frac{1}{\varepsilon} \right) + \mathcal{O}(\varepsilon), \tag{4.13}$$

where γ_E is the Euler-Mascheroni constant and the terms of $\mathcal{O}(\varepsilon)$ are only relevant for calculations with multiple loops. The divergence of the integral has now been regularised, i.e. isolated as the $1/\varepsilon$ term. However, to obtain a sensible result, it is still necessary to remove it.

4.3.2 Renormalisation

The procedure removing the divergences to obtain finite results is called renormalisation and it consists in the redefinition of some of the parameters of the theory. In order to justify it, a physical interpretation of this procedure is necessary. When writing the Lagrangian of a model, the free parameters contained in it are assumed to coincide with the physically observables ones, e.g. the mass of a particle. This assumption holds at LO, but its shortcomings can be observed when looking at higher-order corrections, where indeed it leads to the appearance of divergences.

The idea of renormalisation is then to differentiate the parameters appearing in the Lagrangian, usually called bare parameters, and the observable, *renormalised* parameters. Since the bare parameters are not observable, they can incorporate all non-finite contributions, leaving the renormalised ones finite. It is worth noting the renormalisability of a theory is not a straightforward issue. A theory is renormalisable only if the number of parameters to renormalise at each order of perturbation theory is finite. The SM is renormalisable [108, 109], but many effective field theories (EFTs) are not.

Practically speaking, this means that the Lagrangian can be written as:

$$\mathcal{L}_0 = \mathcal{L} + \delta\mathcal{L}, \tag{4.14}$$

where $\mathcal{L}_0$ is the bare Lagrangian and $\mathcal{L}$ is the renormalised, or physical, one. They have the same structure, but $\mathcal{L}_0$ contains bare parameters and $\mathcal{L}$ renormalised ones. They are linked through $\delta\mathcal{L}$, which contains the new terms necessary to perform this operation, which are called *counterterms*. Counterterms can be calculated using specific Feynman rules and are represented by their corresponding Feynman diagrams; an example, relative to the quark self energy, is given in Fig. 4.2.

We mostly follow the approach described in [110]. Using multiplicative renormalisation, each free parameter is renormalised in the following way:

$$\phi_0 = Z_\phi^{1/2} \phi, \tag{4.15}$$

$$m_{p,0}^2 = Z_m^p m_p^2, \tag{4.16}$$

$$g_0 = Z_g g, \tag{4.17}$$

where ϕ is a scalar particle field, m_p the mass of a generic particle and g is a coupling constant. The terms on the left-hand side are the bare parameters. The various Z

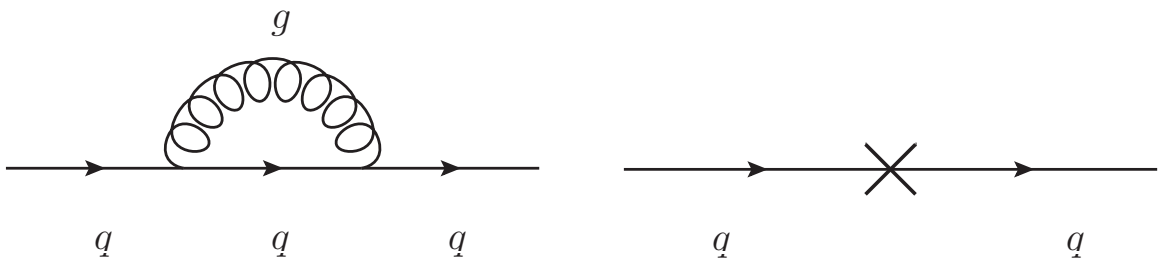

Figure 4.2: The quark self energy at NLO is given by the sum of the loop diagram (left), which contains a divergence, and of the opposite counterterm (right).

constants are the renormalisation constants and will contain the counterterms. To calculate NLO counterterms, one performs an expansion of the kind $Z = 1 + \delta Z$, and the previous equations are then written as:

$$\phi_0 = \left(1 + \frac{1}{2}\delta Z_\phi\right)\phi, \tag{4.18}$$

$$m^2_{p,0} = \left(1 + \delta Z^p_m\right) m^2_p, \tag{4.19}$$

$$g_0 = \left(1 + \delta Z_g\right) g. \tag{4.20}$$

The exact form of the δZ_i is not fixed. They must cancel the divergences contained in the bare terms, but they can also contain finite parts, that can be shifted between them and the renormalised ones. This is reflected in the existence of various renormalisation schemes, that have different advantages and characteristics and are usually chosen in specific contexts depending on the necessity. The results of a calculation to all orders in perturbation theory would not depend on the choice of the renormalisation scheme, but those of any calculation performed to any finite order will. This source of uncertainty is often referred to as theoretical uncertainty of the results.

The renormalisation schemes are usually chosen because of their simplicity or because they provide a clear physical interpretation. In this work we will use two different schemes, the $\overline{\text{MS}}$ scheme and the on-shell scheme, which represent, respectively, a minimal scheme and a more physical scheme.

The $\overline{\text{MS}}$ scheme

The $\overline{\text{MS}}$ scheme [111] is a slight complication over the so-called minimal subtraction (MS) scheme [112], in which only the UV divergences are absorbed in the counterterms. In the $\overline{\text{MS}}$ scheme the factor included in the counterterms is:

$$\Delta = \frac{1}{\varepsilon} - \gamma_E + \log 4\pi, \tag{4.21}$$

The clear advantage of this method is its simplicity, while its main drawback is that it does not offer a straightforward interpreation of the renormalised parameters.

Since the $\overline{\text{MS}}$ scheme is used in the PDF sets that we will use, we will also use it to renormalise the strong coupling constant α_s, with $\alpha_s = g_s^2/4\pi$. In particular, for the work discussed in Chap. 5, we follow the treatment of α_s discussed in [113]. Looking at Eq. (4.18), the relative renormalisation constant is:

$$g_{s,0} = (1 + \delta Z_{g_s}) g_s. \tag{4.22}$$

To compute δZ_{g_s}, any tree-level vertex containing a gluon can be used, so it is sufficient to focus on a single, particularly simple vertex based only on SM particles. These

representations are in general gauge dependent, and are written here in the Feynman-'t Hooft gauge. The simplest one originates from the three-gluon vertex:

$$\delta Z_{g_s} = -\frac{3}{2}\delta Z_{gg}|_{div} + \delta Z_{3g} + \delta Z_{\log}, \tag{4.23}$$

where $\delta Z_{gg}|_{div} = -\frac{3}{4\pi}\alpha_s\Delta$ and $\delta Z_{3g} = -\frac{3}{2\pi}\alpha_s\Delta$. The third term, $\delta Z_{\log}$ has a more involved origin and requires a separate discussion.

The strong coupling constant dependence on the renormalisation scale μ_R is governed by the renormalisation group equation of QCD [114]:

$$\mu_R^2 \frac{d}{d\mu_R^2}\alpha_s = \beta(\alpha_s) = -\alpha_s^2 \sum_n \beta_n \alpha_s^n, \tag{4.24}$$

where β is the β-function of QCD, which practically determines the running of α_s and depends on the number of particles considered and on the colour factors symmetry of QCD. This means that in principle both heavy and light particles are contributing to this evolution if not decoupled explicitely. This could lead to the presence of large logarithms if the scale μ_R is much different from the masses of some of the heavy particles.

In the SUSY calculation that we will perform, the term $\delta Z_{\log}$ is added to the counterterm δZ_{g_s}, to decouple some heavy coloured particles, namely the squarks with masses $m_{\tilde{q}_i}$, the gluino with mass $m_{\tilde{g}}$, the top quark with mass m_t and the bottom with mass m_b. The expression for $\delta Z_{\log}$ then yields [115]:

$$\delta Z_{\log} = -\frac{\alpha_s}{8\pi}\left[\frac{1}{6}\sum_{i=1}^{12}\log\frac{m_{\tilde{q}_i}}{\mu_R^2} + 2\log\frac{m_{\tilde{g}}^2}{\mu_R^2} + \frac{2}{3}\log\frac{m_t^2}{\mu_R^2} + \frac{2}{3}\log\frac{m_b^2}{\mu_R^2}\right]. \tag{4.25}$$

The on-shell scheme

The on-shell (OS) scheme is a non-minimal renormalisation scheme in which mass parameters are renormalised in such a way that they correspond to the physical masses.

The advantage of this scheme is that it provides a more intuitive interpretation of the renormalised parameters. Its drawback is that its formulation is not as simple as the $\overline{\text{MS}}$ one. Moreover, it is not well suited for some non-directly measurable parameters, e.g. the mass of the bottom quark. The problem is that the bottom quark cannot be observed isolated and therefore its mass cannot be measured directly. The mass of the top quark, instead, can be measured, since it decays before forming hadrons, and is therefore renormalisable using the OS scheme.

From the practical point of view, choosing the on-shell renormalisation condition means taking the zeros of the one-particle irreducible two-point functions to be equal to the renormalised parameters. Such functions are, for a boson B, a fermion F or a vector V, respectively [110]:

$$\begin{aligned}\hat{\Gamma}^F(k) =& i(\not{k} - m_F) + i\left[\not{k}\left(P_L\hat{\Sigma}^{F,L}(k^2) + P_R\hat{\Sigma}^{F,R}(k^2)\right)\right] \\ &+ im_F(P_L + P_R)\hat{\Sigma}^{F,S}(k^2),\end{aligned} \tag{4.26}$$

$$\hat{\Gamma}^B(k) = i(k^2 - m_B^2) + i\hat{\Sigma}^B(k^2), \tag{4.27}$$

$$\hat{\Gamma}^V_{\mu\nu}(k) = -ig_{\mu\nu}(k^2 - m_V) - i\left(g_{\mu\nu} - \frac{k_\mu k_\nu}{K^2}\right) - i\frac{k_\mu k_\nu}{k^2}\hat{\Sigma}^V_L(k^2). \tag{4.28}$$

where $P_{L/R} = \frac{1\mp\gamma_5}{2}$ are the chirality projectors and the renormalised self energy functions $\hat{\Sigma}$ is equal to:

$$\hat{\Sigma}(k^2) = \Sigma(k^2) - \delta m^2 + (k^2 - m^2)\delta Z, \tag{4.29}$$

where Σ is the unrenormalised self energy function of the relative particle. Taking the zeros of these functions leads to the renormalisation conditions:

$$\Re\left(\hat{\Gamma}^F(k)u(k)|_{k^2=m_F^2}\right) = 0, \tag{4.30}$$

$$\Re\left(\hat{\Gamma}^B(k)\right) = 0, \tag{4.31}$$

$$\Re\left(\hat{\Gamma}^V\mu\nu(k)\epsilon^\nu(k)|_{k^2=m_F^2}\right) = 0, \tag{4.32}$$

where ϵ^ν is the polarisation vector corresponding to the vector V and u is the spinor corresponding to the fermion F. The masses appearing in these equations are the physical masses. Strictly speaking, the $\Re$ symbol in the expressions above takes the real part of the loop integrals, but not of the quark mixing matrix elements. This will not affect our calculation since we will assume the quark mixing matrix to be real. Additionally, to simplify the resulting expressions, we will also require on-shell conditions for the field renormalisation matrices. In practical terms, this means that the renormalised one-particle irreducible two-point functions are diagonal if the external lines are on their mass shell, leading to the additional conditions:

$$\lim_{k^2\to m_F^2} \frac{\not{k} + m_F}{k^2 - m_F^2}\Re\left(\hat{\Gamma}^F(k)u(k)\right) = 0, \tag{4.33}$$

$$\lim_{k^2\to m_B^2} \frac{1}{k^2 - m_B^2}\Re\left(\hat{\Gamma}^B(k)\right) = i, \tag{4.34}$$

$$\lim_{k^2\to m_V^2} \frac{1}{k^2 - m_V^2}\Re\left(\hat{\Gamma}^V_{\mu\nu}(k)\epsilon^\nu(k)\right) = -i\epsilon_\mu.(k) \tag{4.35}$$

Thus the explicit expressions for the renormalisation constants can be finally written as:

$$\delta m_F = \frac{1}{2} m_F \Re\left(\Sigma^{F,L}(m_F^2) + \Sigma^{F,R}(m_F^2 + 2\Sigma^{F,S}(m_F^2))\right), \tag{4.36}$$

$$\begin{aligned}\delta Z_F^{L/R} =& -\Re\left(\Sigma^{F,L/R}(m_F^2)\right) \\ & - m_F^2 \frac{\partial}{\partial k^2}\Re\left(\Sigma^{F,L}(k^2) + \Sigma^{F,R}(k^2 + 2\Sigma^{F,S}(k^2))\right)|_{k^2=m_F^2},\end{aligned} \tag{4.37}$$

$$\delta m_B^2 = \Re\left(\Sigma^B(m_B^2)\right), \tag{4.38}$$

$$\delta Z_B = \Re\left(\frac{\partial\Sigma^B(k^2)}{\partial k^2}|_{k^2=m_B^2}\right), \tag{4.39}$$

$$\delta m_V^2 = \Re\left(\Sigma_T^V(m_V^2)\right), \tag{4.40}$$

$$\delta Z_V = \Re\left(\frac{\partial\Sigma_T^V(k^2)}{\partial k^2}|_{k^2=m_V^2}\right). \tag{4.41}$$

4.4 Infrared divergences

A different kind of divergences arising in NLO calculations are the so-called *infrared* (IR) divergences. This name is due to the fact that, differently from the first class of divergences that we discussed, these can happen for low, or at least finite, values of momenta in internal loops or of external particles. In particular, there are two classes

of such divergences: soft divergences, that take place in loops when the momentum of a massless particle approaches zero or for external massless particles emitted with vanishing momentum, and collinear divergences, in which external particles are emitted with momentum parallel to the one of the emitting particles. An in-depth discussion of IR divergences was made by Landau in [116].

An example of the origin of such divergences can be obtained by looking at the diagram in Fig. 4.3, representing the real emission of a gluon from a massless quark in the final state. If p is the momentum of the initial-state quark and k the momentum of the gluon, with p_0 and k_0 being the respective time components, the propagator of the quark before the emission is proportional to:

$$\frac{1}{(p+k)^2} = \frac{1}{2\,p\cdot k} = \frac{1}{2\,p_0 k_0(1-\cos\theta)}, \tag{4.42}$$

where the on-shell condition is for the massless particles $p^2 = k^2 = 0$. θ is the angle between the momenta of the two particles. This expression can give both a *soft* divergence, for $k_0 \to 0$, and a *collinear* one, when $\theta \to 0$. These limits will be approached when performing the integral over the phase-space, thus triggering the appearance of the divergences. A similar structure will appear in the calculation of loops in the virtual corrections, e.g. in the left-hand side diagram of Fig. 4.2, where besides the already discussed UV divergences for large values of the loop momentum, there will be also IR divergences for small values of it.

To obtain a finite and sensible result, these divergences also have to disappear. This is guaranteed, as anticipated, by the KLN theorem, that states that all measurable quantities will remain finite when a sum over all possible initial and final states containing such divergences is performed, thus meaning that, considering both virtual and real corrections in this sum, the divergences will cancel out. Soft divergences have to be regularised; one further advantage of the dimensional regularisation scheme that we are using for the UV divergences is that it is also effective on IR divergences. Collinear divergences originating from massless particles in the initial state will be incorporated into the PDFs, more precisely into their scale dependence. This is possible due to factorisation theorem [97] that we mentioned in Sec. 4.1.

In practical terms, the cancellation turns out to be very difficult, because the virtual and real corrections are integrated over different phase-spaces and these integrations are usually performed numerically using Monte Carlo methods. Numerically integrating multiple divergent terms separately and then summing them is actually practically impossible. For this reason, some so-called subtraction schemes have been developed. Examples are the Catani-Seymour method [117], the phase space splicing method [118] and the antenna method [119, 120]. However, we will focus on the Frixione-Kunszt-Signer (FKS) [121, 122] method, which is implemented in the `POWHEG-BOX` [23–25]. This framework will be described in Sec. 4.7. A quick overview of the FKS subtraction

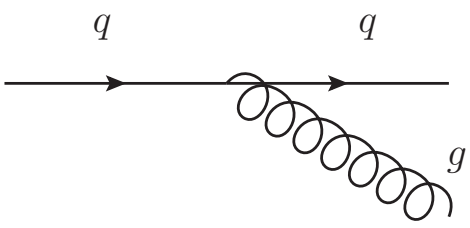

Figure 4.3: The emission of a quark possibly leading to an IR divergence.

method is instead given in the following section. The detailed description of its implementation in the POWHEG-BOX is given in [24, 25], which are the basis for the following discussion.

4.5 The Frixione-Kunszt-Signer subtraction method

The idea of the subtraction formalisms previously mentioned is to introduce counterterms $\mathcal{C}$ that behave as the real corrections in the soft and collinear limits. The specific form of $\mathcal{C}$ will depend on the specific subtraction method chosen, but in general these counterterm are introduced in the NLO cross section (Eq. (4.7)) as:

$$\sigma_{NLO} = \int d\Phi_n \left[\mathcal{B}_n + \mathcal{V}_n + \int d\Phi_1 \mathcal{C}_{n+1}\right] + \int d\Phi_{n+1} \left[\mathcal{R}_{n+1} - \mathcal{C}_{n+1}\right], \tag{4.43}$$

where we have, for simplicity, not reported the flux factor and slightly altered the notation from Eq. (4.7) to make it more readable. $\mathcal{B}_n$, $\mathcal{V}_n$ and $\mathcal{R}_{n+1}$ are the Born, the virtuals and the reals contributions respectively. The term $\int d\Phi \mathcal{C}_{n+1}$ has been added and subtracted, leaving the total cross section unaltered. In this way, the soft and collinear divergences of the real contributions are cancelled. The term $\int d\Phi_1 \mathcal{C}_{n+1}$ has to be integrable analytically.

In the FKS method, the shape of the counterterm is determined by splitting the real corrections into several regions, each including at most one singular contribution. To this end, the functions $\mathcal{S}$ are introduced, defined as:

$$\mathcal{R} = \sum_i \mathcal{R}_i + \sum_{ij} \mathcal{R}_{ij} = \sum_i \mathcal{R}\mathcal{S}_i + \sum_{ij} \mathcal{R}\mathcal{S}_{ij}, \tag{4.44}$$

where the first sum is associated with the final state parton i becoming soft or collinear to an initial state parton, and the second sum is associated to collinear divergences originated by two final state partons, i and j. The case $i = j$ is excluded. For non singular regions, the $\mathcal{S}$ functions are equal to zero. To conserve the amplitude of the real corrections, these functions have to fulfill the condition:

$$\sum_i \mathcal{S}_i + \sum_{ij} \mathcal{S}_{ij} = 1. \tag{4.45}$$

The $\mathcal{S}$ functions have the following properties:

$$\lim_{k_m^0 \to 0} \left(\mathcal{S}_i + \sum_j \mathcal{S}_{ij}\right) = \delta_{im}, \tag{4.46}$$

$$\lim_{\vec{k}_m \| \vec{k}_{1,2}} S_i = \delta_{im}, \tag{4.47}$$

$$\lim_{\vec{k}_m \| \vec{k}_{1,2}} S_{ij} = 0, \tag{4.48}$$

$$\lim_{\vec{k}_m \| \vec{k}_l} \left(\mathcal{S}_{ij} + \mathcal{S}_{ji}\right) = \delta_{im}\delta_{jl} + \delta_{jm}\delta_{il}, \tag{4.49}$$

which have the following meaning:

- Eq. (4.46) means that in the region where the parton m is soft, all the $\mathcal{S}_i$ and $\mathcal{S}_{ij}$ functions are zero, except the $\mathcal{S}_m$ function;
- Eq. (4.47) means that if the parton m is collinear to one of the two initial state partons, labelled 1 and 2, again all other $\mathcal{S}_i$ are zero. Eq. (4.48) means that in this case, also all $\mathcal{S}_{ij}$ functions are zero.

- Eq. (4.49) means that if the parton m is collinear to the parton l, only one of S_{ml} and S_{lm} is non-zero as m and l cannot be equal, thus agreeing with Eq. (4.45).

The specific form of the $\mathcal{S}$ functions and the contributions to the cross sections can be found in Sec. 2.4 of [24].

4.6 Parton showers

To improve the simulation of hadronic collisions, an additional characteristic of coloured partons has to be considered. Coloured particles like quarks and gluons can radiate additional coloured particles, which can in turn radiate even more, leading to a cascade of coloured particles, a so-called parton shower (PS). In principle, each further emission is suppressed by an additional factor α_S, which should quickly make these contributions negligible. However, this suppression can be compensated by large logarithmic factors, which make the PS effects sizeable. To include them, the leading logarithmic contributions to all order are resummed to the fixed-order calculation. It is worth noting that this approach is still based on perturbation theory, meaning that it has only a limited range of validity, i.e. energy scales above 1 GeV. The study of lower energy effects that are relevant for experimental purposes, like hadronisation, i.e. the transition from partons to hadrons and the subsequents decays, requires a different treatment. An introduction to some of the additional topics involved in realistic simulations of hadronic collisions can be found in [123].

Practically speaking, the starting point of the PS is the kinematic configuration of the hard process and additional partons are attached as emissions of initial and final state coloured particles, using a Monte Carlo generator and therefore a probabilistic approach that is described in the following.

There are two possibilities for these emissions: a gluon can split into a quark-antiquark pair or a quark can emit a gluon. Both processes can be formally seen as $1 \to 2$ processes, where we can call the mother particle a and the daughters b and c. The probability of having such splitting reads [23]:

$$dP_a = F_a(z,t)dzdt = \sum_b \frac{\alpha_S(Q)}{2\pi}\hat{P}_{ba}(z)\frac{dt}{t}dz, \tag{4.50}$$

where z is the fraction of momentum carried away by the parton b and, if E is the energy of the incoming parton a and θ the angular separation between b and c, $t = E^2\theta^2$. Note however, that the expressions for z and t are not fixed and different choices as possible, leading to different shower algorithms. The $\hat{P}_{ba}(z)$ are the Altarelli-Parisi splitting functions, which describe the branching of a parton into two new partons and depend on the specific process. The relevant expressions can be found in [23].

Using Eq. (4.50), the probability of having no branching between the scales t_i and t_0, $\Delta_a(t_i, t_0)$ can be built. We need to consider unitarity, meaning that in a certain energy range, a splitting has either happened or not, and the sum of the respective probabilities has to be equal one. Keeping in mind the definition of Δ, we can also write the probability that the splitting $a \to b, c$ occurs when no splitting took place before. This yields:

$$\Delta_a(t_i, t_0) + \int_{t_0}^{t_i} \Delta_a(t_i, t)F_a(z,t)dtdz = 1. \tag{4.51}$$

Inserting iteratively the expression for Δ into the integral, we can solve this equation for $\Delta_a(t_i, t_0)$:

$$\begin{aligned}\Delta_a(t_i,t_0) &= 1 - \int_{t_0}^{t_i} \Delta_a(t_i,t) F_a(z,t) dt dz \\ &= 1 - \int_{t_0}^{t_i} F_a(z,t_1) dt_1 dz + \int_{t_0}^{t_i} dt_1 \int_{t_0}^{t_1} \Delta_a(t_i,t_2) F_a(z_2,t_2) F_a(z_1,t_1) dt_2 dz_1 dz_2 \\ &= ... \\ &= \exp\left[- \int_{t_0}^{t_i} F(z,t) dz \right] . \end{aligned} \tag{4.52}$$

The quantity $\Delta_a(t,_t 0)$ is called the Sudakov form factor and is a fundamental building block of the shower algorithm:

$$\Delta_a(t,t_0) = \exp\left[- \sum_b \int_{t_0}^{t} \frac{dt'}{t} \int \frac{\alpha_S(t')}{2\pi} \hat{P}_{ba}(z) dz \right] . \tag{4.53}$$

Using the expressions just described, the shower Monte Carlo works typically in the following way:

- for parton a, a random number r, between zero and one, is chosen;
- the equation $\Delta_a(t, t_0) = r$ is solved for t. The shower is terminated when t is smaller than an appropriate cut-off energy Q_0, which is the scale at which non-perturbative effects take over, as explained above;
- if $t > Q_0$, a splitting of the form $a \to b$, c has occured, and z is generated using $F_a(z, t)$. Additionally, a random angle ϕ is chosen in the interval $[0, 2\pi]$.
- the process is repeated for the newly generated partons, b and c. Usually, the subsequent splittings are subject to some constraints: in angular-ordered shower algorithms, for each new emission, the angle θ has to be smaller than the ones of previous splittings.

The combination of NLO results with PS is a highly non-trivial task. In particular, simply adding PS contributions obtained as we just described on top of an NLO calculation, would lead to the double counting of some contributions. Both approaches would in fact produce terms that are interpretable as real-emissions in the collinear limit. For this reason, usually part of the PS results has to be subtracted. This is done, for example, in the MC@NLO framework [124]. We will instead focus on a different method, the POWHEG method, which will require some modifications to the PS algorithm discussed so far and is shortly reviewed in the following section. The full discussion of this method is given in Refs. [23–25]

4.7 The POWHEG method

The POWHEG method (POsitive Weight Hardest Emission Generator) is an approach used to match NLO calculations and PS effects. To understand this procedure, we

must start from the definition of the expectation value of an observable $\mathcal{O}$ at NLO. Using the notation of Eq. (4.43):

$$\langle \mathcal{O} \rangle_{NLO} = \int d\Phi_n \mathcal{O}_n \left[\mathcal{B}_n + \mathcal{V}_n + \int d\Phi_1 \mathcal{C}_{n+1} \right] + \int d\Phi_{n+1} \left[\mathcal{R}_{n+1} \mathcal{O}_{n+1} - \mathcal{C}_{n+1} \mathcal{O}_n \right]. \tag{4.54}$$

The expectation value for the same observable can also be written from the PS point of view, starting from the hard process with n particles in the final state, i.e. the underlying Born process. It will be the sum of two terms, one for which no emission happened, and one for which there was an additional emission:

$$\langle \mathcal{O} \rangle_{PS} = \int d\Phi_n \mathcal{B}_n \left[\mathcal{O}_n \Delta(t_i, t_0) + \int d\Phi_1 \mathcal{O}_{n+1} \Delta(t, t_0) F(z, t) \right]. \tag{4.55}$$

Applying directly Eq. (4.55) to Eq. (4.54) would lead to a double counting of the terms already discussed in the previous section. For this reason, the PS is instead applied to a modified NLO cross section [24]:

$$\begin{aligned} \langle \mathcal{O} \rangle_{NLO}^{sub} = & \int d\Phi_n \mathcal{O}_n \left[\mathcal{B}_n + \mathcal{V}_n + \int d\Phi_1 \mathcal{C}_{n+1} \right] \\ & + \int d\Phi_{n+1} \left[\mathcal{B}_n F(z,t) - \mathcal{C}_{n+1} \right] \mathcal{O}_n \\ & + \int d\Phi_{n+1} \left[\mathcal{R}_{n+1} - \mathcal{B}_n F(z,t) \right] \mathcal{O}_{n+1}. \end{aligned} \tag{4.56}$$

To simplify this expression, $F(z,t)$ can be defined as $\mathcal{R}_{n+1}/\mathcal{B}_n$, which will make the term in the third line vanish. This requires a modification of the Sudakov factor, which previously included the Altarelli-Parisi splitting kernels Eq. (4.50). The definition of the Sudakov factor in the POWHEG method is:

$$\Delta(p_T) = exp \int d\Phi_1 \frac{\mathcal{R}_{n+1}}{\mathcal{B}_n} \Theta(k_T - p_T), \tag{4.57}$$

where k_T is the momentum of the emitted parton and p_T is the usual cut-off momentum that represents the stopping point of sthe shower algorithm.

This means that now the ratio between the real corrections and the Born expression is used as a splitting kernel and, instead of being angular-ordered, the subsequent radiations are p_T ordered, meaning that the transverse momentum of the first parton emitted will be the highest, and the partons emitted afterwards will have smaller p_T. This is compatible with most PS programs, because even if they proceed in an angular-ordered way, it is possible to veto further splittings with higher p_T.

To write the POWHEG master formula in a compact form, we define the $\tilde{\mathcal{B}}$ function, which contains the elements of the NLO cross section, as:

$$\tilde{\mathcal{B}} = \left[\mathcal{B}_n + \mathcal{V}_n + \int d\Phi_1 \mathcal{C}_{n+1} \right] + \int d\Phi_1 \left[\mathcal{R}_{n+1} - \mathcal{C}_{n+1} \right]. \tag{4.58}$$

The POWHEG master formula for the cross section is then:

$$\sigma = \int d\Phi_n \tilde{\mathcal{B}} \Delta(p_{T_{min}}) + \int d\Phi_{n+1} \tilde{\mathcal{B}} \Delta(k_T) \frac{\mathcal{R}_{n+1}}{\mathcal{B}_n} \Theta(k_T - p_{T_{min}}). \tag{4.59}$$

Since many features of the POWHEG method are process independent, they have been implemented in the public framework of the `POWHEG-BOX` [25].

This program requires from the user the input of all the necessary process-specific elements, which are [125]:

- The flavour structures of the Born and of the real processes;
- The Born phase space;
- The Born squared amplitude, the colour correlated ones and the spin correlated ones;
- The real matrix elements;
- The finite part of the virtual corrections, which can be computed in dimensional regularisation or in dimensional reduction;
- The Born colour structures.

Moreover, some additional modifications of the program might be necessary to deal with additional complications like, for example, on-shell resonances. This will be discussed in detail in the following Chap. 5.

The `POWHEG-BOX` contains, in a `FORTRAN` framework, all the necessary process independent elements. It finds automatically all the regions containing divergences and builds the soft and collinear counterterms to remove them using the FKS method. The program MINT [126] is used to perform the Monte Carlo integration of the $\tilde{\mathcal{B}}$ function (Eq. (4.58)) over the Born and the real phase space, which is generated by the `POWHEG-BOX`. The result of this integration is the NLO cross section. Moreover, it is possible to calculate the differential distributions for any variable of interest. Finally, the `POWHEG-BOX` generates the hardest emission according to the Sudakov factor of the POWHEG method (Eq. (4.57)) and writes the resulting events in the standard Les Houches format [127], which is readable by most PS programs to shower these events as described in Sec. 4.6. In the works contained in Chaps. 5 and 6 we used for this purpose the program PYTHIA [21, 22].

Chapter 5

Weakino-squark production at hadron colliders

In Chap. 4, we described the main features of an NLO calculation and the POWHEG-BOX framework. In this chapter, we discuss our POWHEG-BOX implementation of the weakino-squark production processes at NLO in SUSY-QCD, focusing on the process specific features of our implementation and on the treatment of the on-shell resonances. A public version of this code will be made available through the POWHEG-BOX website [1].

This class of processes presents interesting experimental signatures, as it includes a coloured particle in the final state, the squark, which can give rise to a hard jet through its strong-interaction induced decay. Moreover, the weakino produced can be, or decay into, the lightest neutralino $\tilde{\chi}_1^0$, which is an interesting dark matter candidate, as already discussed in Sec. 2.4.3. The production of highly energetic weakinos in the final state can therefore lead to large quantities of missing transverse energy.

This chapter is based on Ref. [20]. We present here a more detailed discussion of our calculation, describing in full detail all the ingredients necessary to deal with the on-shell resonances, with methods similar to those described in Refs. [113, 128–130]. To conclude this chapter, we present a short phenomenological study to illustrate the capabilities of our code, again expanding the discussion from Ref. [20].

5.1 Born contributions

The LO processes diagrams for weakino-squark production are shown in Fig. 5.1. These representative diagrams show that two kinds of topologies occur: s-channel processes mediated by a quark and t-channel processes mediated by a squark. In both cases, the initial state consists of a gluon and a quark. The weakino in the final state can be either a neutralino or a chargino. A neutralino-squark final state will be characterised by a squark that has the same flavour as the corresponding initial state quark, e.g. $gd \to \chi_i^0 \tilde{d}_a$, where the index $a = 1, 2$ represents the chirality index of the squark. The index $i = 1, ..., 4$ indicates the kind of neutralino produced. A chargino-squark final state will instead exhibit a squark of a different flavour, e.g. $gd \to \chi_i^- \tilde{u}_a$. In this case, $i = 1, 2$, as there are only two kinds of charginos.

Left- and right-handed squarks are not mass eigenstates, but the mixing of these fields is proportional to the mass of the respective quark. Since we consider five massless quarks in the initial state, we are allowed to treat the left- and right-handed squarks as mass eigenstates. We consider the CKM matrix to be diagonal.

[1] http://powhegbox.mib.infn.it.

We are considering the production of squarks and antisquarks of the first two generations and of all kinds of weakinos, leading to a large number of independent channels. For neutralino-squark production, the four flavours of squarks and antisquarks can be produced both left- and right-handed, leading to 16 production channels for each neutralino and therefore to 64 channels in total, considering the four neutralinos. For chargino-squark production, only left-handed squarks and anti-squarks are produced at the considered order of perturbation theory, as the quark-squark-chargino vertex, necessary to have a two-to-two process as seen in Fig. 5.1, only exists for left-handed squarks. Thus, considering the four flavours of squarks and the two charginos and their respective antiparticles, there are 32 channels for chargino-squark production.

The LO amplitudes have been generated using a tool based on `MadGraph 4` [131–133], included in the `POWHEG-BOX`. This tool also provides spin- and colour-correlated amplitudes, that are necessary in order to use the automated version of the FKS subtraction algorithm implemented in the `POWHEG-BOX`. To cross-check our results, we verified that these amplitudes were equivalent to those generated using `FeynArts 3.9` [134] and `FormCalc 9.4` [135] with the MSSM-CT model file from [136].

As discussed in Chap. 4, at next-to-leading order (NLO) in the strong coupling α_s, virtual and real-emission corrections have to be computed and are discussed in the following sections.

5.2 Virtual corrections

The virtual diagrams have also been generated using `FeynArts 3.9` and `FormCalc 9.4` [135] with the MSSM-CT model file from [136].

The virtual corrections include loop corrections to each vertex of the two LO diagrams and box corrections. There are also self-energy corrections for the intermediate quark of the s-channel diagram and for the intermediate squark of the t-channel diagram. Representative diagrams are shown in Fig. 5.2. Compared to the LO diagrams, the only new particle appearing in these diagrams is the gluino. The virtual diagrams have been generated using the same tools used to generate the Born ones, `FeynArts 3.9` and `FormCalc 9.4`, using the same MSSM-CT model file.

Since these diagrams are UV-divergent, a renormalisation procedure has to be carried out. The divergences are first regularised using dimensional regularisation and then removed using suitable counterterms, which can be generated by `FeynArts`. We use the on-shell scheme to renormalize the wave-functions of the external partons and the masses of the squarks. The strong coupling constant is instead renormalized in the $\overline{\text{MS}}$ scheme with 5 active flavours, i.e. with decoupled squarks, gluinos and top quark, as discussed in Sec. 4.3.2. The Feynman diagrams corresponding to the counterterms,

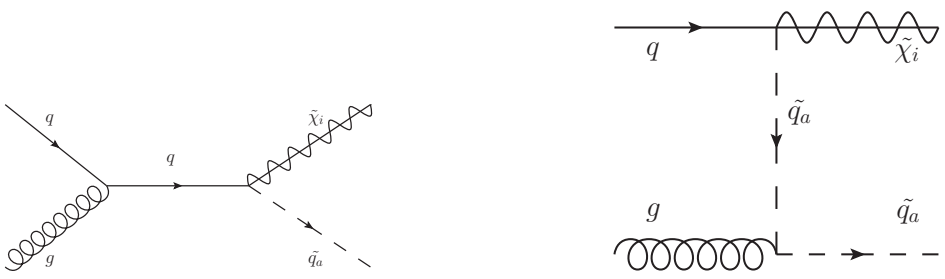

Figure 5.1: Tree-level Feynman diagrams for the weakino-squark production, through an s-channel (left) and t-channel(right) process.

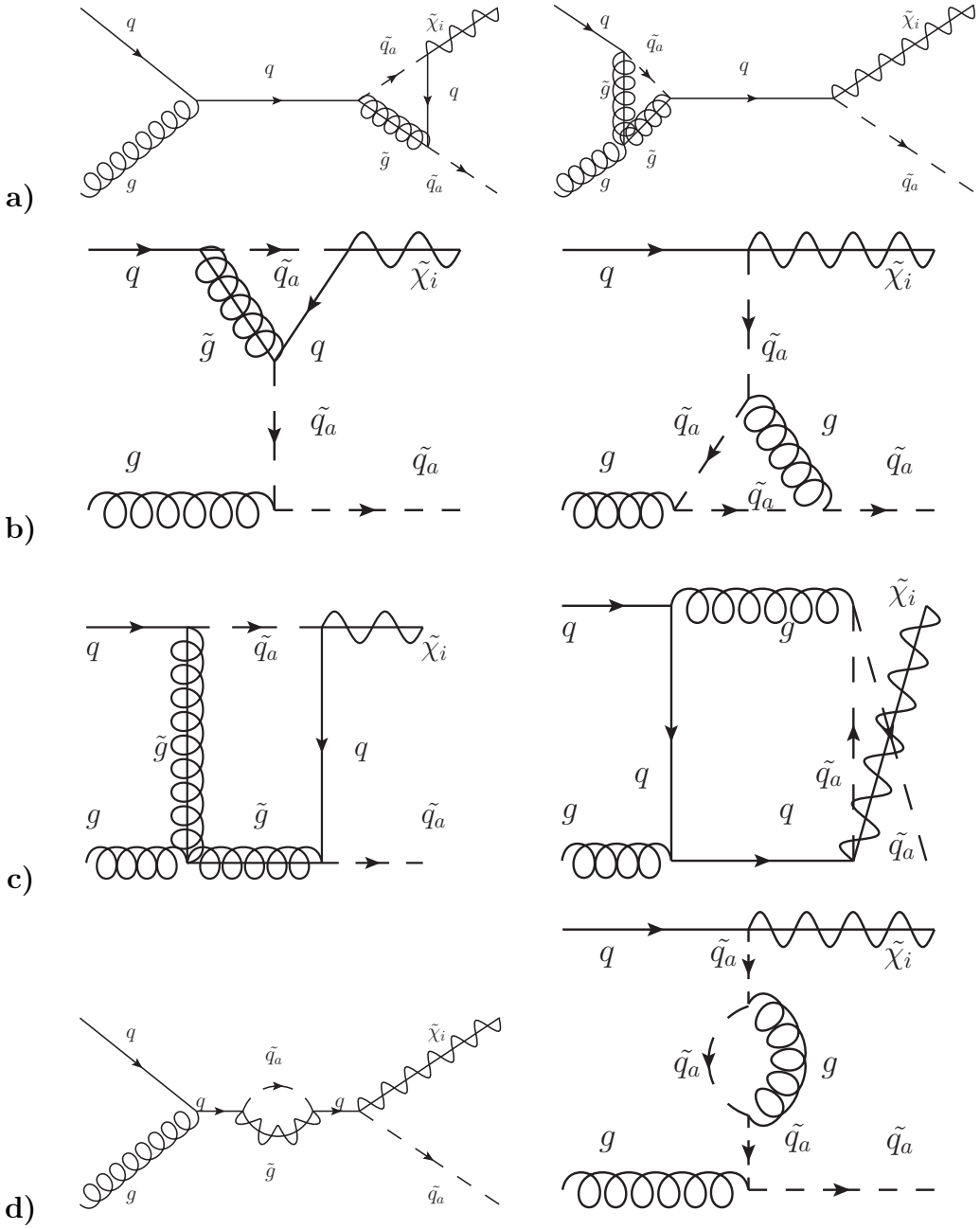

Figure 5.2: Representative Feynman diagrams for the virtual corrections, showing vertex corrections for the s-channel diagram (a), vertex corrections for the t-channel diagram(b), box corrections (c) and self-energy diagrams (d).

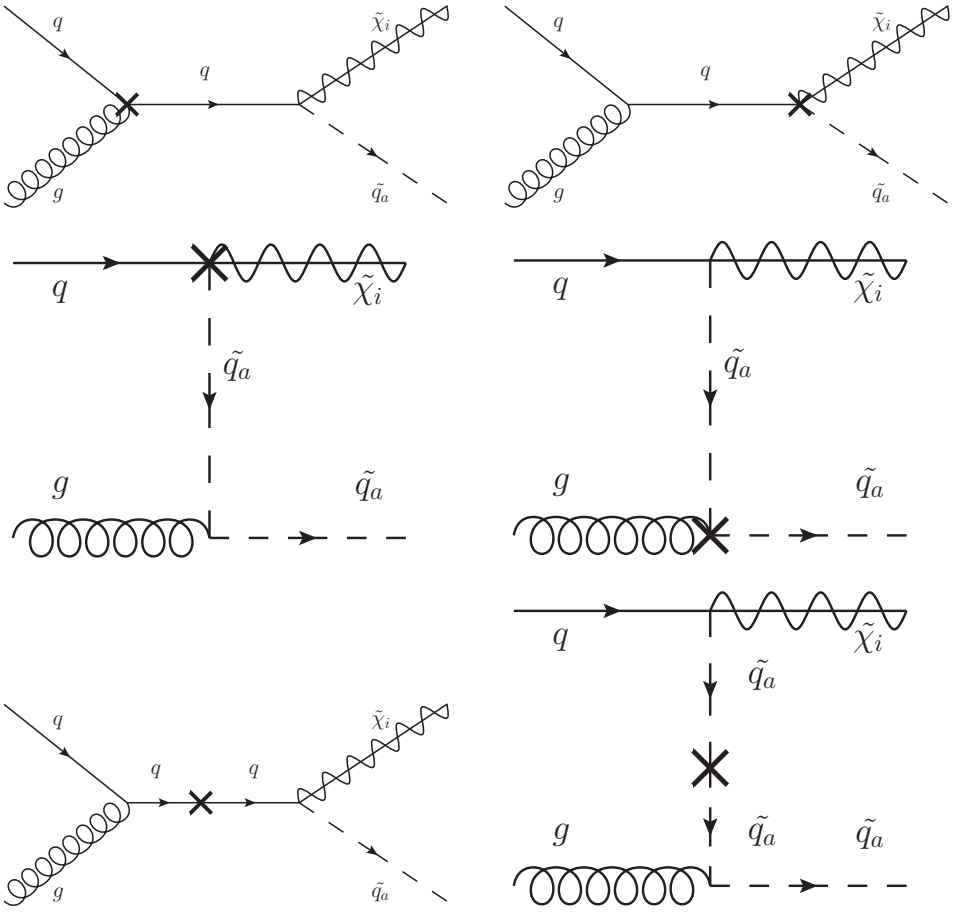

Figure 5.3: Feynman diagrams of vertex (upper and middle rows) and self-energy counterterms (lower row) for weakino-squark production.

both for the vertices and the self-energy diagrams, are shown in Fig. 5.3.

Performing the calculation in $D \neq 4$ dimensions, as required in the dimensional regularisation scheme, strongly breaks supersymmetry introducing a mismatch between the two degrees of freedom of the gaugino and the $(D-2)$ transverse ones of the gauge bosons. This has the practical consequence of spoiling the equality between the gauge couplings and the Yukawa couplings beyond LO, which is required by SUSY invariance. This equality has to be restored introducing finite counterterms [137–139]. In our case, the relevant Yukawa coupling is the weakino-quark-squark one, for which the counterterm reads:

$$\hat{g} = g\left(1 - \frac{\alpha_S}{6\pi}\right). \tag{5.1}$$

The virtual diagrams also present IR divergences, which correspond to divergences of opposite sign steming from the real corrections. As previously mentioned in Sec. 4.5, they are cancelled separately in the virtual corrections and in the reals using the FKS subtraction method.

5.3 Real corrections

The real emission contributions have been generated using the aforementioned tool based on `MadGraph 4`. Differently from the LO case, which includes only quark-gluon induced channels, the real corrections include $q\,q$ and $g\,g$ initial states, resulting in the

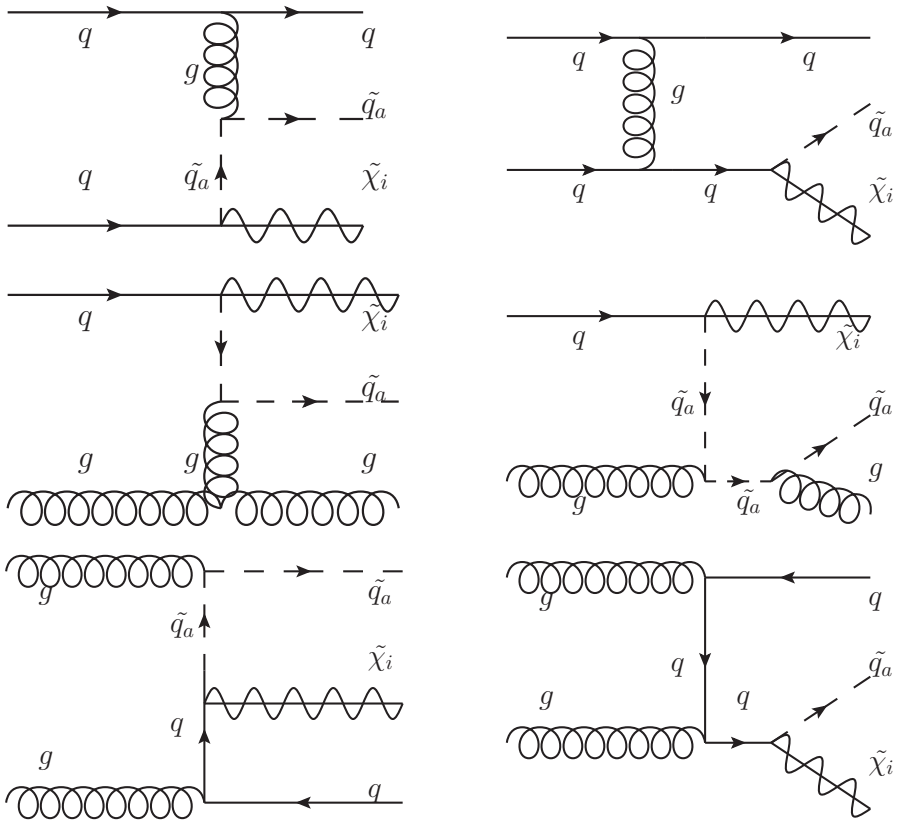

Figure 5.4: Representative Feynman diagrams for the real-emission processes in the $q\,q$ (upper row), $g\,q$ (central row) and $g\,g$ (lower row) channels. These diagrams do not include on-shell resonances.

following channels:

$$g\,g \to \tilde{\chi}_i^i\,\tilde{q}\,q,$$
$$g\,q \to \tilde{\chi}_i^i\,\tilde{q}\,g,$$
$$q\,q \to \tilde{\chi}_i^i\,\tilde{q}\,q.$$

Representative diagrams are shown in Fig. 5.4. Considering the various possibilities, the real corrections for each final state consists of 30 subchannels for the neutralino-squark final states and of 36 subchannels for the chargino-squark final states.

A significant technical complication is represented by the fact that in some of the real corrections diagrams, an intermediate particle, namely a squark or a gluino, can become on-shell. These resonances appear in both the $q\,q$ and the $g\,g$ channels. Representative diagrams are shown in Fig. 5.5. Squarks of any flavours can become on-shell, as long as they are more massive than the final-state weakino. The on-shell resonances of gluinos are kinematically available when the gluino is heavier than the final-state squark.

Apparently, these resonant contributions spoil the perturbative behaviour of our calculation, as they can easily be of the same order of magnitude as the LO cross section. However, these resonant contributions are not a genuine part of the real corrections to the process that we are considering. They should instead be seen as the on-shell production of a different final state followed by a decay into two different particle, e.g. in the case of an on-shell resonant squark, as a di-squark production process followed by the decay of one of the squarks into a weakino and a quark. These contributions are therefore already taken into account in the respective production processes and

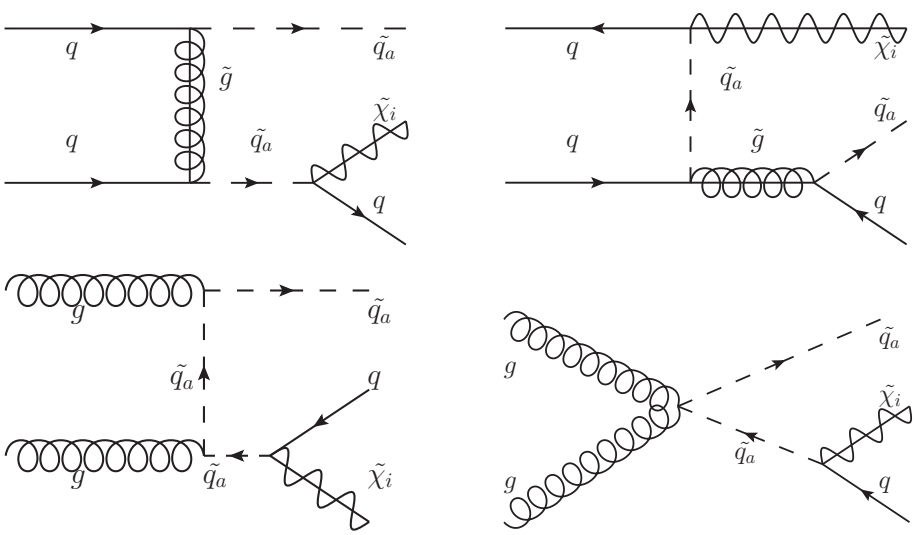

Figure 5.5: Representative Feynman diagrams for the real-emission processes that include on-shell resonances of gluinos (top-right diagram) and squarks (all remaining diagrams).

considering them as a part of our real corrections would lead to them being counted twice. They have therefore to be removed from our real-emission contributions to obtain a well-defined factorisation of production and decay processes, which will then be again perturbatively well-behaved.

On-shell resonances appear rarely in SM processes (e.g. in Wt production [140]), but are a relatively common feature of SUSY calculation. A similar subtraction procedure is necessary, for instance, in weakino-pair production [113,130] and in squark-pair production [128,129]. We will base the subtraction scheme of the on-shell resonances for our implementation on the schemes discussed in these references.

5.4 Subtraction of on-shell resonances

The real-emission contributions to a process containing on-shell resonances can be divided in non-resonant (labelled as nr) and resonant (labelled as res) part in the following way:

$$|\mathcal{M}|^2 = |\mathcal{M}_{nr}|^2 + 2\mathfrak{R}|\mathcal{M}^*_{nr}\mathcal{M}_{res}| + |\mathcal{M}_{res}|^2, \tag{5.2}$$

where also an interference term between the non resonant and resonant term appears. This separation is performed at the diagram level, meaning that only the diagrams that do not contain any resonances are included in the non-resonant matrix elements, $\mathcal{M}_{nr}$. The resonant matrix elements $\mathcal{M}_{res}$ include all the diagrams containing at least one possible on-shell resonance.

The simplest possible way to remove all on-shell contributions consists of simply removing the all the diagrams containing a potential resonance as well as the interference term, which reduces the real corrections to:

$$|\mathcal{M}^{\mathrm{DRI}}|^2 = |\mathcal{M}_{nr}|^2. \tag{5.3}$$

This subtraction method is called diagram removal type I (DRI).

A slightly more refined method consists of removing all the diagrams containing a potential resonance, but keeping contribution from the interference terms ,$2\mathfrak{R}|\mathcal{M}^*_{nr}\mathcal{M}_{res}|$. This can be considered preferable, since these interference terms are appearing exclusively in the context of these real corrections and are therefore not counted twice when

other production processes are considered. The real corrections are in this case:

$$|\mathcal{M}^{\mathrm{DRII}}|^2 = |\mathcal{M}_{nr}|^2 + 2\Re|\mathcal{M}^*_{nr}\mathcal{M}_{res}|. \tag{5.4}$$

This method is called diagram removal type II (DRII). In our POWHEG-BOX implementation of weakino-squark production, it is possible to remove on-shell resonances using this method.

These two methods are very simple but they have some serious drawbacks. Removing the entire amplitude of the diagrams containing resonances means that also off-shell contributions, which are a proper part of the real corrections, are removed. Moreover, removing an arbitrary number of diagrams violates, in general, gauge invariance.

Therefore, a more suitable choice would be to remove exclusively the on-shell contributions from the resonant diagrams, but to leave the off-shell parts intact. This method is usually called diagram subtraction (DSUB) and was first implemented in [115]. The DSUB method is the default option for the removal of on-shell resonances in our POWHEG-BOX implementation. The first step is the regularisation of the singularities present in the propagator of the on-shell particles, achieved by inserting a technical regulator Γ_{reg}:

$$\frac{1}{s_{ij} - m_{ij}^2} \to \frac{1}{s_{ij} - m_{ij}^2 + i\,\Gamma_{reg}\,m_{ij}}, \tag{5.5}$$

where m_{ij} is the mass of the potentially on-shell particle ij and $s_{ij} = \left(p_i + p_j\right)^2$, with i and j being the final state particles that are daughter particles of the ij particle. The regulator Γ_{reg} is not necessarily the physical width of the particle, but a technical parameter. The total cross section, after the removal of on-shell contributions, should not be dependent from Γ_{reg}, as the off-shell contributions are not. This also ensures that, while the DSUB method in general breaks gauge-invariance, this gauge-invariance breaking effects are numerically negligible. This is ensured by reaching the narrow-width approximation[2], in which the production and decay processes are factorised. Practically speaking, this means choosing a sufficiently small value for Γ_{reg}. Our findings regarding this value will be discussed in Sec. 5.5.

After the regularisation, the removal of the on-shell contributions is performed by subtracting, locally from each resonant diagram, a counterterm that reproduces the behaviour of the on-shell resonances. For a single on-shell resonance in a $2 \to 3$ process the general shape of this counterterm is:

$$|\mathcal{M}^{\mathrm{CT}}_{res}|^2 = \prod_{ij} \Theta\left(s - (m_{ij} + m_k^2)\right) \Theta(m_{ij} - m_i - m_j)\, BW |\mathcal{M}_{\mathrm{res}}|^2_{\mathrm{OS}}, \tag{5.6}$$

where again the particles originated by the potentially on-shell particle are labelled i and j, and the index k denotes the remaining particle, which is often referred to as the spectator particle. The first theta-function represents the condition that the centre-of-mass energy squared s is high enough to produce the intermediate particle ij and the spectator particle k on their mass shell. The second theta-function guarantees that the mass of the intermediate particle m_{ij} is larger than the sum of the masses of the two particles i, j, as otherwise an on-shell decay would not be possible. The remaining terms are the Breit-Wigner factor, BW, and the remapped resonant matrix element squared $|\mathcal{M}_{\mathrm{res}}|^2_{\mathrm{OS}}$, which is the resonant matrix element squared calculated with on-shell momenta and applying the substitution in Eq. (5.5) to the propagators of on-shell particles. Thus, both terms depend on the regulator Γ_{reg}..

[2] An overview over the narrow-width approximation is given in [141].

The Breit-Wigner factor BW is used to suppress the counterterm in correspondence of off-shell regions, to avoid the subtraction of off-shell contributions. It is defined as the ratio between the matrix element squared and the matrix element squared itself taken in the on-shell limit, i.e. $s_{ij} \to m_{ij}^2$ and is equal to:

$$BW = \frac{m_{ij}^2 \Gamma_{reg}^2}{(s_{ij}^2 - m_{ij}^2)^2 + m_{ij}^2 \Gamma_{reg}^2}. \tag{5.7}$$

In order for a BW factor to reproduce as closely as possible the behavior of the resonance, the regulator Γ_{reg} is usually chosen such that it is as small as possible without causing numerical instabilities in the integration. In the limit $\Gamma_{reg} \to 0$, the BW factor approaches a Dirac delta, leading to fewer off-shell contributions being included in the counterterm.

Finally, the counterterm contains the on-shell matrix element squared $|\mathcal{M}_{\text{res}}|^2_{\text{OS}}$, which has to be evaluated for on-shell kinematics, meaning that the momentum of the intermediate particle has to meet the condition $p_{ij}^2 = m_{ij}^2$, which is not guaranteed for arbitrary phase space points. To ensure this condition, a reshuffling of the momenta has to be performed, which ensures the on-shell condition and the conservation of four momentum. This procedure is similar to the one performed to produce transformed kinematics in order to remove IR singularities from real corrections in the Catani-Seymour algorithm [142]. The reshuffled momenta for the spectator particle k and for the on-shell particle ij can be written in terms of the original momenta as:

$$\tilde{p}_k = \frac{\lambda^{1/2}\left(s, m_{ij}^2, m_k^2\right)}{\lambda^{1/2}\left(s, s_{ij}, m_k^2\right)} \left(p_k^\mu - \frac{p_{12} \cdot p_k}{s} p_{12}^\mu\right) + \frac{s + m_k^2 - m_{ij}^2}{2s} p_{12}^\mu, \tag{5.8}$$

$$\tilde{p}_{ij} = p_{12}^\mu - \tilde{p}_k^\mu, \tag{5.9}$$

where p_{12} is the sum of the momenta of the incoming particles. The Källén λ function is defined as $\lambda(x, y, z) = x^2 + y^2 + z^2 - 2xy - 2xz - 2yz$. The two remaining reshuffled momenta, $\tilde{p}_i$ and $\tilde{p}_j$, are not defined unambigously. An arbitrary direction has to be chosen for one of the two particles; in our procedure we chose the keep the direction of the particle i fixed. The momenta p_i and p_j are boosted into the rest frame of the on-shell intermediate particle, where the solid angle of the particle i can be extracted. In this reference frame, the reshuffled momenta $\tilde{p}_i'$ and $\tilde{p}_j'$ are built using the on-shell condition and the fixed direction of the particle i. At this point, the momenta are boosted back along the momentum $\tilde{p}_i j$, yielding the reshuffled momenta $\tilde{p}_i$ and $\tilde{p}_j$.

Before integrating the counterterm over the phase space, however, another consideration is necessary: the matrix elements contained in the counterterm have been evaluated in a different phase space that meets the on-shell conditions, as we just discussed, which is different from the phase space in which all the other real matrix elements have been calculated, i.e. the general three-particle phase space $d\Phi_3$. Therefore, the integration has to be performed over a separate phase space or, alternatively, a corrective factor reflecting the phase-space transformation, also called Jacobian factor, can be introduced before integrating the real contributions and the counterterms over the same phase space. If $d\tilde{\Phi}_3$ is the on-shell phase space elements, it can be espressed in terms of the the regular three-particle phase space as:

$$d\tilde{\Phi}_3 = \mathcal{J}_3 d\Phi_3. \tag{5.10}$$

The Jacobian factor can be derived by imposing the on-shell condition to the integration

over the $d\Phi_3$ and reads:

$$\mathcal{J}_3 = \frac{s_{ij}\lambda^{1/2}(s, m_{ij}^2, m_k^2)\lambda^{1/2}(m_{ij}^2, m_i^2, m_j^2)}{m_{ij}^2\lambda^{1/2}(s, s_{ij}, m_k^2)\lambda^{1/2}(s_{ij}, m_i^2, m_j^2)}, \tag{5.11}$$

where the Källén λ function is defined as $\lambda(x, y, z) = x^2 + y^2 + z^2 - 2xy - 2xz - 2yz$.

Now that all the necessary ingredients for the subtraction of the on-shell resonances have been described, the cross section for the real contributions can be calculated as:

$$\sigma_{real} = \int d\Phi_3 \left[|\mathcal{M}_{nr}|^2 + 2\Re|\mathcal{M}_{nr}^*\mathcal{M}_{res}|\right] + \sigma_{OS}, \tag{5.12}$$

where σ_{OS} is:

$$\sigma_{OS} = \int d\Phi_3 \left[|\mathcal{M}_{res}|^2 - \mathcal{J}_3|\mathcal{M}_{res}^{\mathrm{CT}}|^2\right] \tag{5.13}$$

There are two possibilities to perform the integration necessary to calculate these cross section. The simpler way is to actually not perform the integration in Eq. (5.13) before summing it into Eq. (5.12), but to perform only one collective integration for the whole real cross section. We will refer to this method as DSUBI. The second possibility is to perform separately the integrations, i.e. summing the contributions from Eq. (5.13) into Eq. (5.12) after they have been integrated. We will refer to this method as DSUBII. Requiring two separate integrations, the DSUBII method is obviously more time-consuming. Moreover, it requires some modifications to the structure of the `POWHEG-BOX` to handle the separate integrations. These modifications are included in our implementation of this process.

Despite its complexity, the DSUBII method is the default option in our implementation, as for some scenarios, the DSUBI method was leading to numerical instabilities, as it will be discussed in the following section. Both methods are however available in our implementation.

5.5 OSR in weakino-squark production at NLO

We will now discuss the specific feature of the on-shell resonances present in the real-emission contributions to the weakino-squark production. As already mentioned, squarks of every flavour and gluinos can become resonant, leading to 11 independent channels for resonances. In principle, a different regulator could be used for every channel. In our implementation, a distintion is made only between the regulator for squark resonances $\Gamma_{\tilde{q}}$ and the one for gluino resonances $\Gamma_{\tilde{g}}$.

To check the stability of our on-shell subtraction method, we investigated the impact of the variation of the regulator on our results. We noticed that the DSUBI method was sufficient to give stable results when only gluino resonances were present but that when also squark resonances were possible, using the DSUBII method was necessary, because of the more complicated resonant structure. We therefore recommmend the use of the DSUBII method. We also observed that the total cross section does not depend from the value of the regulator, given that this value is chosen to be sufficiently small. For both the gluino and the squark resonances, the ratio between the regulator and the mass of the resonant particle should not be larger than 10^{-4}. Smaller values can be used, but they lead to larger numerical errors.

Our findings are shown in Fig. 5.6. We performed the calculation of the NLO cross section for $\tilde{\chi}_1^0\tilde{d}_L$ using an artificial SUSY spectrum in which the mass values

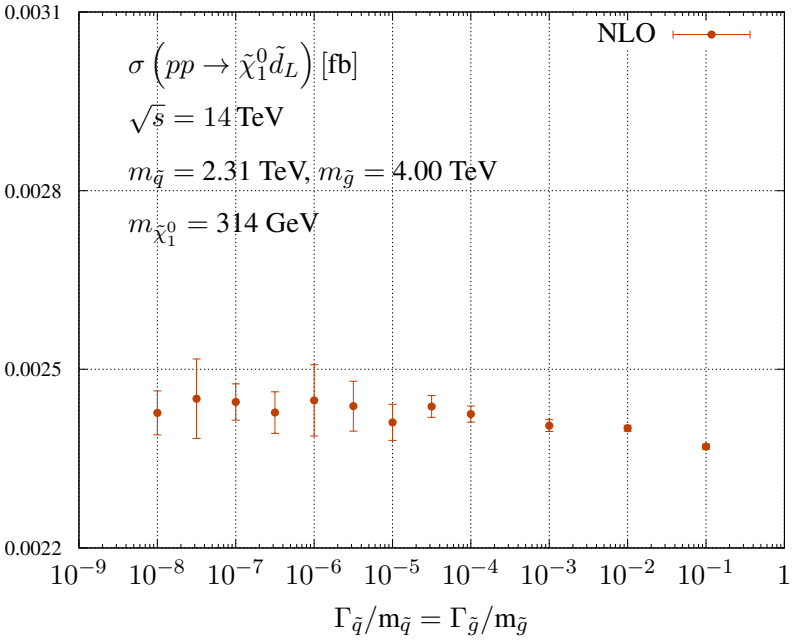

Figure 5.6: Dependence of the total cross section for the process $pp \to \tilde{d}_L \tilde{\chi}_1^0$ on the regulators $\Gamma_{\tilde{q}}$ and $\Gamma_{\tilde{g}}$. The values of the two regulators have been changed simultaneously to explore the range $10^{-8} \leq \frac{\Gamma_i}{m_i} \leq 10^{-4}$, where $i = \tilde{q}, \tilde{g}$.

lead to the simultaneous appearance of gluino and squark resonances. The mass of the neutralino has been set to 314 GeV, the mass of the gluino has been set to 4.00 TeV and the squarks have been assumed to be mass degenerate with a mass of 2.31 TeV. The value of the two regulators has been changed simultaneously to explore the range $10^{-8} \leq \frac{\Gamma_i}{m_i} \leq 10^{-1}$, where $i = \tilde{q}, \tilde{g}$. In the range $10^{-8} \leq \frac{\Gamma_i}{m_i} \leq 10^{-4}$, the cross section appears to be fundamentally independent of the regulator, thus proving that our on-shell subtraction scheme is well-defined and that gauge-violating effects are numerically negligible once the the narrow-width approximation for the intermediate on-shell states has been reached. For larger values of the regulator, the cross section is no longer constant.

5.6 Checks of our implementation

To verify the correctness of our calculation, we performed two cross-checks, confronting our results with indipendently obtained ones.

The first cross-check has been performed with a non-publicly available calculation based on the `Prospino` framework [143]. This calculation has been performed using mass-degenerate light-flavour squarks. It is worth mentioning that, in this calculation, the removal of on-shell resonances has been performed using a completely different approach, used and described in Refs. [115, 139, 144–147]. This method is based on a resonant and factorized parametrisation of the phase-space integration within the `Prospino` framework, considering the matrix elements of the production of the intermediate resonant squark/gluino and of the subsequent decay, including spin correlations and chiral states. We performed a detailed comparison between the the two calculations, involving several different SUSY parameter space points, both in the presence of on-shell resonances and in their absence. We checked separately all the individual parts contributing to the NLO cross sections. We found full agreement at the permille

pMSSM11 - Scenario a				
M_1	M_2	M_3	$m_{\tilde{q}}$	$m_{\tilde{q}_3}$
1.3 TeV	2.3 TeV	1.9 TeV	0.9 TeV	2.0 TeV
$m_{\tilde{l}}$	$m_{\tilde{\tau}}$	M_A	A	μ
1.9 TeV	1.3 TeV	3.0 TeV	-3.4 TeV	-0.95 TeV
$\tan\beta$	$m_{\tilde{\chi}_1^0}$	$m_{\tilde{\chi}_1^-}$	$m_{\tilde{d}_L}$	$m_{\tilde{g}}$
33	0.954 TeV	0.955 TeV	1.01 TeV	1.98 TeV
pMSSM11 - Scenario b				
M_1	M_2	M_3	$m_{\tilde{q}}$	$m_{\tilde{q}_3}$
0.25 TeV	0.25 TeV	-3.86 TeV	4.0 TeV	1.7 TeV
$m_{\tilde{l}}$	$m_{\tilde{\tau}}$	M_A	A	μ
0.35 TeV	0.46 TeV	4.0 TeV	2.8 TeV	1.33 TeV
$\tan\beta$	$m_{\tilde{\chi}_1^0}$	$m_{\tilde{\chi}_1^-}$	$m_{\tilde{u}_L}$	$m_{\tilde{g}}$
36	0.248 TeV	0.271 TeV	4.07 TeV	3.90 TeV

Table 5.1: Input parameters and relevant physical masses of the SUSY particles in the two scenarios used for our phenomenological studies.

level between the two approaches.

In the second cross-check, we reproduced the results presented in Ref. [148] and found, within the attainable accuracy, good agreement with them if adding squarks and antisquarks for the individual production processes.

5.7 Results

In order to demonstrate the capabilities of our code, we present numerical results for two selected scenarios: First, we consider the on-shell production of a neutralino and a squark for a realistic SUSY parameter point in the phenomenological MSSM model with eleven parameters, the pMSSM11, suggested in Ref. [49], which we call *scenario a*. This parameter point exhibits both squark and gluino on-shell resonances, thus showcasing the subtraction feature of our code. The input parameters and relevant physical masses are shown in the upper half of Tab. 5.1. Then, we consider the production of a chargino and a squark for another SUSY parameter point, extracted from the same reference, which takes into account constraints from a variety of experiments, including measurements of the anomalous magnetic moment of the muon [149, 150] (see also the latest experimental result reported in Ref. [151]), which we call *scenario b*. The input parameters and relevant physical masses are shown in the lower half of Tab. 5.1.

Our `POWHEG-BOX` code can be used to produce event files in the format of the Les Houches Accord (LHA) [127] for the on-shell production of a squark and a weakino. These event files can in turn be processed by a multi-purpose Monte-Carlo program like `PYTHIA` [21, 22] that provides a parton shower (PS) to obtain predictions at NLO+PS accuracy. `PYTHIA` furthermore provides the means for the simulation of tree-level decays of unstable SUSY particles. To illustrate that feature, we consider the squark+chargino production channel $pp \to \tilde{\chi}_1^- \tilde{u}_L$ for scenario b and simulate the decays of the squarks, $\tilde{u}_L \to u\tilde{\chi}_1^0$, and the charginos, $\tilde{\chi}_1^- \to e^-\bar{\nu}_e\tilde{\chi}_1^0$ with `PYTHIA 8` [22], thus providing predictions for $pp \to e^-\bar{\nu}_e\tilde{\chi}_1^0\, u\tilde{\chi}_1^0$ in the narrow-width approximation for the squark and chargino decays. We note that QCD corrections do not affect the purely weak chargino decay. QCD corrections in principle relevant for the squark decay are not

	LO	NLO	K		LO	NLO	K
$\tilde{\chi}_1^0\tilde{d}_L$	2.11	3.24	1.54	$\tilde{\chi}_1^0\tilde{d}_R$	0.0348	0.145	4.16
$\tilde{\chi}_1^0\tilde{u}_L$	6.76	9.47	1.42	$\tilde{\chi}_1^0\tilde{u}_R$	0.342	0.595	1.74
$\chi_1^+\tilde{d}_L$	3.80	6.03	1.59	$\chi_1^-\tilde{u}_L$	9.86	14.2	1.44

Table 5.2: Cross sections at LO and NLO accuracy and K factors for different final states in scenario a. The quoted numbers include the sum of channels for weakino production in association with a squark and an anti-squark of the given flavour. All cross-section numbers are given in units of [ab]. The numerical uncertainties do not affect the digits reported.

taken into account. When labeling the perturbative accuracy of our results, we will only refer to the production process, implicitly assuming that no QCD corrections are provided for the squark decays.

Throughout our analysis, the renormalisation and factorisation scales, $\mu_{\rm R}$ and $\mu_{\rm F}$ are set to

$$\mu_{\rm R} = \xi_{\rm R}\mu_0\,, \mu_{\rm F} = \xi_{\rm F}\mu_0\,, \tag{5.14}$$

with

$$\mu_0 = (m_{\tilde{d}_L} + m_{\chi_1^0})/2\,. \tag{5.15}$$

The scale variation parameters $\xi_{\rm R}, \xi_{\rm F}$ are used to vary the scales around their central value. If not specified otherwise, they are set to $\xi_{\rm R} = \xi_{\rm F} = 1$. For the parton distribution functions (PDFs) of the protons we use the CT14LO and CT14NLO set [152] as provided by the LHAPDF library [153] and the associated strong coupling with $\alpha_s(m_Z) = 0.118$ for five active flavours. We used as electroweak input parameters the Z boson mass, $m_Z = 91.188$ GeV, the Fermi constant, $G_F = 1.166379 \cdot 10^{-5}$ GeV^{-2} and the W boson mass, $m_W = 80.393$ GeV, while the electromagnetic coupling α is a derived quantity. All our results correspond to proton-proton collisions at a center-of-mass energy of 14 TeV. Unless stated otherwise, our results do not include contributions from anti-squark production channels.

In Tab. 5.2, we report cross sections and K factors, defined as the ratio of NLO to LO cross sections,

$$K = \frac{\sigma_{NLO}}{\sigma_{LO}}\,, \tag{5.16}$$

for various final states in scenario a. We quote results for the production of squarks and anti-squarks of the first generation in association with either the lightest neutralino $\tilde{\chi}_1^0$ or chargino $\tilde{\chi}_1^\pm$. From our results the relevance of the NLO corrections is apparent, with most of the production rates increased of around 50%. An exceptionally large K-factor of 4.16 is observed for the $\tilde{\chi}_1^0\tilde{d}_R$ channel, due to the suppression of the LO matrix elements and the large numbers of quark- and antiquark-induced channels of the real corrections.

In Fig. 5.7 we present the dependence of the cross section for the process $pp \to \tilde{d}_L\tilde{\chi}_1^0$ on the renormalisation and factorisation scales for scenario a. The cross section depends on both of these scales already at LO. We varied $\mu_{\rm R}$ and $\mu_{\rm F}$ around the central value $\mu_0 = (m_{\tilde{d}_L} + m_{\chi_1^0})/2$ in the range $0.5\mu_0$ to $2\mu_0$. At LO, we observe a more pronounced dependence on the factorisation scale, with the combined variation of factorisation and renormalisation scale in the above mentioned range leading to a variation of the cross section of approximately 38%. The overall variation of the NLO cross section in the range $0.5\mu_0$ to $2\mu_0$ is reduced to approximately 19%. At NLO, the dependence on $\xi_{\rm F}$ is significantly reduced, while the variation due to $\xi_{\rm R}$ is only marginally reduced

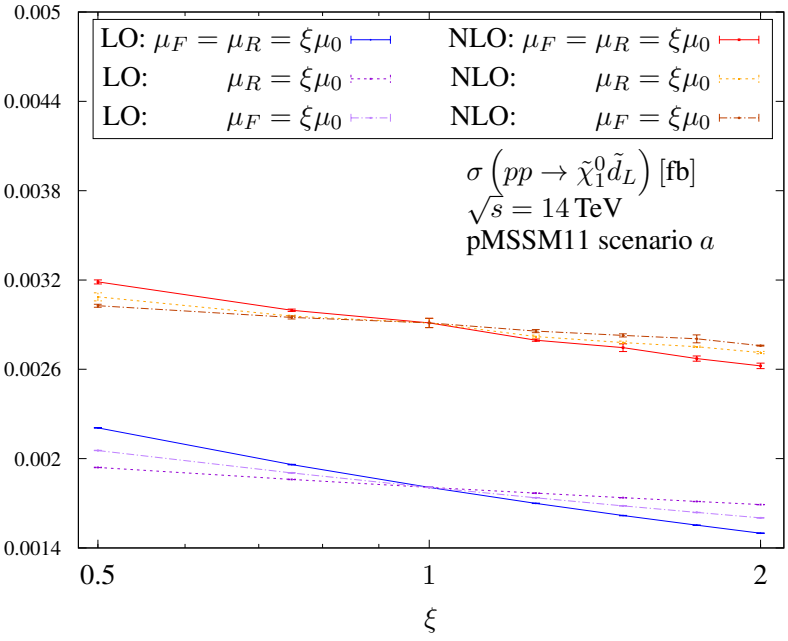

Figure 5.7: Dependence of the total cross section for the process $pp \to \tilde{d}_L \tilde{\chi}_1^0$ on the renormalisation (μ_R) and factorisation(μ_F) scales. Three curves are shown for the LO and NLO cases, respectively. The solid lines correspond to $\mu_\mathrm{R} = \mu_\mathrm{F} = \xi\mu_0$, the dotted lines to $\mu_\mathrm{R} = \xi\mu_0$ with $\mu_\mathrm{F} = \mu_0$ and the dash-dotted lines to $\mu_\mathrm{F} = \xi\mu_0$ with $\mu_\mathrm{R} = \mu_0$ for scenario a.

compared to the LO which can be traced back, to a large amount, to the sizable number of quark- and antiquark-induced channels of the real corrections.

To verify the last statement, we performed a study on the dependence of the cross section on the renormalisation and factorisation scale for scenario a. This time, we considered the process $pp \to \tilde{d}_R \tilde{\chi}_1^0$, which has, as noted in Table 5.2, a K-factor exceeding four. We studied the dependence of the NLO cross section on said scales but without considering the real-emission contributions due to quark- and anti-quark induced channels. As expected, we observed a significant decrease of the K-factor, which is in this case approximately 1.6, and a diminuition of the scale dependence in the range $0.5\mu_0$ to $2\mu_0$, which in this case is around 14%.

Scenario a : $\tilde{\chi}_1^0 \tilde{d}_L$ production

For our phenomenological study of the representative squark+neutralino production channel $pp \to \tilde{\chi}_1^0 \tilde{d}_L$ in scenario a we assume the neutralino gives rise to a signature with a large amount of missing transverse momentum. We do not consider squark decays for this study, as it is mainly intended to demonstrate the perturbative stability of our results and the applicability of our code to searches for DM and other types of new physics. In this way, we do not spoil the NLO-QCD accuracy of our results with the inclusion of tree-level decays.

In this scenario with stable squarks, jets can only arise from real-emission contributions or parton-shower effects. We reconstruct jets from partons using the anti-k_T jet algorithm [154] with an R parameter of 0.4. While we do study the properties of such jets to assess the impact of the parton-shower matching on the NLO-QCD results, we do not require the presence of any jets in the event selection, but impose cuts only on the missing transverse momentum of the produced system.

The missing transverse momentum of an event, $\vec{p}_T^{\,\mathrm{miss}}$, is reconstructed from the

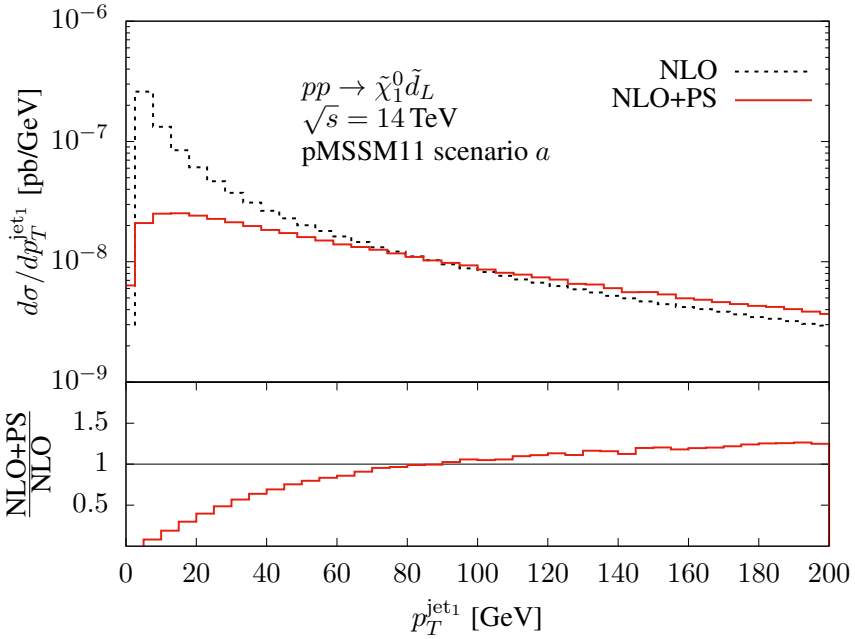

Figure 5.8: Transverse-momentum distribution of the hardest jet in the process $pp \to \tilde{d}_L \tilde{\chi}_1^0$ at NLO (black dotted curve) and NLO+PS (red solid curve) before any cuts are applied. The lower panel shows the ratios of the NLO+PS to the NLO results.

negative of the vectorial sum of the transverse momenta of all objects assumed to be visible to the detector (i.e. jets with a transverse momentum larger than 20 GeV in the pseudorapidity range $|\eta^{\text{jet}}| < 4.9$ and squarks). We discussed the importance of this observable for DM searches in Sec. 3.5.3. The absolute value of $\vec{p}_T^{\,\text{miss}}$ is sometimes referred to as "missing transverse energy", $E_T^{\text{miss}} = |\vec{p}_T^{\,\text{miss}}|$.

In Fig. 5.8 we show the transverse-momentum distribution of the hardest jet, before any cuts are imposed. In our setup, with a stable squark, such a jet can only result from the real-emission contributions or from the parton shower. This distribution is thus particularly sensitive to the NLO+PS matching. Indeed, the figure shows the typical Sudakov behavior expected for this distribution: Towards low values of p_T^{jet}, the fixed-order result becomes very large. The Sudakov factor supplied by the NLO+PS matching procedure dampens that increase. At higher transverse momenta the NLO+PS results are slightly larger than the fixed-order NLO results. Since our analysis is fully inclusive with respect to jets, distributions related to the directly produced squark and neutralino do not exhibit strong sensitivity to this Sudakov damping.

Figure 5.9 (left) illustrates the azimuthal-angular separation of the squark from the neutralino, $\Delta\phi(\tilde{\chi}_1^0, \tilde{d}_L)$ at NLO and NLO+PS accuracy before any cuts are imposed. The $\Delta\phi(\tilde{\chi}_1^0, \tilde{d}_L)$ distribution shows that squark and neutralino tend to be produced with large angular separation. The shape of the distribution is not significantly altered by parton-shower effects, but an almost flat increase of approximately 50% is observed for the NLO+PS distribution with the exception of the region in which $\Delta\phi(\tilde{\chi}_1^0, \tilde{d}_L)$ approaches π. The back-to-back production of the neutralino and the squark is then slightly favoured in the purely NLO case.

The missing transverse-momentum distribution is shown in Fig. 5.9 (right). In the bulk the NLO and NLO+PS results are very similar. This is not surprising, as the main source of missing transverse-momentum is the neutralino, which is not affected by the parton-shower effects. The only other source of $|\vec{p}_T^{\,\text{miss}}|$ are soft jets, which become

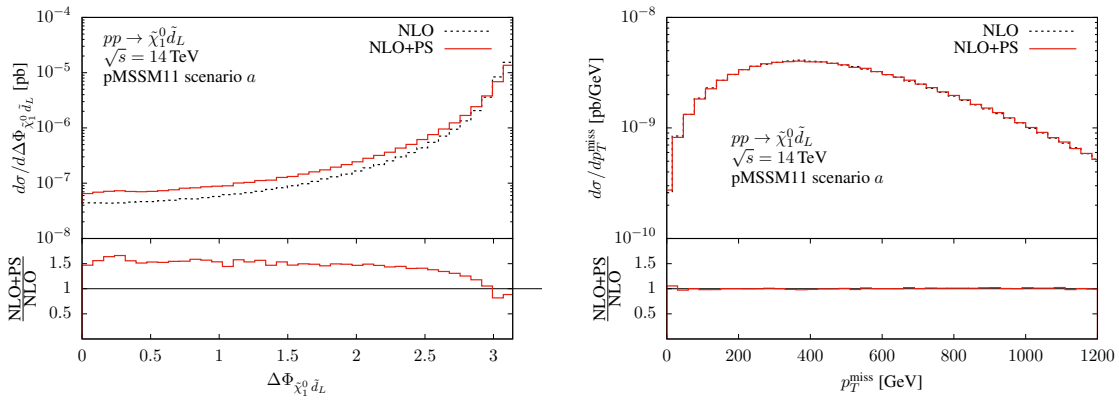

Figure 5.9: Angular separation of the squark and the neutralino (left) and missing transverse energy (right) in the process $pp \to \tilde{d}_L \tilde{\chi}_1^0$ at NLO (black dotted curves) and NLO+PS (red solid curves) before any cuts are applied. The lower panels show the ratios of the respective NLO+PS to the NLO results.

important only towards very large values of $|\vec{p}_T^{\,\text{miss}}|$. In this region, the fixed-order NLO result is indeed slightly larger than the corresponding NLO+PS result, which is related to the behavior of the jet at low p_T^{jet} discussed above. Using a cut on the missing transverse energy thus can be considered to be a perturbatively safe choice.

In the following, in order to consider an event in our analysis, we require it to be characterized by a large amount of missing transverse energy,

$$|\vec{p}_T^{\,\text{miss}}| > 250 \text{ GeV}\,. \tag{5.17}$$

At NLO, this is effectively equivalent to a cut on the transverse momentum of the neutralino, since the only other potential source of missing momentum is the jet stemming from the real-emission corrections, which however only escapes the detector if it is very soft or outside of the pseudorapidity range $|\eta^{\text{jet}}| < 4.9$. Including PS shower, other source of soft radiation emerge. In Fig. 5.10, we show the transverse-momentum distribution of the neutralino after the cut of Eq. (5.17) has been imposed. As is to be expected, the NLO and NLO+PS distributions are very different for low values of $p_T^{\tilde{\chi}_1^0}$, where the NLO distribution assumes very small values, but are then very similar for $p_T^{\tilde{\chi}_1^0} > 250$ GeV.

In Fig. 5.11 (left) we show the transverse-momentum distribution of the squark after the cut of Eq. (5.17) has been imposed. We discussed the effects of this cut on the transverse momentum of the neutralino. They transpose in a clear manner to this observable: The production of squarks with transverse momentum lower than 250 GeV is also suppressed. This is due to the fact the overall transverse momentum of the final state has to be equal to zero: The transverse momentum of the squark has to be equal to the sum of the ones of the neutralino and of the jets. Since the neutralino is, especially in the fixed order case, almost not produced with low transverse momentum because of the cut of Eq. (5.17), when the squark has a low transverse momentum only soft radiation can compensate the transverse momentum of the squark. Therefore, differences between the NLO and the NLO+PS predictions occur only in the region of low transverse momenta, where soft-gluon effects of the Sudakov factor dominate the NLO+PS results.

In Fig. 5.11 (right) we show instead the invariant mass distribution of the squark-neutralino system, which instead appears to be almost uneffected by the parton-shower effects.

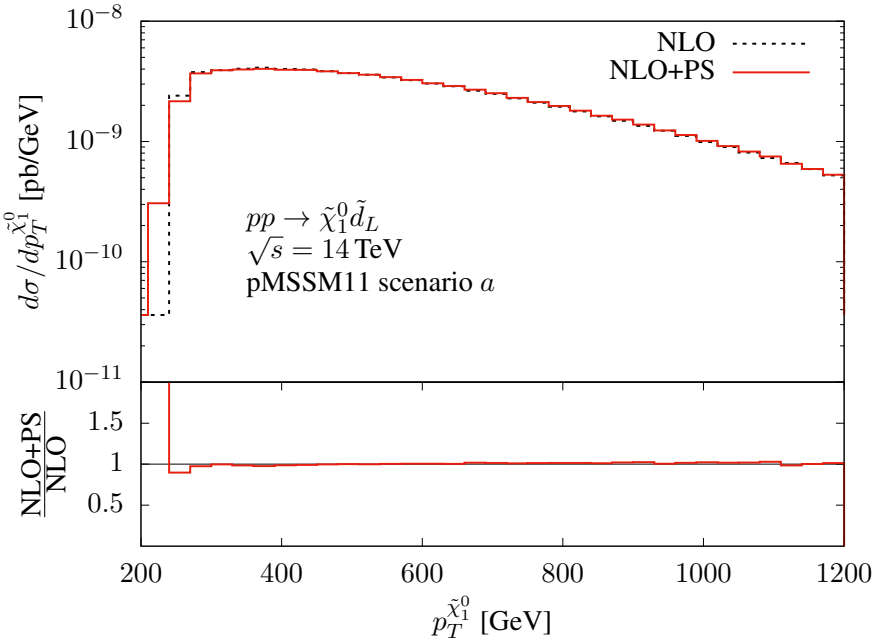

Figure 5.10: Transverse-momentum distribution of the neutralino in the process $pp \to \tilde{d}_L \tilde{\chi}_1^0$ at NLO (black dotted curve) and NLO+PS (red solid curve) after the cut of Eq. (5.17) has been applied. The lower panel shows the ratios of the NLO+PS to the NLO results.

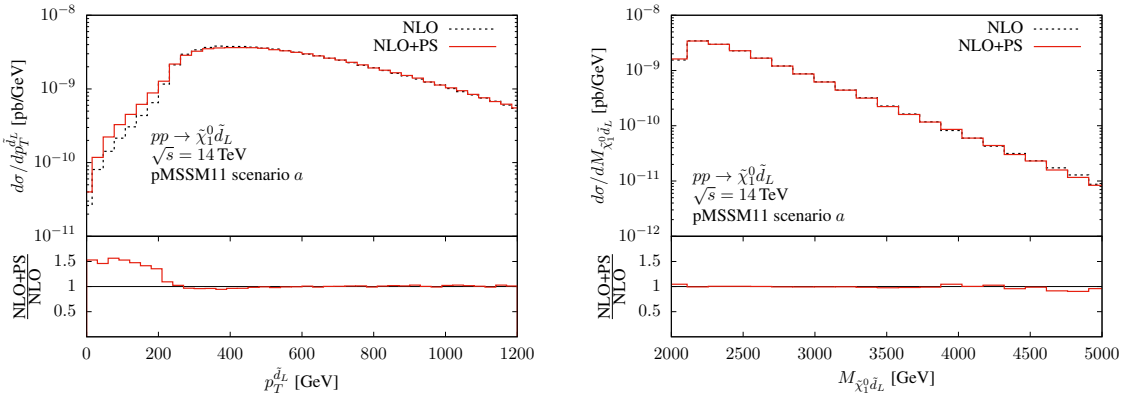

Figure 5.11: Transverse momentum of the squark (left) and invariant mass of the squark-neutralino system (right) in the process $pp \to \tilde{d}_L \tilde{\chi}_1^0$ at NLO (black dotted curves) and NLO+PS (red solid curves), after the cut of Eq. (5.17) has been applied. The lower panels show the ratios of the respective NLO+PS to the NLO results.

Scenario b : $\tilde{\chi}_1^- \tilde{u}_L$ production followed by $\tilde{u}_L \to u\tilde{\chi}_1^0$ and $\tilde{\chi}_1^- \to e^- \bar{\nu}_e \tilde{\chi}_1^0$

Most SUSY particles decay into lighter particles, including other SUSY particles and the LSP $\tilde{\chi}_1^0$. The latter is stable because of R-parity conservation, as we discussed Sec. 2.4.3 and therefore represent the bottom of these decay chains. To obtain more realistic simulations, these decays have to be taken into account.

Then, let us now consider the squark+chargino production channel $pp \to \tilde{\chi}_1^- \tilde{u}_L$ at NLO+PS accuracy, combined with tree-level decays of the squark, $\tilde{u}_L \to u\tilde{\chi}_1^0$, and the chargino, $\tilde{\chi}_1^- \to e^- \bar{\nu}_e \tilde{\chi}_1^0$, as provided by `PYTHIA 8`.

For the considered parameter point, which we called scenario b, the quark resulting from the squark decay gives rise to a very hard jet, shown in Fig. 5.12 (left). This is

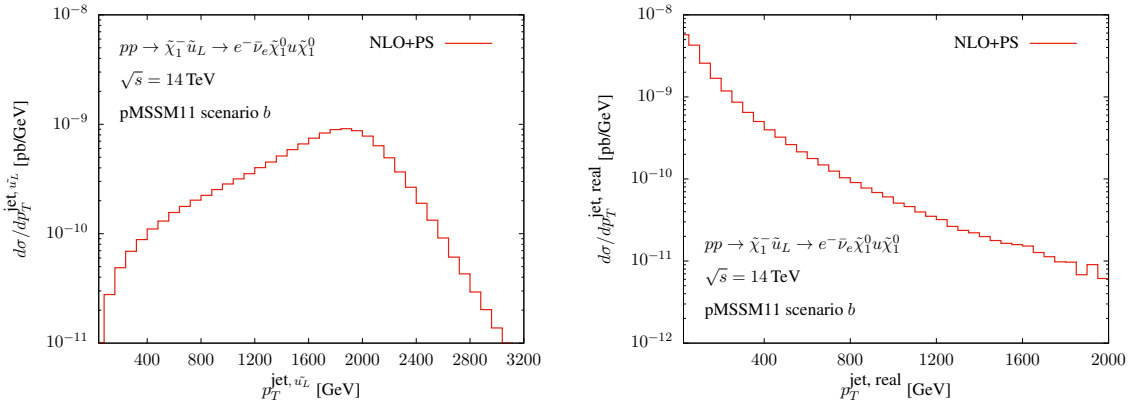

Figure 5.12: Transverse-momentum distribution of the jet stemming from the squark decay (left) and of the real-emission parton (right) in the process $pp \to \tilde{\chi}_1^- \tilde{u}_L \to e^- \bar{\nu}_e \tilde{\chi}_1^0 \, u \tilde{\chi}_1^0$ at NLO+PS accuracy before any cuts are applied.

due to the fact that, as shown in Tab. 5.1, the squark mass is a lot larger than the $\tilde{\chi}_1^0$ mass. In parameter points for which these masses are closer, such as scenario a, most of the momentum of the mother squark is allocated to the neutralino and the resulting jet is then much softer.

Further jets can be generated by real-emission corrections and the parton-shower. As demonstrated by Fig. 5.12 (right), such jets exhibit an entirely different shape and are produced with less transverse momentum, with an increase of the production of soft radiation.

In addition to the jet, the squark decay gives rise to a very hard neutralino. This means that there are several sources to the missing momentum of the final-state system, which include the neutralino and the neutrino stemming from the chargino decay and jets that are too soft to be identified. The total missing transverse energy of the $e^- \bar{\nu}_e \tilde{\chi}_1^0 \, u \tilde{\chi}_1^0$ final state is depicted in Fig. 5.13.

From this distribution it is clear that we can afford to impose a hard cut on E_T^{miss} to suppress background processes with typically much smaller amounts of missing transverse momentum, without significantly reducing the signal cross section. In the following we therefore impose a cut of

$$E_T^{\text{miss}} \geq 250 \text{ GeV} \,, \tag{5.18}$$

which reduces the cross section for $e^- \bar{\nu}_e \tilde{\chi}_1^0 \, u \tilde{\chi}_1^0$ production by less than one percent.

The momentum balance of the chargino-decay system is quite uneven: The heavy neutralino acquires a large amount of transverse momentum, peaked at about 450 GeV, while the lepton exhibits a much softer distribution, see Fig. 5.14. This is again a consequence of the mass pattern of the mother and decay particles. The difference between the masses of the chargino and of the neutralino is indeed only ≈ 20 GeV.

Even softer leptons are expected in SUSY scenarios where the masses of the chargino and its decay neutralino are yet closer than for the considered pMSSM11 point, such as for example scenario a. This feature has to be taken into account in searches aiming to use the lepton to tag a particular signal.

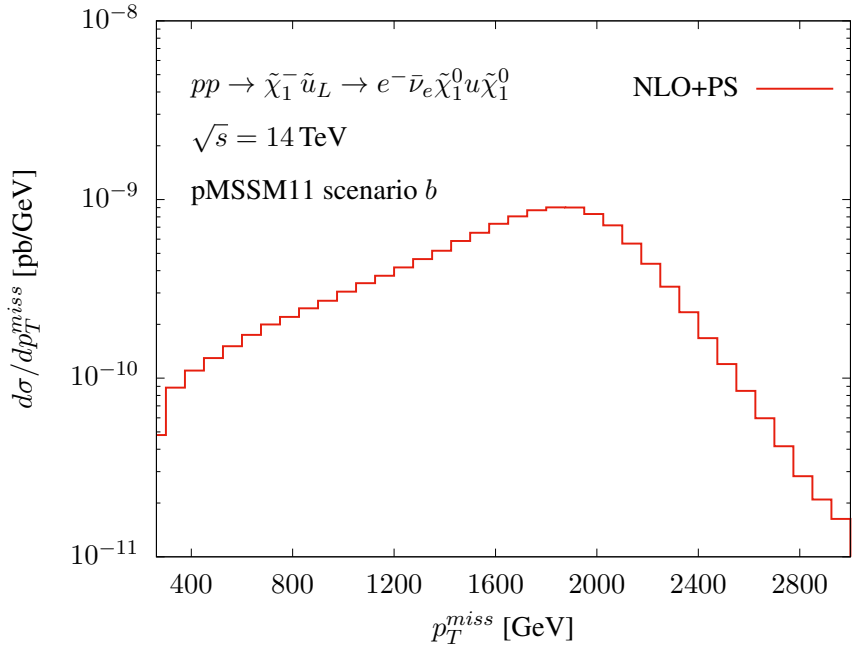

Figure 5.13: Missing transverse energy of the final-state system in the process $pp \to \tilde{\chi}_1^- \tilde{u}_L \to e^- \bar{\nu}_e \tilde{\chi}_1^0 \, u \tilde{\chi}_1^0$ at NLO+PS accuracy before any cuts are applied.

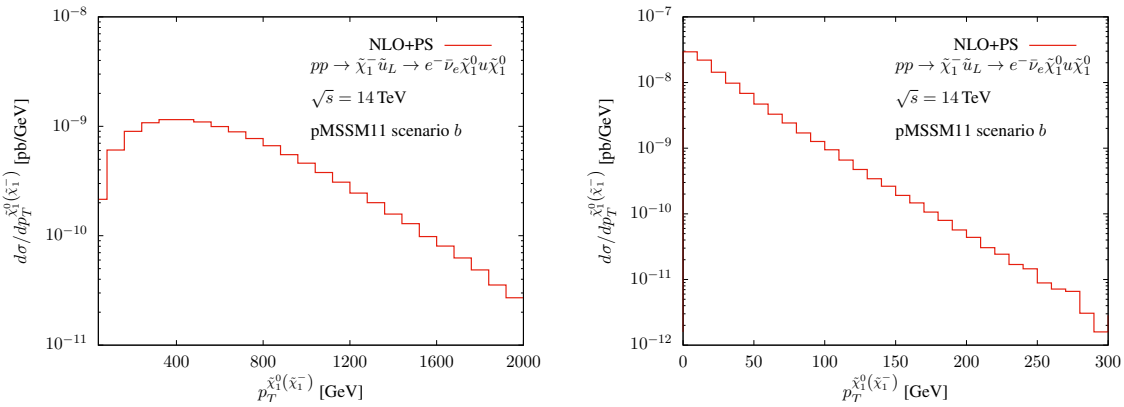

Figure 5.14: Transverse momentum distribution of the neutralino (left) and the electron (right) stemming from the chargino decay in the process $pp \to \tilde{\chi}_1^- \tilde{u}_L \to e^- \bar{\nu}_e \tilde{\chi}_1^0 \, u \tilde{\chi}_1^0$ at NLO+PS accuracy, after the cut of Eq. (5.18) has been applied.

Chapter 6

Dark matter production in the MSSM and in simplified models

In this chapter we will discuss the results published in [26]. In Chap. 3, we discussed at length the DM issue and we emphasised its relevance in modern physics. We introduced several DM candidates and discussed the framework of simplified models. We now study the phenomenology of two of these simplified models, namely the s-channel simplified model (Sec. 3.4.1) and the t-channel simplified model (Sec. 3.4.2).

Our aim is to establish the similarity of the phenomenology of DM-pair production in these simplified models with the phenomenology of the pair production of the DM candidate of the MSSM, the lightest neutralino $\tilde{\chi}_1^0$. The choice of the MSSM as reference UV-complete theory is due to the similarity of the production processes in the two frameworks.

Following our publication [26], we will start with the an expended discussion of the DM-pair production in the simplified models, including NLO QCD corrections which require the subtraction of on-shell resonances. We will then discuss the setup of our comparison between the simplified models and the MSSM and the results of our study.

6.1 Leading order production processes

In Sec. 2.4.3, we highlighted the characteristics of the lightest neutralino $\tilde{\chi}_1^0$, focusing on its composite nature and on its role as DM candidate, as it is in many scenarios the LSP and therefore, considering R-parity, a stable, massive and weakly interacting particle.

The LO production processes for $\tilde{\chi}_1^0$ pair-production in framework of the LHC are represented in Fig. 6.1. These diagrams clearly resemble the ones shown in Fig. 3.6, for the LO production processes of DM pair-production in an s-channel simplified model

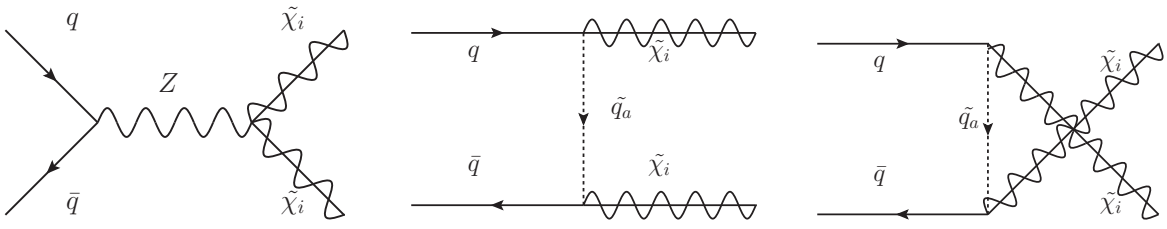

Figure 6.1: The LO production processes for a neutralino pair at the LHC. The u-channel diagram (right) is present because the neutralino is a Majorana fermion.

and in a t-channel simplified model motivating a detailed comparison of the respective phenomenologies. From the experimental point of view, the two approaches will lead to the same class of signature in the final state: large missing transverse momentum, due to the neutralino or DM pair, which is escaping detectors, recoiling against one or multiple hard jets. There are, however, a few clear differences. Each simplified model only contains a subset of diagrams similar to the ones in Fig. 6.1; moreover, we generally assume the DM particle in the simplified models to be a Dirac fermion, in contrast with the neutralino, which is a Majorana fermion. We will, for this reason, also consider the case of a Majorana fermion in the t-channel model, where we expect observable differences in the resulting phenomenologies due to the appearance of an additional diagram. In the s-channel model, instead, we have checked that this choice of fermion type does not have phenomenologically relevant consequences.

6.2 Dark matter pair production in simplified models at NLO

In order to perform an accurate phenomenological analysis and comparison between the two approaches, we will require NLO-QCD accuracy for the total pair production cross section. This is necessary because only the real corrections include an extra parton, which will give rise to a hard jet in the final state. As explained in Sec. 3.5.3, the DM particles will escape the detectors without leaving a directly observable signature. Therefore, to establish if they have been produced in a collision, it is necessary to observe visible particles recoiling against them and, consequently, a non-vanishing amount of transverse momentum in the final state. However, it should be noted that the hardest jet, being only accounted for by the real-emission corrections, is only described with LO accuracy.

For neutralino pair production, we make use of an existing `POWHEG-BOX` implementation for electroweakino pair production [130], which is publicly available from the online repository [155]. For the simplified models, we choose to create our own implementations, also based on the `POWHEG-BOX`, one for each model in consideration.

Before considering the specific characteristics of the NLO corrections, we compute the widths of the mediators in the two models, to be sure that, after our choice of parameters, we will be in a regime where the mediators can be treated perturbatively using the narrow-width approximation [84], meaning that the ratios between the width and the mass of the mediator are much smaller than one. We can compute the expressions for these ratios, that are simplified by some assumptions which we will make in order to keep the number of free parameter as small as possible, aiming to build models that are as simple as possible. These assumptions are: for the s-channel model, whose parameters were defined in Eq. (3.24) we will choose $g^V_{\chi/q} = g^A_{\chi/q} \equiv \tilde{g}$, and for the t-channel model, whose parameters were defined in Eq. (3.25), we will choose $\lambda_{Q_L} = \lambda_{u_R} = \lambda_{d_R} \equiv \tilde{\lambda}$ and we will additionally assume that the mediators of all flavours are degenerate in their mass $M_{\tilde{Q}}$. Therefore, for each model we have two free parameters, the mass of the mediator and a single coupling constant, in addition to the mass of the DM particle.

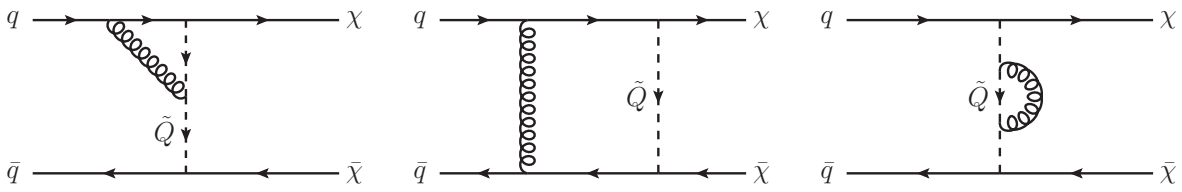

Figure 6.2: Selection ofFeynman diagrams of the virtual corrections to the t-channel model: a vertex correction (left), a box diagram (centre) and a self-energy diagram(right).

For the width of the mediator of s-channel model we then find:

$$\frac{\Gamma_V}{M_V} = \frac{\tilde{g}^2}{6\pi}\Bigg\{15 + \Theta(M_V - 2m_t)3\sqrt{1-\frac{4m_t^2}{M_V^2}}\left(1-\frac{m_t^2}{M_V^2}\right) + \Theta(M_V - 2m_\chi)\sqrt{1-\frac{4m_\chi^2}{M_V^2}}\left(1-\frac{m_\chi^2}{M_V^2}\right)\Bigg\}, \tag{6.1}$$

where we assumed five massless quark flavours. m_t is the mass of the top quark, equal to 173.0 GeV [156]. $\Theta(x)$ is the Heaviside step function with $\Theta(x) = 1$ for $x \geq 0$ and $\Theta(x)$ for $x < 0$. M_V is the mass of the vector mediator and m_χ the mass of the DM particle.

For the width of the mediator of the t-channel model we have:

$$\frac{\Gamma_{\tilde{Q}}}{M_{\tilde{Q}}} = \frac{\tilde{\lambda}^2}{16\pi}\left(1-\frac{m_\chi^2}{M_{\tilde{Q}}^2}\right)^2. \tag{6.2}$$

We will check that the ratios $\frac{\Gamma_V}{M_V}$ and $\frac{\Gamma_{\tilde{Q}}}{M_{\tilde{Q}}}$ are significantly smaller than one when we fix the parameters for our phenomenological studies.

The NLO corrections within the s-channel model are quite simple, since the only coloured particles present in the LO diagrams are the initial-state partons. The relevant diagrams were already shown in Fig. 4.1; additional real emission diagrams contribute, since gluon-induced channels are also present. These corrections are very similar to the Drell-Yan case and have been calculated before, for example in [157], but we decided to use our own implementation in order to have full control and flexibility.

The NLO corrections within the t-channel model are slightly more involved. The presence of a coloured mediator gives rise to additional virtual diagrams, such as box and self-energy diagrams. Representative Feynman diagrams are shown in Fig. 6.2. In the real emission corrections, on-shell resonances can arise. We gave a detailed explanation of the treatment of such resonances in Sec. 5.4 for the similar case of on-shell resonances in weakino-squark production. In the case of the t-channel model, the scalar mediators $\tilde{Q}_i$ can become on-shell; when they are, the relative real-emission process should then rather be seen as a tree-level production of $\chi\tilde{Q}_i$ followed by a decay $\tilde{Q}_i \to q\bar{\chi}$. For this reason, these contributions have been subtracted; in this case we used the `DSUBI` scheme, as the integration over a separate phase space for the on-shell contributions was not necessary to obtain stable results. Feynman diagrams of the real emission corrections are shown in Fig. 6.3.

6.3 Numerical implementation and setup

To perform the comparison, we performe a scan of the SUSY parameter space and then fix the parameters of the simplified models aiming to achieve the highest possible

degree of similarity between the resulting spectra. After this, we study the resulting phenomenologies using our implementations for the simplified models and the weakino code for the MSSM. After this, we perform a detailed comparison of these results.

For our `POWHEG-BOX` implementation of the simplified models at the NLO level, we need to provide the Born, virtual and real emission matrix elements and to handle the subtraction of the on-shell contributions in the t-channel model.

The Born and real-emission amplitudes are generated using a tool based on `MadGraph 4` [131–133]. This tool also provides the spin- and colour-correlated Born amplitudes, which are necessary to build the subtraction terms used in the FKS formalism, which we discussed in Sec. 4.5 and is implemented in the `POWHEG-BOX` to ensure the removal of infrared divergences in virtual and real contributions. The virtual amplitudes are generated using the two Mathematica packages `FeynArts 3.9` [134] and `FormCalc 9.4` [135]. To compute the one-loop integrals, we use the fortran-based library `COLLIER 1.2` [158–160].

The external quark fields are renormalised using the on-shell scheme and, in the t-channel model, we use the $\overline{\text{MS}}$ scheme for the mediator fields and masses. Other parameters do not require normalisation at NLO QCD. After renormalisation, all the results of our calculations are UV-finite.

To perform our scan of the SUSY parameter space, we use two of the constrained MSSM scenarios that we presented in Sec. 2.4.4, namely the CMSSM and the pMSSM10. For each of them, we choose points within a restricted range of the parameters, which is shown in table 6.1. For each point, we will then generate the respective SUSY spectrum, using the spectrum generator `SPheno 4.0.3` [161, 162]. We then check that two specific conditions are met: The first is that the lightest neutralino $\tilde{\chi}_1^0$ is the LSP and the second is that the lightest Higgs boson h is compatible with the experimentally observed one, i.e. it has a mass between 124 and 126 GeV. When a spectrum satisfies both criteria, it is accepted. We stop when for both scenarios we have 5000 accepted spectra. We observed that the points are quite evenly distributed over the parameter space available, with some areas relatively less populated, as an effect of the conditions we have imposed.

The parameters of the simplified models have to be fixed in order to be as close as possible to the MSSM and to keep the models as simple as possible. For the mass of the dark matter candidate χ, a natural choice is to set it equal to the mass of the lightest neutralino, i.e. $m_\chi = m_{\tilde{\chi}_i^0}$. For the mass of the vector mediator V, we will consider two values, $M_V = 1$ TeV and $M_V = 10$ TeV, to cover two different cases: In the first one, the mediator is too light to decay on-shell into a pair of DM particles ($M_V \lesssim 2m_\chi$), and in the second one, the mediator is heavy enough that the on-shell effects contribute negligibly to the process, considering the high values of centre-of-

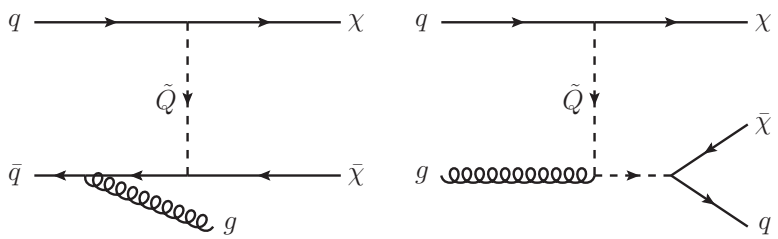

Figure 6.3: Selection of Feynman diagrams of the real corrections for the t-channel model: a real-emission process without any on-shell resonances (left) and one where the mediator $\tilde{Q}$ can become resonant(right).

CMSSM	pMSSM10	
$M_0 \in [0, 10]$ TeV	$M_1 \in [-1, 1]$ TeV	$M_2 \in [0, 4]$ TeV
$m_{1/2} \in [0, 10]$ TeV	$M_3 \in [-4, 4]$ TeV	$m_{\tilde{q}_{1/2}} \in [0, 4]$ TeV
$A_0 \in [-3, 3] \times M_0$	$m_{\tilde{q}_3} \in [0, 4]$ TeV	$m_{\tilde{l}} \in [0, 2]$ TeV
$\tan\beta \in [2, 60]$	$M_A \in [0, 4]$ TeV	$A \in [-5, 5]$ TeV
$\operatorname{sign}\mu > 0$	$\mu \in [-5, 5]$ TeV	$\tan\beta \in [1, 60]$

Table 6.1: The ranges of the free parameters of the CMSSM and pMSSM10 in which the scan was performed.

mass energies $\sqrt{S}$ that we discuss in the context of LHC searches ($2m_\chi \ll M_V \sim \sqrt{S}$). For the t-channel model, we will use the same values of the masses for all the scalar mediators, as we already stated. We choose this mass to be equal to the average of the ten light-flavour squark masses, meaning:

$$M_{\tilde{Q}} = \frac{m_{\tilde{u}_L} + m_{\tilde{u}_R} + m_{\tilde{d}_L} + m_{\tilde{d}_R} + m_{\tilde{c}_L} + m_{\tilde{c}_R} + m_{\tilde{s}_L} + m_{\tilde{s}_R} + m_{\tilde{b}_1} + m_{\tilde{b}_2}}{10}. \quad (6.3)$$

The last free parameters of the simplified models are the couplings. We reduce the number of parameters, as anticipated, by choosing a unified coupling for each model, namely $\tilde{g}$ for the s-channel model and $\tilde{\lambda}$ for the t-channel model. We then have to choose a value for these couplings such that the ratio of the mediator width to its mass is significantly smaller than one, in order to justify the narrow-width approximation. We set $\tilde{g} = 0.5$ and $\tilde{\lambda} = 1$ and checked the relative width-to-mass ratios using the Eqs. 6.1-6.2. The resulting ratios are clearly much smaller than one, as shown in Fig. 6.4, and therefore these choices can be maintained.

It is possible to calculate the corresponding DM relic abundance for the CMSSM and pMSSM10 points, but we have not used this result as a contraint for the selection of parameter points, because the theoretical calculation of the relic density is based on several assumptions [163]. The numerical value has been very accurately measured, but eventual differences between the calculated value and the observed one could be due to the inaccuracy of any of these assumptions: there could be, for example, additional fields in the dark sector or alternative production channels that are not being considered in the calculation. Therefore, even if a model apparently leads to a value of the relic abundance that is incompatible with the observations, this does not exclude the model. We, however, checked that our scan includes points for which the resulting DM abundance is compatible with the observed one.

6.4 Phenomenological results

We can now study the LHC phemenology of both approaches. We fix the hadronic centre-of-mass energy as $S = 13$ TeV. We use the PDF set PDF4LHC15 NLO MC [164], accessed via the `LHAPDF 6` library [153]. We work in the five-flavour scheme, assuming five massless quark flavour contributing to the initial state and to determine the running of $\alpha_S(\mu_R)$, where μ_R is the renormalisation scale. The renormalisation and factorisation scales μ_R and μ_F are set equal to the sum of the final-state masses, which means in our case $\mu_R = \mu_F = 2m_\chi$. We include parton-shower effects using the generator `PYTHIA 6.4.25` [21], switching off the effects related to QED radiation

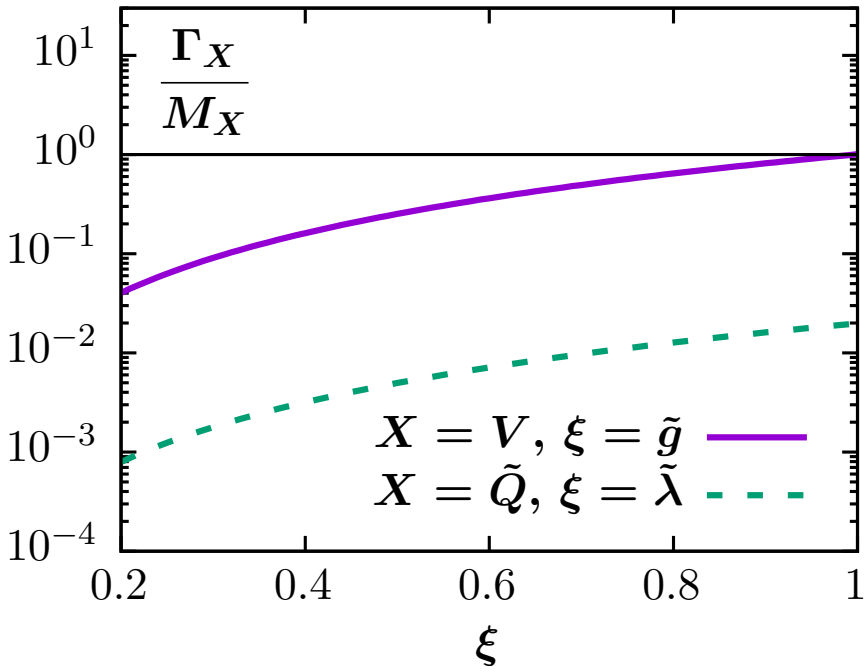

Figure 6.4: Ratio of mediator width Γ_X to mediator mass M_X for the two cases of a vector mediator V in the s-channel model (solid purple) and the scalar mediator $\tilde{Q}$ in the t-channel model (dashed green), as a function of the corresponding coupling ($\xi = \tilde{g}$ or $\xi = \tilde{\lambda}$). The other parameters are fixed to $M_V = 10$ TeV, $M_{\tilde{Q}} = 3$ TeV, and $m_\chi = 100$ GeV.

and hadronisation. Finally, to reconstruct jets, we use the `FastJet 3.3.0` [165, 166] package, using the anti-k_T [154] algorithm with $R = 0.4$ and $\eta^{jet} < 4.5$.

Before moving to the actual comparison between simplified models and the MSSM, we first look at some features of the t-channel model regarding the on-shell resonances. The resonant contributions are subtracted by manually extracting the resonant diagrams from the `MadGraph`-generated routines and then adding the relative counterterm before the integration. For this procedure, we have to introduce an artifical regulator Γ, as discussed before. We use as regulator the physical width of the mediators as calculated in Eq. (6.2). We found that the total cross section is essentially independent of this value, meaning that the removal procedure is well defined. We also checked that the resonant contributions have a significant impact on the total cross section for DM pair production. We plot the ratio of the cross sections, before and after the subtraction of on-shell contributions, in Fig. 6.5 using the points generated for the pMSSM10 to fix the parameters of the simplified model. As expected, the largest effects are to be found in regions where $M_{\tilde{Q}} \approx m_\chi$, where the difference between the cross section can be as large as a factor of five. We will then, in the remainder of this work, always subtract resonant contributions from the t-channel results.

6.4.1 Phenomenology of the CMSSM

In this section we compare the total cross section in the CMSSM and in the simplified models. In Fig. 6.6, we show the ratios of total cross sections in the simplified models to the ones in the MSSM, with the axes being chosen as m_0 and $m_{1/2}$. The other CMSSM parameters vary implicitly in the above-mentioned ranges. This results in a range for the mass of the DM candidate between approximately 100 GeV and 5 TeV. The magnitude of the ratios is colour-coded, with purple indicating low and yellow

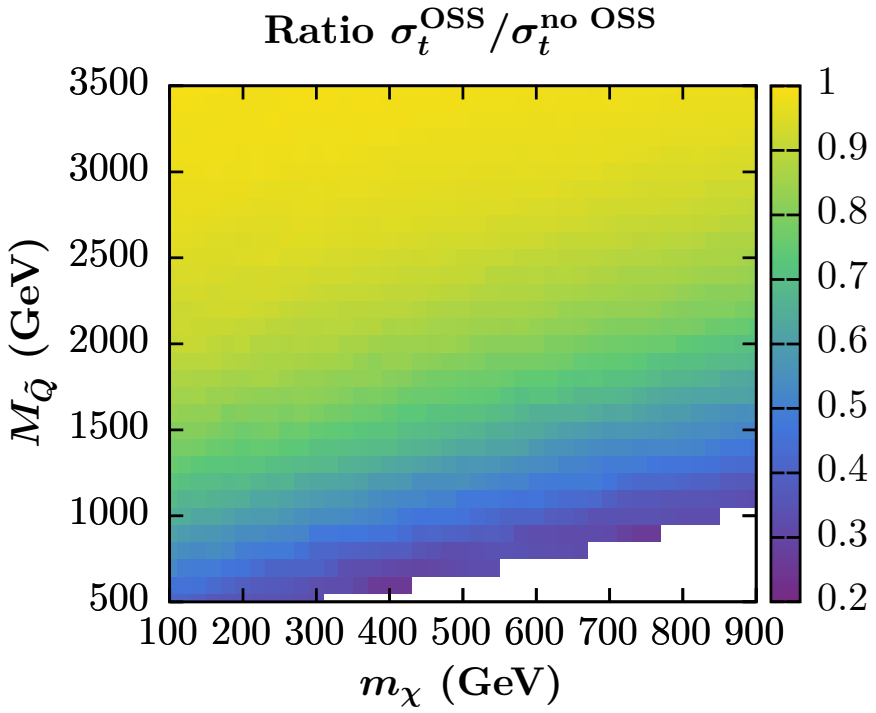

Figure 6.5: Ratio of the total cross section for DM-pair production in the t-channel model at NLO-QCD after the removal of on-shell contributions to the same quantity without on-shell subtraction.

very high ratios. We will generally not be interested in the absolute values of the ratios that can be rescaled by varying the values of the couplings in the simplified models, but rather in their relative variations over the considered range using always the same values for the couplings of the simplified models.

In Fig. 6.6(a), we show the case of the s-channel model with $M_V = 1$ TeV and in Fig. 6.6(b) the case of the s-channel model with $M_V = 10$ TeV. This difference has clearly observable results: for the region where $m_{1/2} > 2$ TeV, the case with the lighter mediator shows a relatively flat behaviour, with differences of at most one order of magnitude, while the one with a heavier mediator shows a large increase of the ratio for growing values of $m_{1/2}$, with differences of up to six orders of magnitude. An exception in both cases is observable for points with $m_0 > 7$ TeV and 2 TeV $< m_{1/2} <$ 6 TeV, which we will discuss in detail below.

The different structures can be understood as a consequence of the resonant behaviour of the s-channel mediator. The propagator of the mediator becomes resonant for $M_V = 2m_\chi$, leading to an increase of the cross section in the s-channel model and therefore of the ratio, because in the MSSM such resonant structures would be observed for much lower values of m_χ, since the mediator of the MSSM s-channel diagram is the Z boson. The effect of the resonance can be observed in Fig. 6.6 (a) for low $m_{1/2} < 2$ TeV and also in Fig. 6.6 (b) for high $m_{1/2} \approx 10$ TeV. The mass m_χ is equal to $m_{\tilde{\chi}_1^0}$, which is closely connected to $m_{1/2}$: at the lower edge of the parameter plane, m_χ is around 500 GeV and therefore triggers the resonance for the vector mediator with $M_V = 1$ TeV, while at the upper edge m_χ is around 5 TeV, thus causing the increase of the cross section in the $M_V = 10$ TeV case.

The case of the t-channel model is shown in Figs. 6.6 with a logarithmic (c) and a linear (d) colour scale, respectively. From these two plots it becomes clear that over the whole parameter range, the ratio varies by less than one order of magnitude, with

the exception of points with $m_0 > 7$ TeV and 2 TeV $< m_{1/2} <$ 6 TeV, as before. The linear colour scale reveals that for most of the parameter space, the ratio varies at most by a factor of three, which indicates a great overall similarity to the MSSM in contrast to the case of the s-channel model. This can be explained by the fact that the t-channel mediators of this model are similar to the squarks in their masses, while the s-channel model mediators are much heavier than the Z-boson.

We still have to explain the enhancement of the ratios in the points with $m_0 > 7$ TeV and 2 TeV $< m_{1/2} <$ 6 TeV. In this region, the ratio is enhanced by several orders of magnitude compared to the surrounding points. Investigating the possible causes of this effect we noticed some peculiar features of these points. The first is that the mass $m_{\tilde{\chi}_1^0} = m_\chi$ is significantly lower than for the surrounding points; however, this affects both cross sections in a similar way and should not have a big impact on their ratio. The second, and more significant, feature concerns the composition of the lightest neutralino. We discussed the composite nature of the neutralinos in Sec. 2.4.3: they have a bino, wino and two higgsino components, whose weight is determined by the neutralino mixing matrix N_{ij}. In most of the parameter space we investigated, the dominant component of $\tilde{\chi}_1^0$ is the bino. As a consequence, the dominant contribution to the $\tilde{\chi}_1^0$ pair production process comes from diagrams with squark exchange, i.e. the centre and right one in Fig. 6.1. For the enhanced points, instead, $\tilde{\chi}_1^0$ is dominantly a mix of the two higgsino components, meaning that the squark exchange diagrams are suppressed, and the major contribution should come from the left-hand-side diagram in Fig. 6.1. However, this contribution is proportional to the difference of the absolute squared values of the neutralino mixing matrix elements for the higgsino components [167, 168], i.e. $\mathcal{M}_{Z\text{-boson}} \propto |N_{14}|^2 - |N_{13}|^2$ (see Sec. 2.4.3 for more details). We noticed that for all these points, $|N_{13}|$ and $|N_{14}|$ are similar in size, leading to this contribution being suppressed as well. Therefore, all the diagrams contributing to the MSSM cross section are suppressed, while the simplified model ones are unaffected by these effects, as they do not have a feature equivalent to the neutralino mixing matrix. This leads to the strong enhancement of the observed ratio. We will refer to this effect as the "higgsino mixing-matrix suppression" in the following sections.

6.4.2 pMSSM10 phenomenology

We now discuss the phemenology of DM pair production in the pMSSM10 scenario. The paramater space is now ten-dimensional, meaning that, as in the previous case, we have to select two parameters in order to obtain two-dimensional plots, with all other parameters always varying implicitly. We choose to use the modulus of the Higgsino mass parameter $|\mu|$ and the SUSY-breaking wino mass M_2, because this choice allows for an easy differentiation between a (predominantly) bino, a wino, and a higgsino composition of $\tilde{\chi}_1^0$.

The plot where we visualise the amplitude of the mixing matrix elements using a colour-scheme based on the composition of the lightest neutralino in each point is shown in Fig. 6.7. The colour indicates the dominant component, where a component is considered dominant if the corresponding square of the absolute value of the mixing matrix element $|N_{1i}|^2$ is larger than 0.5. The majority of points contain a bino-like $\tilde{\chi}_1^0$, with, in most cases, $|N_{11}|^2 \geq 0.99$. The wino and higgsino components are instead dominant for low M_2 and $|\mu|$, respectively. If no component $|N_{1i}|^2$ is larger than 0.5, the point is considered a "mixed" point. Most points labelled as "higgsino" and "mix" up to $|\mu|$ values of around 700 GeV show a suppression of the MSSM cross section due to the higgsino mixing-matrix suppression that we discussed in the previous section,

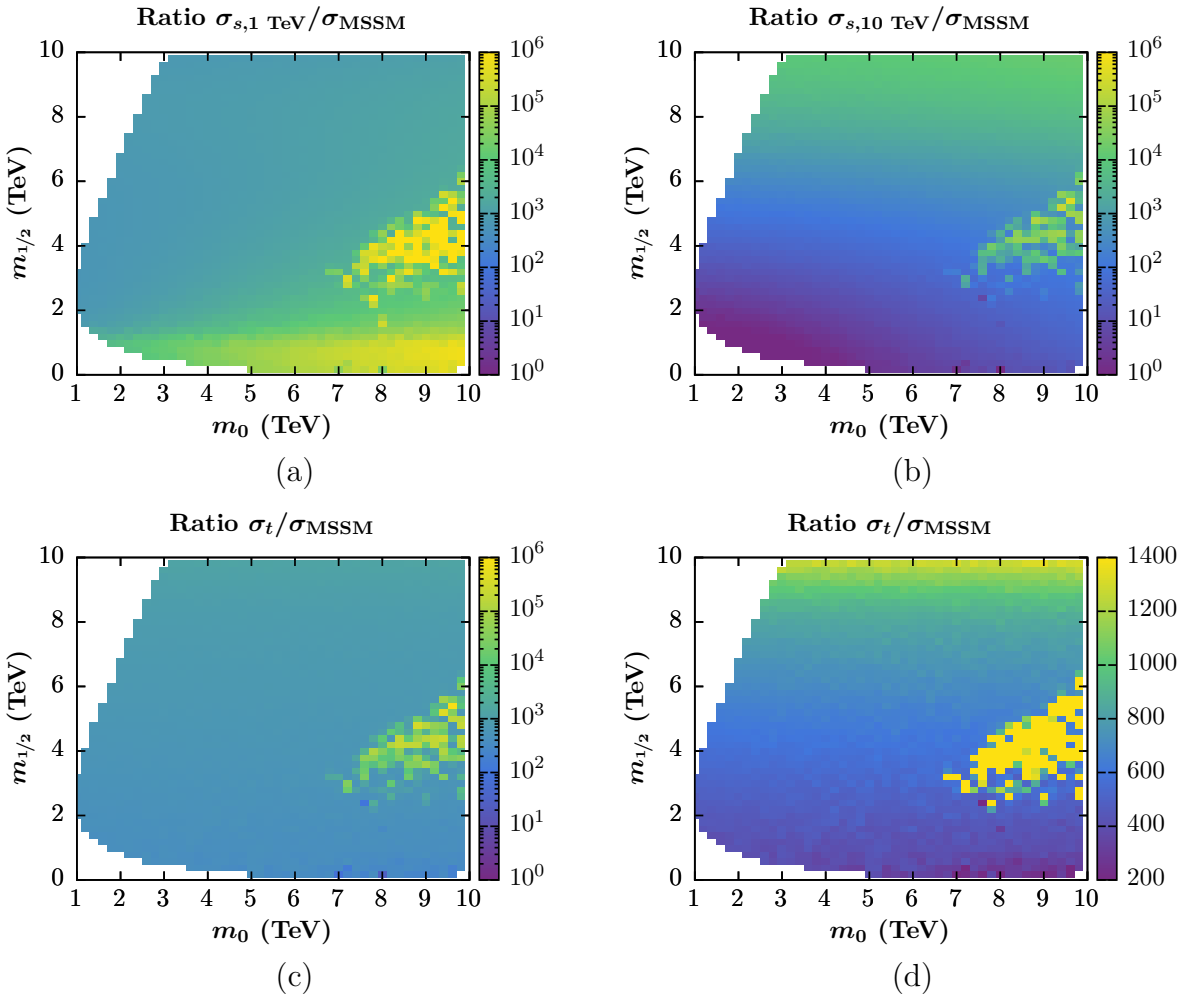

Figure 6.6: Ratios between the total cross sections for DM pair production in simplified models and the ones in the MSSM, in the plane of the CMSSM parameters m_0 and $m_{1/2}$, with all other parameters varied implicitly. Shown are the s-channel models with $M_V = 1$ TeV (a) and $M_V = 10$ TeV (b), and t-channel model with a logarithmic (c) and a linear (d) colour scale, respectively. White regions denote points excluded in the parameter space where the lightest neutralino is not the LSP and therefore not a DM candidate or where radiative electroweak symmetry breaking is not possible (bottom left corner). Rough edges are an interpolation effect.

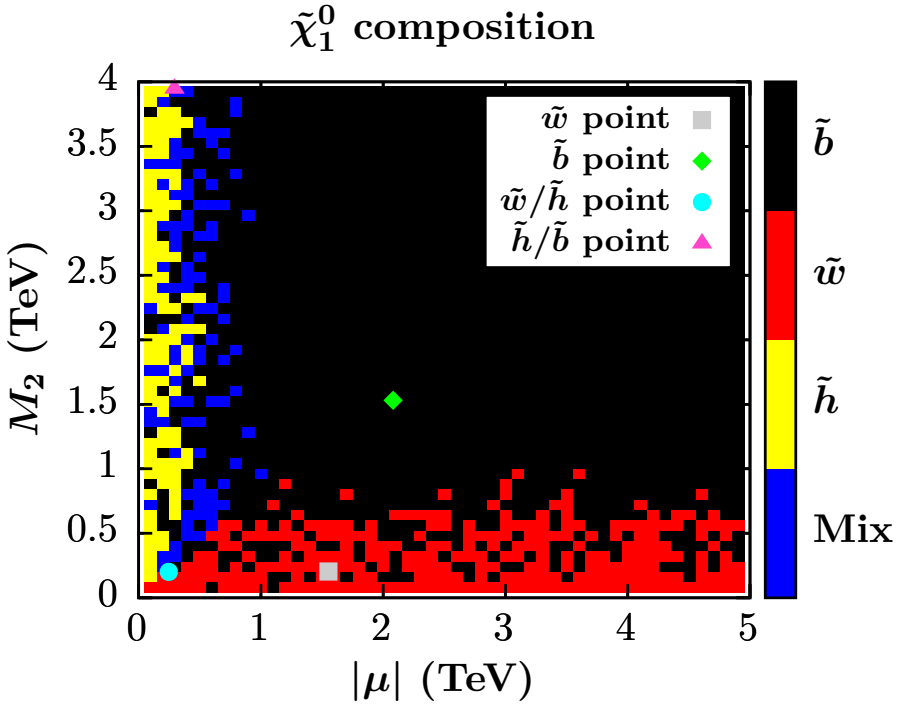

Figure 6.7: Composition of the lightest neutralino $\tilde{\chi}_1^0$ in the $|\mu|$ – M_2 plane. A point is dominantly bino-like ($\tilde{b}$, black) for $|N_{11}|^2 > 0.5$, dominantly wino-like ($\tilde{w}$, red) for $|N_{12}|^2 > 0.5$, dominantly higgsino-like ($\tilde{h}$, yellow) for $|N_{13}|^2 > 0.5$ or $|N_{14}|^2 > 0.5$, or a mix of all components ("mix", blue) in any other case, i.e. if neither $|N_{1i}|^2$ is larger than 0.5. For later discussion four specific points referred to as $\tilde{w}, \tilde{b}, \tilde{w}/\tilde{h}$, and $\tilde{h}/\tilde{b}$ are highlighted.

leading to an enhancement of the ratio in those points.

Similar to the previous discussion for the CMSSM, in Fig. 6.8 we show the ratios between total cross sections for DM pair production in simplified models and in the MSSM constrained scenario in consideration. The ratios for the s-channel models with $M_V = 1$ TeV and $M_V = 10$ TeV are shown in the top plots, left and right respectively. Both cases show a similar range of relative variation, with the absolute values in the right plot being smaller because of the higher mass in the s-channel propagator. For 100 GeV $< |\mu| <$ 700 GeV, we observe the by-now familiar enhancement of the ratio due to the higgsino mixing-matrix suppression. In the central area of the plots, there are seemingly random variations of the cross section of up to three orders of magnitude. Some structures are, however, observable at the edges. For very low values of $|\mu|$ and M_2, the mass $m_{\tilde{\chi}_1^0}$ becomes very low, triggering a resonant behaviour of the Z-boson in the MSSM for $m_{\tilde{\chi}_1^0} \approx M_Z/2$. In these areas, in both plots, the ratio is lower because of the enhancement of the MSSM cross section. This effect is particularly relevant for the heavier s-channel mediator mass $M_V = 10$ TeV, while for the second case, with a lighter mediator, its own enhancement coming from the resonance of the s-channel mediator partially compensates the MSSM effects, leading to a larger ratio.

Fig. 6.8 (c) shows the ratio of the cross sections in the t-channel model to the MSSM cross sections. We observe structures similar to the ones just discussed: there is a region with an enhanced ratio for 100 GeV $< |\mu| <$ 700 GeV due to the higgsino mixing-matrix suppression and a region with smaller ratio for low $|\mu|$ or M_2 due to the resonant behaviour of the MSSM cross sections. The latter is in this case not compensated in any way in the simplified models, where the t-channel mediators do not exhibit a resonant behaviour. However, the central bino region is a bit smoother

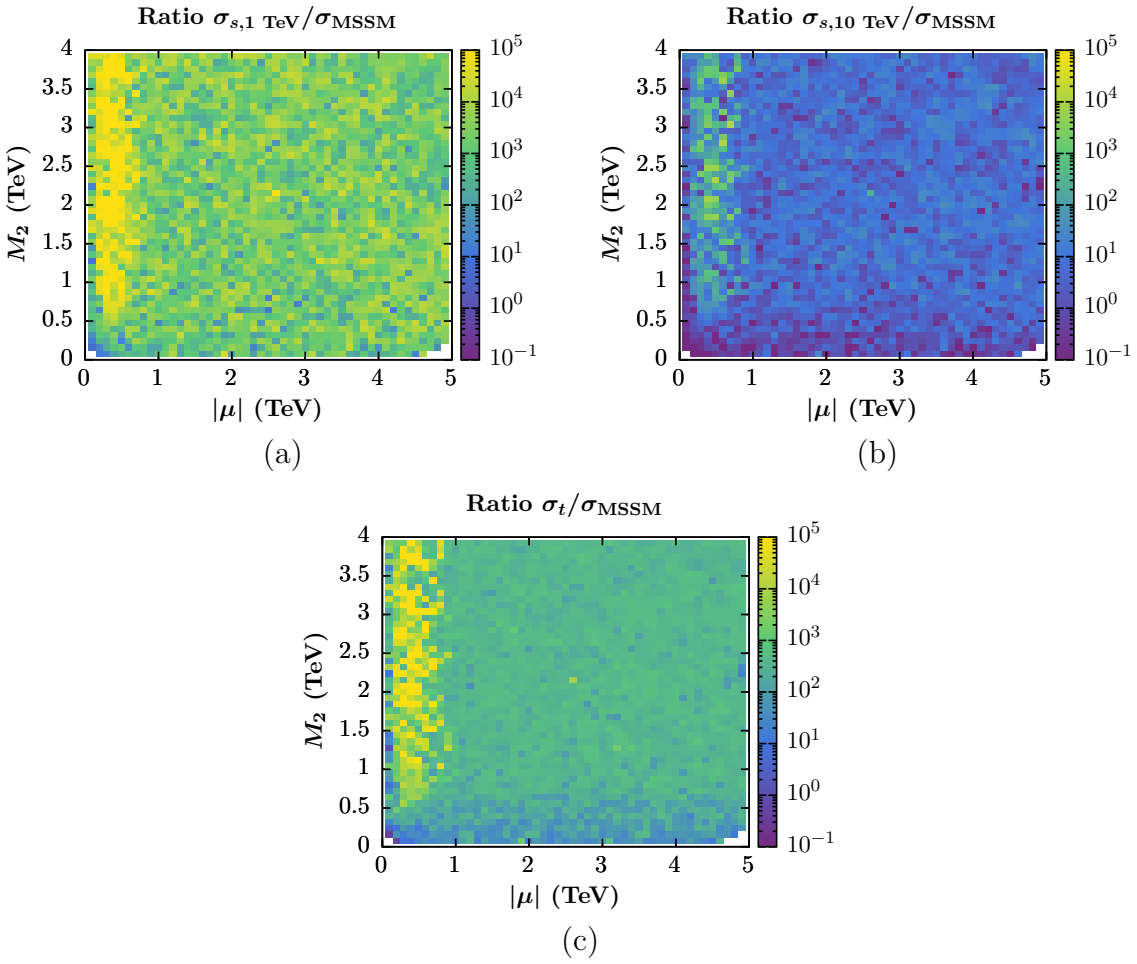

Figure 6.8: Ratios of total cross sections for DM pair production in the simplified models to the ones in the MSSM, in the plane of the pMSSM10 parameters $|\mu|$ and M_2, with all other parameters varied implicitly. Shown are the s-channel models with $M_V = 1$ TeV (a) and $M_V = 10$ TeV (b), and the t-channel model (c).

than for the s-channel model, still with seemingly random variation, but of smaller size, mostly around one order of magnitude. This behaviour can again be attributed to the similarity of the t-channel model with the MSSM: the bino-like neutralino does not couple to the Z-boson, and the only contributing diagrams are the ones including a squark exchange, which strongly resemble the simplified model ones.

It appears then that these ratios exhibit some interesting features, some of which are shared by the two simplified models. In particular, they appear to be sensible to the composition of the lightest neutralino $\tilde{\chi}_1^0$, with similar structures due to higgsino mixing-matrix suppression and resonant behaviours appearing in all of the three cases discussed. We therefore study in detail four points, each representing a specific composition of the lightest neutralino.

For these points, we look at differential distributions in the MSSM and the two simplified models. As before, for the s-channel model we consider mediator masses of $M_V = 1$ TeV and $M_V = 10$ TeV. For the t-channel model we so far always considered the case of DM made of Dirac fermions, but we now additionally show results for DM being made of Majorana fermions, which makes the model more similar to the MSSM. We compare results obtained for these models to those of the MSSM for the four representative points of the pMSSM10 parameter space highlighted in Fig. 6.7. We will focus on two observables:

- the invariant mass of the DM pair system, $M_{\chi\chi}$, which is an interesting quantity to study the characteristics of the models, even if it is not directly accessible for a pair of invisible particles;

- transverse momentum of the DM pair system, $|\vec{p}_{T,\chi\chi}|$, which is identical to the "missing transverse momentum", in an experimental context, and then strictly connected to the characteristic signal of the production of invisible particles in a collider. For simplicity, we will simply denote this quantity with $p_{T,\chi\chi}$.

In order to compare only the shapes of the distributions and not their absolute values, each distribution shown is normalised to the respective total cross section, i.e. $\hat{\sigma}_X \equiv (1/\sigma_X)\, d\sigma_X/dy$, where $\hat{\sigma}_X$ is the normalised differential cross section, σ_X is the total cross section, X specifies the model, and y denotes either $M_{\chi\chi}$ or $p_{T,\chi\chi}$. For simplicity, no cuts have been applied to any kinematical variable. All results are given at NLO+PS accuracy.

In Fig. 6.9, we show the differential distributions for a parameter point where the lightest neutralino is mainly composed of a wino, which is denoted as $\tilde{w}$ point in Fig. 6.7. For the case of the s-channel model with $M_V = 1$ TeV we observe a resonance structure peaking at $M_{\chi\chi} = M_V$ which is related to the mass of the mediator and is therefore not present for any other model. Considering the normalisation of the distributions, its differential cross section drops significantly faster than the other for higher invariant masses. The case of the heavier mediator $M_V = 10$ TeV is different, as the resonance structure is not present in the shown range of the invariant mass. For relatively low values of $M_{\chi\chi}$, this model reproduces quite well the MSSM distribution, however deviating significantly for $M_{\chi\chi} > 1300$ GeV.

The distributions for the t-channel model show the higher similarity of the model to the MSSM and the positive impact on the comparison of the choice of a Majorana fermion as the DM candidate. For the Dirac DM case, the behaviour of the t-channel model is quite different for low $M_{\chi\chi}$ values; the constant ratio for higher values means, considering the normalisation, that in that area the behaviour is actually the same. The Majorana DM case instead produces a distribution that agrees very well with the MSSM one.

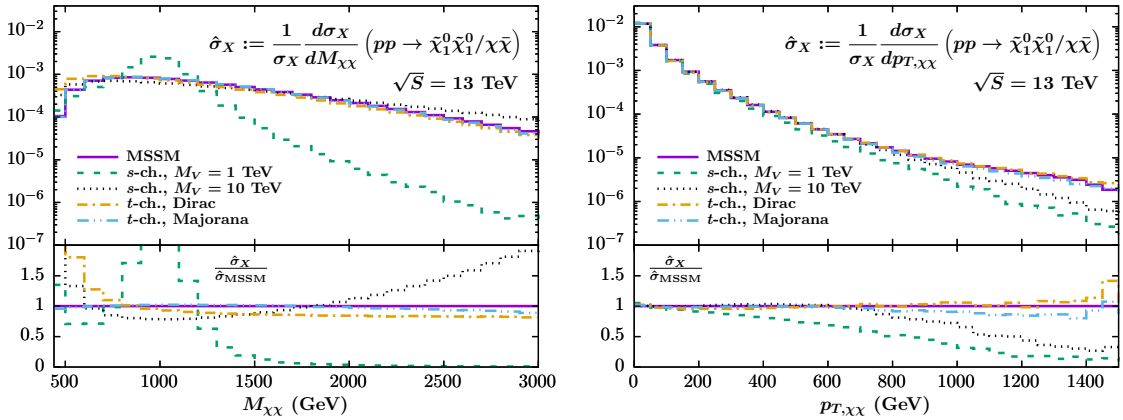

Figure 6.9: Invariant mass (left) and transverse momentum distribution (right) of the DM pair system at NLO+PS accuracy. Masses and parameters are chosen according to the $\tilde{w}$ parameter point of Fig. 6.7. Shown are predictions for the MSSM (solid purple line), the s-channel model with $M_V = 1$ TeV (dashed green line) and $M_V = 10$ TeV (dotted black line), and the t-channel model with DM as a Dirac (dash-dotted orange line) and a Majorana (dash-double dotted blue line) fermion.

The right plot of Fig. 6.9 shows the transverse-momentum distribution of the DM pair system. For low $p_{T,\chi\chi} \lesssim 200$ GeV, all models demonstrate the same behaviour. For increasing transverse momentum, the s-channel model with $M_V = 1$ TeV is the first to deviate from the MSSM at around $p_{T,\chi\chi} = 200$ GeV with a distribution dropping more quickly than in all of the other scenarios. Beyond $p_{T,\chi\chi} \approx 800$ GeV, also the s-channel model with $M_V = 10$ TeV deviates from the MSSM, as the latter demonstrates a plateau towards high $p_{T,\chi\chi}$. This plateau originates from the overlap of the decreasing behaviour of the p_T distribution and a resonance peak with its centre at half of the average of the squark masses. This peak is indeed due to the on-shell resonances of the intermediate squarks: the interference term between the non-resonant and possibly resonant amplitudes $2\,\mathrm{Re}(\mathcal{M}_{nr}\mathcal{M}_r^*)$ is not subtracted and leads to this enhancement of the cross section for $p_{T,\chi\chi} \approx M_{\tilde{Q}}/2$. This plateau is also present in the t-channel models with Dirac and Majorana DM, where the same resonant structures are present.

The good agreement between the t-channel model and the MSSM, in particular considering Majorana DM, is due to the high similarity of the two production processes: in the MSSM, for wino-like points, the Z-boson diagram is strongly suppressed, thus leaving the squark-exchange diagrams as the dominant contributions.

Fig. 6.10 shows the case of the $\tilde{b}$ point, where the lightest neutralino is dominated by the bino component. The overall agreement between the MSSM and the simplified models is in this case significantly worse. The qualitative behaviour of all the lines presents some similarities: the t-channel model with Majorana DM still presents an invariant mass distribution that lies on top of the MSSM one, but the Dirac DM case now shows a significant discrepancy from the MSSM over all the investigated range. Concerning the transverse momentum distributions, the s-channel ones are now indistinguishable, as for none of them a resonant structure is present in this case. The t-channel model distributions also do not describe the same shape of the MSSM anymore. They show only a hint of the resonance plateau that was described in the previous case, while the MSSM still clearly presents this feature.

Fig. 6.11 shows differential distributions for the point labeled $\tilde{w}/\tilde{h}$. Here, the lightest neutralino consists of a mix of a dominant wino component and a small higgsino part. The invariant mass distribution illustrates that none of the simplified models

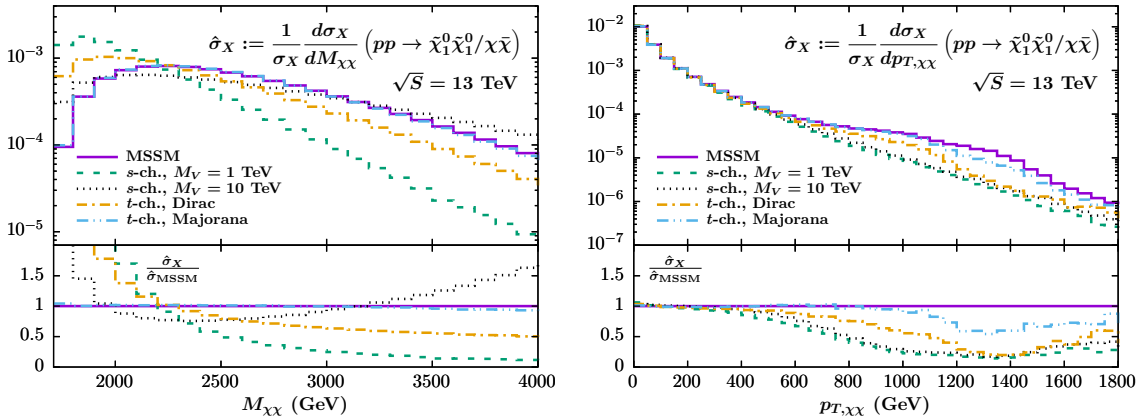

Figure 6.10: Invariant mass (left) and the transverse momentum distribution (right) of the DM pair system at NLO+PS accuracy. Masses and parameters are chosen according to the $\tilde{b}$ parameter point of Fig. 6.7. The colouring of the lines follows the scheme introduced in Fig. 6.9.

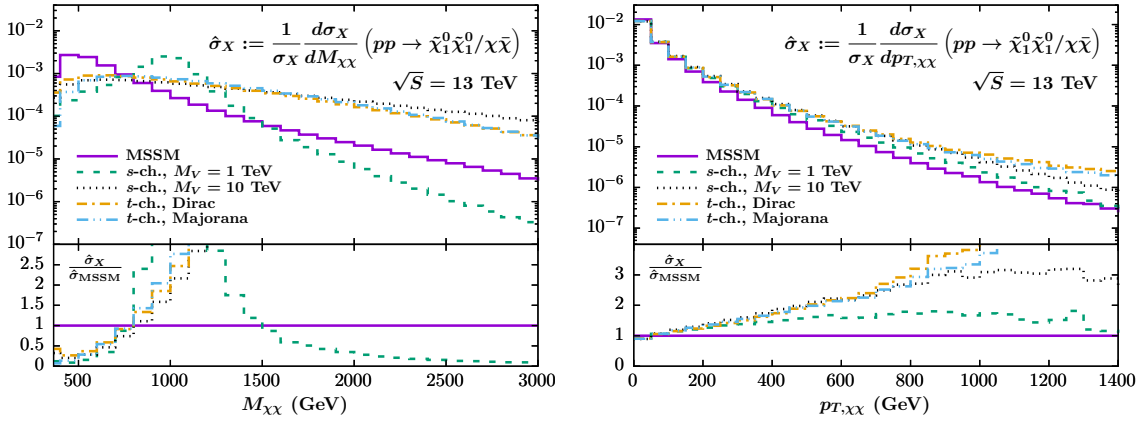

Figure 6.11: Invariant mass (left) and the transverse momentum distribution (right) of the DM-pair system at NLO+PS accuracy. The masses and parameters are chosen according to the $\tilde{w}/\tilde{h}$ parameter point of Fig. 6.7. The colouring of the lines follows the scheme introduced in Fig. 6.9.

has a similar behaviour to the MSSM: while the s-channel model with $M_V = 1$ TeV fails to describe the MSSM line due to the resonance behaviour of the mediator, the other three lines are either below the MSSM prediction for low invariant masses or far above towards high invariant masses. A similar observation can be made for the $p_{T,\chi\chi}$ distribution: all the lines of the simplified models decrease more slowly than the one of the MSSM. Only the ratio for the s-channel models is constant towards high $p_{T,\chi\chi}$. In particular the ratio of the s-channel model with $M_V = 1$ TeV appears to be approximately constant for 300 GeV $< p_{T,\chi\chi} <$ 1200 GeV.

These results indicate that a small higgsino component can have a very significant impact even for a parameter point where the wino component is dominant: in this case, we have $|N_{12}|^2 > 0.6$. This is due to the strong influence of the Z-boson diagram, which manifests itself in a poor capability of the t-channel model to approximate the behaviour of the MSSM because of the different overall structure; the s-channel model also has issues in reproducing the MSSM behaviour because of the different mass of the mediator.

Finally, predictions for the $\tilde{h}/\tilde{b}$ point are shown in Fig. 6.12. For this point, the

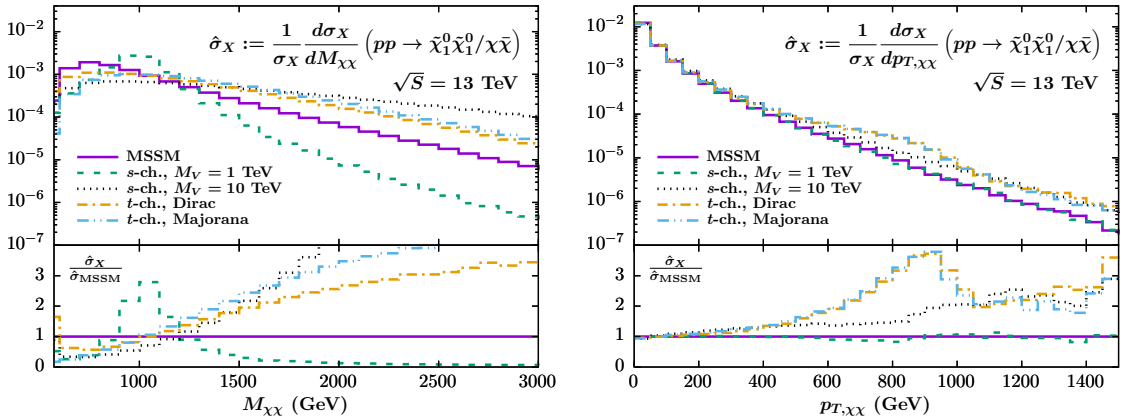

Figure 6.12: Invariant mass (left) and the transverse momentum distribution (right) of the DM pair system at NLO+PS accuracy. Masses and parameters are chosen according to the $\tilde{h}/\tilde{b}$ parameter point of Fig. 6.7. The colouring of the lines follows the scheme introduced in Fig. 6.9.

lightest neutrino is mainly a mix of the bino ($|N_{11}|^2 \approx 0.13$) and higgsino ($|N_{13}|^2 \approx 0.45$, $|N_{14}|^2 \approx 0.41$) components, while the wino component is negligible. The invariant mass distribution reveals a large discrepancy between the simplified models and the MSSM, similar in size to the previous case but different in the structure. The $p_{T,\chi\chi}$ distributions present similar behaviour. Only the $p_{T,\chi\chi}$ distribution of the s-channel model with $M_V = 1$ TeV follows the MSSM prediction, while all of the other lines lie above the MSSM with a non-constant ratio.

The worsening in the agrement between the MSSM and the t-channel models is due to the peak-like structure at around $p_{T,\chi\chi} \approx 900$ GeV, which is related to the on-shell subtraction of intermediate t-channel mediators, as discussed previously. In this case, however, this structure is only visible in the t-channel model, as in the MSSM the dominant contribution comes from the Z-boson exchange diagram.

Chapter 7

Direct detection of dark matter: NLO calculations in simplified models

In this chapter we discuss the work published in [27]. We performed the calculation of next-to-leading order (NLO) QCD corrections for the scattering of DM particles off nucleons in the simplified models with s- and t-channel mediators and with both mediators present simultaneously, which we call $s+t$-channel simplified model. We also matched our results to the Wilson coefficients and operators of a low-energy effective field theory to present our results in the framework of direct DM searches. We used our findings to investigate the different reach of collider searches and the direct detection experiments CRESST and XENON.

NLO QCD corrections to the direct detection rates in the context of simplified models can be used to improve theoretical predictions, as they are less severely affected by theoretical uncertainties. As already mentioned, this chapter follows closely the discussion from our publication [27]. We begin with an expanded overview of direct detection of DM and of the calculation of matrix elements for simplified models in the non-relativistic limits. We also discuss in detail the matching procedure necessary to connect our results to experimentally accessible quantities. To conclude the chapter, we present our numerical results.

7.1 Direct detection of dark matter

In Sec. 3.5.2, we mentioned the framework of direct DM searches. We will now illustrate in detail how these searches are performed and what the ingredients necessary for a quantitative description are.

As we anticipated, the goal is to detect low-energy scattering events between DM particles, which are present as a result of the local DM density ρ_0, and target nuclei in specifically built detectors. These events will have as a signature the transfer of a small quantity of energy from the DM particles to the nuclei, leading to a recoil of the latter, which can be measured if all the sources of background, e.g. cosmic muons or neutrinos, are under control. The experimental signature of a DM particle of mass m_χ scattering elastically off a nuclear target particle of type i and mass m_i is given by the differential rate of nuclear recoil events dR per energy interval dE,

$$\frac{dR}{dE} = \sum_i k_i \frac{\sigma_i}{2 m_\chi \mu_i^2} \rho_0 \eta_i \,, \tag{7.1}$$

where k_i denotes the mass fraction of nuclear species i in the detector, σ_i the DM-nucleus scattering cross section and μ_i the reduced mass of the DM-nucleus system,

$$\mu_i = \frac{m_\chi m_i}{m_\chi + m_i} \,. \tag{7.2}$$

The quantity η_i depends on the distribution of the velocity v of the DM particles relative to the detector,

$$\eta_i = \int_{v_{min,i}}^{v_{esc}} d^3v \frac{f(\vec{v})}{v}, \tag{7.3}$$

where the integration range is determined by the minimum velocity $v_{\mathrm{min},i} = \sqrt{\frac{m_i E}{2\mu_i^2}}$ of the DM particle required to cause a recoil energy E in the detector, and the galactic escape speed v_{esc} beyond which DM particles are no longer gravitationally bound in the Milky Way. $f(\vec{v})$ is the local velocity distribution in the detector rest frame. We assume DM particles to move at non-relativistic velocities of about $v \sim 10^{-3}c$ [169], in agreement with the cold DM hypothesis. Assuming the nuclei in the detector to be at rest, typical recoil energies, which are proportional to the momentum exchange q between the DM particles and the nuclei, are of the order of a few to a few hundred keV. We will therefore work in the limit of vanishing relative momentum between scattering DM particle and nucleus, where $q^2 \to 0$, and refer to it as the non-relativistic limit.

In the differential detection rate of Eq. (7.1) all information on the microscopic DM-nucleus interaction is contained in the elastic DM-nucleus cross section σ_i, while the other quantities entering the equation are related to the detector composition and the DM relic density. In the non-relativistic limit, this elastic scattering cross section receives contributions from so-called spin-independent (SI) and spin-dependent (SD) interactions. The cross section σ_i therefore can be conveniently divided into an SI (σ_i^{SI}) and an SD (σ_i^{SD}) part. The strength of the contribution will differ for different types of nuclei, as the SI part is enhanced for heavy nuclei, while this enhancement is not present for the SD part [170]. In order to allow for easier comparisons between different experimental setups using different detector materials, results are usually expressed in terms of the cross sections of the scattering between a single nucleon and a DM particle, keeping the division between the SI (σ_N^{SI}) and SD (σ_N^{SD}) parts. In this work, we present our results in this common framework.

A comment is in order concerning the local DM density, since its value ρ_0 enters directly the expression for the detection rate. Since no DM particles has ever been detected, this quantity obviously has not been directly measured. Therefore, ρ_0 is fixed with the aid of some assumptions, such as the DM relic abyndance as measured through the CMB. The direct detection experiments have been used to set upper bounds on the cross section σ_i and its components σ_N^{SI} and σ_N^{SD}. When considering specific models, these bounds can be translated into limits on the masses and the couplings of the DM candidate in consideration. Therefore, the assumptions made to choose a value of ρ_0 directly affect the limits obtained.

To calculate the cross section σ_i, we start our discussion from the description of the elastic DM-nucleon scattering in the non-relativistic limit. This low-energy regime allows us to treat the scattering event as an effective four-fermion interaction like the one shown in Fig. 7.1, which can be parameterized in terms of effective operators. We therefore start our discussion with an effective Lagrangian in relativistic notation with

DM-quark interaction terms of the form

$$\begin{aligned}\mathcal{L}_{\mathrm{EFT}}^{\mathrm{int},\chi q} &= c_S\,\mathcal{O}_S + c_V\mathcal{O}_V + c_A\,\mathcal{O}_A + c_T\mathcal{O}_T \\ &= c_S\,[\bar{\chi}\chi\,\bar{q}q] + c_V\left[\bar{\chi}\gamma^\mu\chi\,\bar{q}\gamma_\mu q\right] \\ &\quad + c_A\left[\bar{\chi}\gamma^\mu\gamma_5\,\chi\bar{q}\gamma_\mu\gamma_5 q\right] - \frac{1}{2}c_T\left[\bar{\chi}\sigma^{\mu\nu}\chi\,\bar{q}\sigma_{\mu\nu}q\right], \end{aligned} \tag{7.4}$$

with χ being the DM field, q being the quark field, $\sigma_{\mu\nu} = \frac{i}{2}[\gamma_\mu, \gamma_\nu]$, and a priori unknown Wilson coefficients $c_j \equiv c_{j,q}$ which in general depend on the quark flavour q. This Lagrangian contains the effective dimension-six operators $\mathcal{O}_j$ accounting for scalar, vector, axial-vector, and tensor interactions of four fermions. These are the only operators that are not suppressed by small non-relativistic velocities. In the low-energy regime we are considering, mixed operators, such as e.g. $\bar{\chi}\gamma^\mu\chi\,\bar{q}\gamma_\mu\gamma_5 q$, are kinematically suppressed and will therefore not be discussed further. In the non-relativistic limit, the scalar and vector operators induce SI, the axial-vector and tensor operators SD interactions.

In order to derive from the EFT Lagrangian the scattering cross sections relevant for direct detection experiments, we can compute for each term in the Lagrangian the matrix element

$$\mathcal{M}_{j,q} = c_{j,q}\,\left(\bar{\chi}\Gamma_j\chi\right)\,\left(\bar{q}\Gamma_j q\right), \tag{7.5}$$

where for $j = S, V, A, T$ the Γ_j stands for $1, \gamma_\mu, \gamma_\mu\gamma_5, \frac{i}{\sqrt{2}}\sigma_{\mu\nu}$, respectively. For computing quantities involving nucleons rather than elementary quarks, we adopt the conventional assumption that, in the non-relativistic limit, quark operators within nucleonic states are proportional to nucleonic operators. This effectively leads to a replacement of the quark fields by nucleon fields [171],

$$\bar{q}\,\Gamma_j q \quad \longrightarrow \quad \sum_q f_{j,q}^N\,\bar{N}\Gamma_j N, \tag{7.6}$$

with the nucleonic matrix elements $f_{j,q}^N$ as proportionality factors, which encode the non-perturbative contributions from hadronic physics and are typically calculated in lattice-gauge theory or determined experimentally. The $f_{j,q}^N$ depend on the type of the nucleon $N = p, n$, the interactions j, and the quark flavour q. In our calculations we use the numerical values for the $f_{j,q}^N$ listed in Tab. 7.1. They have been extracted from the program `MicrOMEGAs` [78, 79], version 5.0.9. Note that values of the vector, axial-vector, and tensor coefficients for neutrons can be obtained from the respective proton coefficients using isospin symmetry, i.e. by switching the d and u columns.

Since we will be calculating cross sections relative to the nucleons, a summation over all active quark flavours has to be performed. We therefore introduce the nucleonic

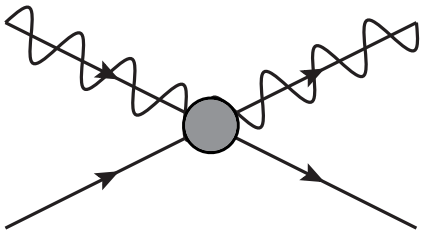

Figure 7.1: Tree-level Feynman diagram for DM-quark scattering in the effective theory, where the four-fermion interaction is indicated by a grey circle.

couplings

$$g_j^N = \sum_q f_{j,q}^N c_{j,q}, \tag{7.7}$$

for each interaction type j. The matrix elements $\mathcal{M}_{j,q}$ from Eq. (7.5) have to be substituted by the nucleonic ones $\mathcal{M}_{j,N}$, performing the substitution introduced in Eq. (7.6). The total cross section for nucleon scattering in the non-relativistic limit is then equal to:

$$\sigma_N = \frac{1}{16\pi s}\overline{\sum_{pol.}}\sum_j |\mathcal{M}_{j,N}|^2 = \frac{1}{16\pi s}\overline{\sum_{pol.}}|\mathcal{M}_N|^2, \tag{7.8}$$

where the averaging over initial-state and the summing over final-state polarisations and colours have to be taken into account and are indicated by the bar over the sum. In the non-relativistic limit, the center-of-mass energy squared of the DM-nucleon system can be written as $s = \left(m_\chi + m_N\right)^2$, with m_N being the mass of the considered nucleon.

Distinguishing between the contributions to SI and SD scattering and evaluating the fermionic traces within the squared amplitude, we obtain

$$\sigma_N^{\mathrm{SI}} = \frac{\mu_N^2}{\pi}\left|g_S^N \pm g_V^N\right|^2 = \frac{\mu_N^2}{\pi}\left|g_{\mathrm{SI}}^N\right|^2, \tag{7.9}$$

$$\sigma_N^{\mathrm{SD}} = \frac{\mu_N^2}{\pi}\left|g_A^N \pm g_T^N\right|^2 = \frac{\mu_N^2}{\pi}\left|g_{\mathrm{SD}}^N\right|^2, \tag{7.10}$$

with the reduced mass μ_N of the DM-nucleon particle system. The positive sign between the contributions from the different Wilson coefficients corresponds to DM scattering. The cross section relative to anti-DM scattering contains instead a minus sign between the different contributions.

Having calculated the cross section in terms of Wilson coefficients, it is necessary to know their expressions in terms of the parameters of the simplified models. In order to obtain them, the matrix elements of the simplified models have to be calculated and then matched to the matrix elements in the EFT consisting of the Wilson coefficients and the operators. We will first calculate the matrix elements for the s- and t-channel simplified models and then match them to the EFT at the NLO in QCD. A similar calculation has been carried out for the neutralino-parton scattering in the context of the MSSM [172] and we have based our procedure on the one described in this reference.

	quark flavour			
	d	u	s	c, b, t
$f_{S,q}^p$ (f_q^p)	0.0191	0.0153	0.0447	0.0682
$f_{S,q}^n$ (f_q^n)	0.0273	0.0110	0.0447	0.0679
$f_{V,q}^p$ $(f_{V_q}^p)$	1	2	0	0
$f_{A,q}^p$ (Δ_q^p)	−0.427	0.842	−0.085	0
$f_{T,q}^p$ (δ_q^p)	−0.230	0.840	−0.046	0

Table 7.1: Numerical values of the nucleonic matrix elements used in this work, taken from [78, 79]. Indicated in brackets are alternative names of the coefficients commonly used in the literature [171].

7.2 Matrix elements for simplified dark matter models in the non-relativistic limit

In Sec. 3.4 we introduced two simplified models for DM, namely the s- and t-channel models. In that section, we gave the expressions for their Lagrangians and discussed the properties of their DM candidates, which are Dirac fermions, and of their mediator particles, i.e. a vector in the s-channel model and coloured scalars in the t-channel model. The names of these models models are referring to the kinematic structure of DM pair production processes at a collider. In DM-nucleon scattering events, the interactions at the parton level would instead correspond to the topologies shown in Fig. 7.2.

Since we are working in the non-relativistic limit ($q^2 \to 0$), the centre-of-mass energy squared of the DM-quark system is equal to $\hat{s} = (m_\chi + m_q)^2$ and the square of the momentum transfer between the incoming DM particle and the outgoing quark is $\hat{u} = (m_\chi - m_q)^2$. In our calculation, we will always keep the explicit $\hat{u}$ dependence. We will show results for DM-quark scattering, but corresponding expressions for anti-DM-quark can be obtained by performing the substitution $\hat{u} \leftrightarrow \hat{s}$.

The calculation of the matrix elements for the s-channel model is relatively straightforward. The Born matrix element corresponding to the left Feynman diagram of Fig. 7.2 reads:

$$\mathcal{M}^s_{Born} = -\frac{1}{\hat{t} - M_V^2}\left[g_q^V g_\chi^V \left(\bar{\chi}\gamma^\mu\chi\right)\left(\bar{q}\gamma_\mu q\right) + g_q^A g_\chi^A \left(\bar{\chi}\gamma^\mu\gamma_5\chi\right)\left(\bar{q}\gamma_\mu\gamma_5 q\right)\right], \tag{7.11}$$

where in the non-relativistic limit we have $\hat{t} \ll M_V^2$ and the dependence from this Mandelstam variable can therefore be safely neglected. The couplings g_i^j have been defined in the Lagrangian of the s-channel model in Eq. (3.24) and M_V is the mass of the vector mediator. In the t-channel model, a slight complication is given by the ordering of the fermionic fields, which complicates the matching of the matrix elements to the EFT operators. The Born matrix element corresponding to the right Feynman diagram of Fig. 7.2 is equal to:

$$\mathcal{M}^t_{Born} = -\left[\frac{\lambda^2_{Q_L}}{\hat{u} - M_L^2}\left(\chi\bar{P}_L q\right)\left(\bar{q}P_R\chi\right) + \frac{\lambda^2_{q_R}}{\hat{u} - M_R^2}\left(\chi\bar{P}_R q\right)\left(\bar{q}P_L\chi\right)\right], \tag{7.12}$$

where the couplings have been defined in the Lagrangian of the t-channel model in Eq. (3.25) and the masses M_L and M_R are, respectively, the masses of the left- and right-handed scalar mediators. The chirality projectors P_L and P_R are equal to:

$$P_L = \frac{\mathbb{1} - \gamma_5}{2}, \qquad P_R = \frac{\mathbb{1} + \gamma_5}{2}. \tag{7.13}$$

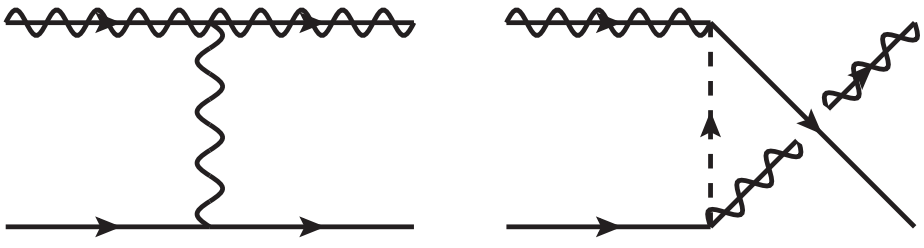

Figure 7.2: Tree-level Feynman diagrams for DM-quark scattering in the s-channel (left) and t-channel (right) models.

As already mentioned, the fermion fields in this matrix element are not ordered as they are in the effective Lagrangian of Eq. (7.4). In order to derive the Wilson coefficients, a rearrangement of the spinors is necessary. This rearrangement can be performed using the so-called Fierz identities, which have first been developed by Markus Fierz in 1932 [173]. The explicit expressions of the identities can be found in [174]. The expressions are simplified in our case because, since we work in the non-relativistic limit, mixed Dirac structures and pseudosalar contributions can be neglected. This means that the relevant identities are:

$$(\bar{\chi}q)(\bar{q}\chi) = -\frac{1}{4}\Big\{(\bar{\chi}\chi)(\bar{q}q) + (\bar{\chi}\gamma_\mu\chi)(\bar{q}\gamma^\mu q) + \frac{1}{2}(\bar{\chi}\sigma_{\mu\nu}\chi)(\bar{q}\sigma^{\mu\nu}q) - (\bar{\chi}\gamma_\mu\gamma_5\chi)(\bar{q}\gamma^\mu\gamma_5 q)\Big\}, \tag{7.14}$$

$$(\bar{\chi}\gamma_5 q)(\bar{q}\gamma_5\chi) = -\frac{1}{4}\Big\{(\bar{\chi}\chi)(\bar{q}q) - (\bar{\chi}\gamma_\mu\chi)(\bar{q}\gamma^\mu q) + \frac{1}{2}(\bar{\chi}\sigma_{\mu\nu}\chi)(\bar{q}\sigma^{\mu\nu}q) + (\bar{\chi}\gamma_\mu\gamma_5\chi)(\bar{q}\gamma^\mu\gamma_5 q)\Big\}, \tag{7.15}$$

$$(\bar{\chi}\gamma_\mu q)(\bar{q}\gamma^\mu\chi) = -(\bar{\chi}\chi)(\bar{q}q) + \frac{1}{2}(\bar{\chi}\gamma_\mu\chi)(\bar{q}\gamma^\mu q) + \frac{1}{2}(\bar{\chi}\gamma_\mu\gamma_5\chi)(\bar{q}\gamma^\mu\gamma_5 q), \tag{7.16}$$

$$(\bar{\chi}\gamma_\mu\gamma_5 q)(\bar{q}\gamma^\mu\gamma_5\chi) = (\bar{\chi}\chi)(\bar{q}q) + \frac{1}{2}(\bar{\chi}\gamma_\mu\chi)(\bar{q}\gamma^\mu q) + \frac{1}{2}(\bar{\chi}\gamma_\mu\gamma_5\chi)(\bar{q}\gamma^\mu\gamma_5 q). \tag{7.17}$$

These expressions can be combined to obtain the Fierz identities for structures containing the chirality projectors P_L and P_R.

Since our goal is to obtain NLO results, the next step is to calculate radiative corrections for both models. Considering that we are not in a high-energy regime, we have to follow a slightly different procedure from the one described in Sec. 4.2.

7.3 Radiative corrections

A major difference between a full NLO-QCD calculation and the one we are performing in the non-relativistic limit is that in this case the calculation of real-emission corrections is not necessary. In this limit, in fact, the in- and outgoing momenta of the same particles are equal, and therefore there is no possibility of having a parton emission[1]. This means that only virtual corrections have to be calculated. In this case, they are IR finite on their own, which we have checked explicitly, and no subtraction method for IR divergences is required. Representative diagrams for these virtual corrections are shown in Fig. 7.3.

To deal with the UV divergences present in the virtual corrections, we are using dimensional regularisation with $d = 4 - 2\varepsilon$ and anti-commutation relations between the gamma matrices and γ_5. After having regularised the divergences, we remove them using the hybrid on-shell/$\overline{\text{MS}}$ renormalisation scheme of Sec. 4.3.2. The on-shell scheme is used for the quark field-strenght renormalisation and the $\overline{\text{MS}}$ scheme is used for the renormalisation of couplings and mediator masses.

The corrections we are discussing here all contribute at $\mathcal{O}(\alpha_s)$. Other contributions from loop-induced processes with gluons in initial and final states contributing to DM-nucleon scattering have been calculated in the framework of the MSSM and similar models in [175–179]. However, these contributions contribute only starting from $\mathcal{O}(\alpha_s^2)$ to the cross sections, which is one order higher than what we are discussing in our work, and we are thus not taking them into account.

[1] To be more accurate, the real emissions limited to very soft energies cancel out exactly in the elastic approximation.

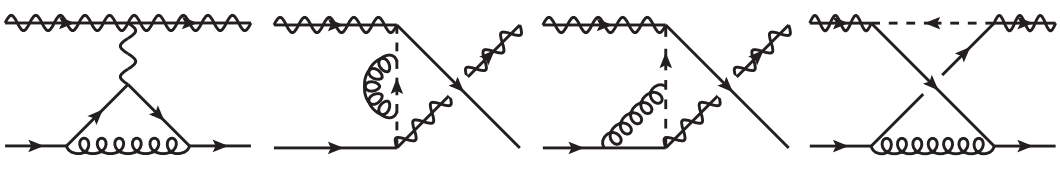

Figure 7.3: Representative one-loop Feynman diagrams for DM-quark scattering, for the s-channel (a) and t-channel [(b)–(d)] models.

7.4 Matching of simplified models and effective field theory

Having calculated the matrix elements for the simplified models, we can finally obtain the Wilson coefficients by performing the so-called *matching* procedure. This consists of imposing, at each order in perturbation theory,

$$\mathcal{M}_{\text{sim}} \stackrel{!}{=} \mathcal{M}_{EFT}, \tag{7.18}$$

where the two amplitudes have been calculated in their respective frameworks, i.e. $\mathcal{M}_{\text{sim}}$ in the simplified models and $\mathcal{M}_{\text{EFT}}$ in the EFT approach. Therefore, the left-hand side (l.h.s) of Eq. (7.18) will depend on the parameters of the simplified models, while the right-hand side (r.h.s.) is a function of the Wilson coefficients. Imposing this equality, we will be able to express the Wilson coefficients in terms of the parameters of the simplified model.

Looking at the EFT Lagrangian of Eq. (7.4), the matching condition at LO reads simply:

$$\mathcal{M}_{\text{sim}}^{\text{tree}} \stackrel{!}{=} c_S^{\text{tree}}\,\mathcal{O}_S^{\text{tree}} + c_V^{\text{tree}}\,\mathcal{O}_V^{\text{tree}} + c_A^{tree}\,\mathcal{O}_A^{\text{tree}} + c_T^{\text{tree}}\,\mathcal{O}_T^{\text{tree}}. \tag{7.19}$$

The expressions for the tree level matrix elements for both models have been derived in Eqs. (7.11) and (7.12). Noticing which Lorentz structures are present in those equations, it can be seen that the only Wilson coefficients contributing at tree level are the vector and axial-vector ones, i.e. c_V^{tree} and c_A^{tree}. This is straightforward in the s-channel model, but requires using the Fierz identities for the fermion chains in the t-channel model. The tree-level matching condition is therefore even more compact in our case:

$$\mathcal{M}_{\text{sim}}^{\text{tree}} \stackrel{!}{=} c_V^{\text{tree}}\,\mathcal{O}_V^{\text{tree}} + c_A^{\text{tree}}\,\mathcal{O}_A^{\text{tree}}. \tag{7.20}$$

The matching condition at NLO has the following form:

$$\mathcal{M}_{\text{sim}}^{\text{NLO}} \stackrel{!}{=} \sum_{j=S,V,A,T} c_j^{\text{NLO}}\mathcal{O}_j^{\text{NLO}}, \tag{7.21}$$

where it is important to note that the effective operators are subject to NLO corrections as well as the Wilson coefficients. Both the matrix elements of the simplified models and the terms on the r.h.s. of this equation can be decomposed into tree-level and one-loop terms:

$$\mathcal{M}_{\text{sim}}^{\text{NLO}} = \mathcal{M}_{\text{sim}}^{\text{tree}} + \mathcal{M}_{\text{sim}}^{\text{1-loop}}, \tag{7.22}$$

$$c_j^{\text{NLO}}\mathcal{O}_j^{\text{NLO}} = \left(c_j^{\text{tree}} + c_j^{\text{1-loop}}\right)\left(\mathcal{O}_j^{\text{tree}} + \mathcal{O}_j^{\text{1-loop}}\right), \tag{7.23}$$

with $\mathcal{M}_{\text{sim}}^{\text{1-loop}}$, $c_j^{\text{1-loop}}$ and $\mathcal{O}_j^{\text{1-loop}}$ of $\mathcal{O}(\alpha_{\text{s}})$. Terms of the kind $c_j^{\text{1-loop}}\mathcal{O}_j^{\text{1-loop}}$ will not be addressed in our calculation since they contribute at $\mathcal{O}(\alpha_{\text{s}}^2)$. Considering that for the

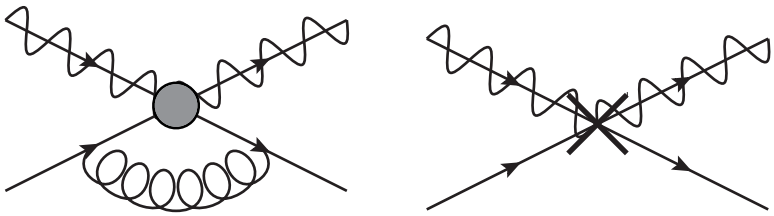

Figure 7.4: One-loop Feynman diagrams for DM-quark scattering in the EFT (left) and the corresponding counterterm diagram (right).

LO coefficients we have $c_S^{\text{tree}} = c_T^{\text{tree}} = 0$ and canceling the LO contributions on both sides of Eq. (7.21) using Eq. (7.20), we can write the NLO matching condition in a more compact way as:

$$\begin{aligned}\mathcal{M}_{\text{sim}}^{\text{1-loop}} - c_A^{\text{tree}}\mathcal{O}_A^{\text{1-loop}} - c_V^{\text{tree}}\mathcal{O}_V^{\text{1-loop}} &\stackrel{!}{=} \\ c_S^{\text{1-loop}}\mathcal{O}_S^{\text{tree}} + c_A^{\text{1-loop}}\mathcal{O}_A^{\text{tree}} + c_V^{\text{1-loop}}\mathcal{O}_V^{\text{tree}} + c_T^{\text{1-loop}}\mathcal{O}_T^{\text{tree}}&\,.\end{aligned} \tag{7.24}$$

Therefore, to calculate the one-loop Wilson coefficients, it is not sufficient to calculate the one-loop simplified model matrix elements, but operator corrections have to be considered as well. Since the corresponding tree-level Wilson coefficients vanish, we do not have to calculate operator corrections to the scalar and tensor operators, which, in the NLO matching procedure, only contribute to the terms $c_{S,T}^{tree}\mathcal{O}_{S,T}^{\text{1-loop}}$. However, we stress that they might not necessarily vanish on their own and only the sum of their contributions vanish as a result of the NLO matching procedure.

We note that the simplified model is valid at a high-energy scale, which we choose to be $\mu_{\text{high}} = M_{\text{med}}$, and thus the matching, demanding the EFT to reproduce the full theory, is to be performed at this scale. As the nucleonic matrix elements are, however, defined at a low-energy scale $\mu_{\text{low}} \sim 2$ GeV, the Wilson coefficients $c_{j,q}$ consequently have to be evolved from μ_{high} down to μ_{low} via renormalisation-group equations.

Before extracting the various contributions to the Wilson coefficients for both simplified models from the various virtual diagrams, we will show the relevant operator corrections. There is only one vertex correction plus a corresponding counterterm contributing to each one-loop operator correction in the EFT, which are represented in Fig. 7.4. In the non-relativistic limit, these one-loop terms are proportional to the corresponding tree-level operators,

$$\mathcal{O}_j^{\text{1-loop}} = \frac{\alpha_{\text{s}}}{4\pi} C_F\, o_j^{\text{1-loop}} \mathcal{O}_j^{\text{tree}}\,, \tag{7.25}$$

with

$$o_j^{\text{1-loop}} = o_{j,\triangle}^{\text{1-loop}} + o_{j,\text{CT}}^{\text{1-loop}} \tag{7.26}$$

for each tensor structure $j = S, V, A, T$, parameterizing the full one-loop correction with the colour factor $C_F = \frac{4}{3}$ explicitly factored out.

For the vector and axial-vector operators, the expressions for the operator corrections are identical to the one-loop Wilson coefficients in the s-channel model, which will be calculated in the following section and that we momentarily define simply as $c_{j,\triangle}^{s,\text{1-loop}}$, where $j = V, A$. The explicit expression is given in Eq. (7.31). For the vertex correction to the operators we can therefore write:

$$\begin{aligned} o_{V,\triangle}^{\text{1-loop}} &= c_{V,\triangle}^{s,\text{1-loop}}\,, \\ o_{A,\triangle}^{\text{1-loop}} &= c_{A,\triangle}^{s,\text{1-loop}}\,. \end{aligned} \tag{7.27}$$

For the counterterms we also get an expression identical to the one-loop counterterm in the s-channel model. We momentarily define them as $c_{j,\mathrm{CT}}^{s,\text{1-loop}}$, with the explicit expression given in Eq. (7.32) and write the results as:

$$\begin{aligned} o_{V,\mathrm{CT}}^{\text{1-loop}} &= c_{V,\mathrm{CT}}^{s,\text{1-loop}}\,, \\ o_{A,\mathrm{CT}}^{\text{1-loop}} &= c_{A,\mathrm{CT}}^{s,\text{1-loop}}\,. \end{aligned} \tag{7.28}$$

Summing the contributions to obtain the full one-loop operator correction as in Eq. (7.26), and using the explicit expressions for these terms, we see that the corrections vanish for the vector operator, and lead to a finite contribution for the axial-vector operator:

$$\begin{aligned} o_{V}^{\text{1-loop}} &= 0\,, \\ o_{A}^{\text{1-loop}} &= -2\,. \end{aligned} \tag{7.29}$$

We can now calculate the contributions to the Wilson coefficients for the s- and t-channel simplified model, which arise from the matrix elements corresponding to the diagrams of Fig. 7.3. We will also calculate the Wilson coefficients for a combined $s+t$-channel simplified model, in which both mediators are present simultaneously.

We now list all expressions that are required to calculate the $\mathcal{O}(\alpha_\mathrm{s})$ contributions to the Wilson coefficients. For clarity, we separate the contributions according to the type of mediator-fermion interaction $j = S, V, A, T$ and the topology of the one-loop diagrams by introducing labels for propagator ($\circ$), vertex ($\triangle$), and box corrections ($\square$) as well as counterterm contributions (CT). For symbolic manipulations, we have used the MATHEMATICA packages FEYNCALC [180–182] and PACKAGE-X [183].

7.4.1 Wilson coefficients of the s-channel simplified model

In the s-channel model, the only tensor structures appearing in the tree-level matrix elements that contribute to DM-quark scattering are the ones corresponding to the vector and axial-vector currents. Imposing the matching condition leads to the following Wilson coefficients:

$$\begin{aligned} c_{S}^{s,\text{tree}} &= 0\,, \\ c_{V}^{s,\text{tree}} &= -\frac{g_q^V g_\chi^V}{M_V^2}\,, \\ c_{A}^{s,\text{tree}} &= -\frac{g_q^A g_\chi^A}{M_V^2}\,, \\ c_{T}^{s,\text{tree}} &= 0\,. \end{aligned} \tag{7.30}$$

At the one-loop level, there are only contributions originating from corrections to the quark-antiquark-mediator vertex, since the mediator does not carry a colour charge. The relevant corrections are of the form

$$\begin{aligned} c_{S,\triangle}^{s,\text{1-loop}} &= 0\,, \\ c_{V,\triangle}^{s,\text{1-loop}} &= 3\left(\Delta + \ln\frac{\mu_\mathrm{R}^2}{m_q^2}\right) + 4\,, \\ c_{A,\triangle}^{s,\text{1-loop}} &= c_{V,\triangle}^{s,\text{1-loop}} - 2\,, \\ c_{T,\triangle}^{s,\text{1-loop}} &= 0\,, \end{aligned} \tag{7.31}$$

with $\Delta = \frac{1}{\varepsilon} - \gamma_{\rm E} + \ln(4\pi)$, where $\gamma_{\rm E}$ is the Euler–Mascheroni constant $\gamma_{\rm E} \approx 0.57721$. Note that here and in the following, the $1/\varepsilon$ term generally receives contributions both from UV and IR divergences. It turns out that the counterterm contributions are the same for both the vector and axial-vector currents, and furthermore they are exactly opposite to the corrections of the vector current:

$$\begin{aligned} c_{S,\rm CT}^{s,\text{1-loop}} &= 0\,, \\ c_{V,\rm CT}^{s,\text{1-loop}} &= -c_{V,\triangle}^{s,\text{1-loop}}\,, \\ c_{A,\rm CT}^{s,\text{1-loop}} &= c_{V,\rm CT}^{s,\text{1-loop}}\,, \\ c_{T,\rm CT}^{s,\text{1-loop}} &= 0\,. \end{aligned} \tag{7.32}$$

We can already see at this point that there is no correction to the vector current.

After summing all the one-loop contributions, we finally need to take into account the one-loop operator corrections as dictated by the matching condition of Eq. (7.24). Since, as we anticipated, the corrections to the vector and axial-vector operators are equivalent to the ones in the s-channel model, they cancel each other, and at $\mathcal{O}(\alpha_{\rm s})$ we find no contributions to the Wilson coefficients of the discussed operators for this model,

$$c_j^{s,\text{1-loop}} = \frac{\alpha_{\rm s}}{4\pi} C_F \left(c_{j,\triangle}^{s,\text{1-loop}} + c_{j,\rm CT}^{s,\text{1-loop}} - o_j^{\text{1-loop}} \right) c_j^{s,\text{tree}} = 0\,, \tag{7.33}$$

for all tensor structures $j = S, V, A, T$. We note that, as mentioned before, while the sum of the vertex correction and counterterm contribution to the vector current cancels independently of the matching, the corresponding contribution to the axial-vector current is non-zero and vanishes only after including the operator correction.

7.4.2 Wilson coefficients to the t-channel simplified model

Also in the t-channel model, only the vector and axial-vector operators contribute at tree level. In our calculation we will assume that the t-channel mediators only couple to left-handed squark. We will keep this approximation in our analysis in Sec.7.5, where we will also motivate our choice more in detail. In our results we will therefore only include the coupling $\lambda_{Q_L}^2$ and indicate with $M_{\tilde{Q}}$ the mass of the left-handed mediator. A transition to the general case is obtained by replacing in all the following results $\lambda_{Q_L}^2$ by a sum of the allowed couplings and differentiating between the masses M_L and M_R.

From the tree-level matching condition, we obtain the following Wilson coefficients:

$$\begin{aligned} c_S^{t,\text{tree}} &= 0\,, \\ c_V^{t,\text{tree}} &= \frac{\lambda_{Q_L}^2}{8\left(\hat{u} - M_{\tilde{Q}}^2\right)} := c^{t,\text{tree}}\,, \\ c_A^{t,\text{tree}} &= -c^{t,\text{tree}}\,, \\ c_T^{t,\text{tree}} &= 0\,. \end{aligned} \tag{7.34}$$

Here we have introduced a common tree-level factor, $c^{t,\text{tree}}$, which will also appear in the one-loop expressions for each tensor structure.

At $\mathcal{O}(\alpha_{\rm s})$, we now have several contributions coming from propagator, vertex, and box corrections. We write these contributions in terms of scalar and tensor integrals and use the MATHEMATICA extension PACKAGE-X to obtain analytical expressions for

the loop integrals. All one-loop integrals emerging in our calculation can be expressed in terms of a small set of master integrals that below we abbreviate as

$$\begin{aligned} A_0 &= A_0(m_\chi^2)\,, \\ B_0 &= B_0(\hat{u}; 0, M_{\tilde{Q}}^2)\,, \\ C_i &= C_i(m_q^2, m_\chi^2, \hat{u}; 0, m_q^2, M_{\tilde{Q}}^2)\,, \\ D_{i,ij} &= D_{i,ij}(m_q^2, m_\chi^2, m_\chi^2, m_q^2, \hat{u}, 0; 0, m_q^2, M_{\tilde{Q}}^2, m_q^2)\,, \end{aligned}$$

where we are following the notation of Ref. [183]. For the three-point integrals, we encounter C_i with $i = 0, 1, 2$, while in the case of four-point integrals, those of type D_i and D_{ij} with $i, j = 0, 1, 2, 3$ emerge.

The contributions from the propagator correction can then be written as:

$$\begin{aligned} c_{S,\circ}^{t,\text{1-loop}} &= 0\,, \\ c_{V,\circ}^{t,\text{1-loop}} &= \frac{2\left(\hat{u} + M_{\tilde{Q}}^2\right) B_0 - A_0}{\hat{u} - M_{\tilde{Q}}^2}\,, \\ c_{A,\circ}^{t,\text{1-loop}} &= -c_{V,\circ}^{t,\text{1-loop}}\,, \\ c_{T,\circ}^{t,\text{1-loop}} &= 0\,. \end{aligned} \tag{7.35}$$

The contributions from the vertex corrections are:

$$\begin{aligned} c_{S,\triangle}^{t,\text{1-loop}} &= 4 m_q m_\chi C_1\,, \\ c_{V,\triangle}^{t,\text{1-loop}} &= 2\Big[B_0 + 2\left(\hat{u} - m_\chi^2\right)(C_0 + C_1 + C_2) \\ &\qquad + 2\left(m_q^2 C_0 + m_\chi^2 C_2\right)\Big]\,, \\ c_{A,\triangle}^{t,\text{1-loop}} &= -c_{V,\triangle}^{t,\text{1-loop}}\,, \\ c_{T,\triangle}^{t,\text{1-loop}} &= -c_{S,\triangle}^{t,\text{1-loop}}\,. \end{aligned} \tag{7.36}$$

The contributions from the box correction are:

$$\begin{aligned} c_{S,\square}^{t,\text{1-loop}} &= 4 m_q m_\chi \left(\hat{u} - M_{\tilde{Q}}^2\right)(D_{12} + D_{22} + D_{23} - D_2)\,, \\ c_{V,\square}^{t,\text{1-loop}} &= 2\left(\hat{u} - M_{\tilde{Q}}^2\right)\Big\{2D_{00} - m_\chi^2 D_{22} - m_q^2[D_{11} + D_{22} \\ &\qquad + D_{33} - 2(D_0 + D_1 + D_2 + D_3 \\ &\qquad - D_{12} - D_{13} - D_{23})]\Big\}\,, \\ c_{A,\square}^{t,\text{1-loop}} &= -2\left(\hat{u} - M_{\tilde{Q}}^2\right)\Big\{2D_{00} + m_\chi^2 D_{22} + m_q^2[D_{11} + D_{22} \\ &\qquad + D_{33} + 2(D_0 + D_1 + D_2 + D_3 \\ &\qquad + D_{12} + D_{13} + D_{23})]\Big\}\,, \\ c_{T,\square}^{t,\text{1-loop}} &= 4 m_q m_\chi \left(\hat{u} - M_{\tilde{Q}}^2\right)(D_{12} + D_{22} + D_{23} + D_2)\,. \end{aligned} \tag{7.37}$$

We also list the counterterm contributions which we have calculated from the renor-

malisation constants of our model:

$$\begin{aligned} c_{S,\mathrm{CT}}^{t,\text{1-loop}} &= 0\,, \\ c_{V,\mathrm{CT}}^{t,\text{1-loop}} &= -\left[\Delta\left(\frac{2\hat{u}+M_{\tilde{Q}}^2}{\hat{u}-M_{\tilde{Q}}^2}+4\right)+3\ln\frac{\mu_{\mathrm{R}}^2}{m_q^2}+4\right], \\ c_{A,\mathrm{CT}}^{t,\text{1-loop}} &= -c_{V,\mathrm{CT}}^{t,\text{1-loop}}\,, \\ c_{T,\mathrm{CT}}^{t,\text{1-loop}} &= 0\,. \end{aligned} \tag{7.38}$$

Eventually, we sum over all the one-loop contributions and multiply by the common factor mentioned above. Additionally, we need to take into account the one-loop operator corrections as dictated by the matching condition to obtain the $\mathcal{O}(\alpha_{\mathrm{s}})$ corrections to the Wilson coefficients of the t-channel model:

$$\begin{aligned} c_j^{t,\text{1-loop}} = \frac{\alpha_{\mathrm{s}}}{4\pi}C_F\Big(&c_{j,\circ}^{t,\text{1-loop}}+c_{j,\triangle}^{t,\text{1-loop}}+c_{j,\square}^{t,\text{1-loop}}+c_{j,\mathrm{CT}}^{t,\text{1-loop}} \\ &-o_j^{\text{1-loop}}\Big)c^{t,\text{tree}}\,, \end{aligned} \tag{7.39}$$

for each tensor structure $j = S, V, A, T$.

An interesting feature of the t-channel model is that at tree level only the Wilson coefficients of the vector and axial-vector operators, c_V and c_A, contribute. Genuine contributions to the scalar and tensor coefficients, c_S and c_T, are obtained only starting at order $\mathcal{O}(\alpha_s)$. However, we have examined the numerical effects of all Wilson coefficients and found that, compared to the dominant Wilson coefficients, the contribution of c_S and c_T to the full NLO cross section is small: it is less than 0.1% in most cases, and in the range of 0.1% up to approximately 1% for low DM masses and when being close to the threshold of equal DM and mediator masses.

7.4.3 Wilson coefficients to the $s+t$-channel simplified model

For the $s+t$-channel model, corresponding to the sum of the Lagrangians of Eq. (3.24) and Eq. (3.25), the tree-level and one-loop Wilson coefficients can be readily obtained by summing the contributions of the s- and t-channel models quoted above. In particular, this means that at the one-loop level, we must add the vertex and counterterm contributions of Eq. (7.31) and Eq. (7.32) to the one-loop Wilson coefficient of the t-channel model, Eq. (7.39), so that the one-loop operator correction is taken into account only once. We find

$$\begin{aligned} c_j^{s+t,\text{tree}} &= c_j^{s,\text{tree}}+c_j^{t,\text{tree}}\,, \\ c_j^{s+t,\text{1-loop}} &= \frac{\alpha_{\mathrm{s}}}{4\pi}C_F\left(c_{j,\triangle}^{s,\text{1-loop}}+c_{j,\mathrm{CT}}^{s,\text{1-loop}}\right)c_j^{s,\text{tree}}+c_j^{t,\text{1-loop}}\,, \end{aligned} \tag{7.40}$$

for each tensor structure $j = S, V, A, T$. Since the only relevant one-loop corrections in the s-channel model either vanish exactly (for the vector operator) or cancel with the corresponding operator corrections (for the axial-vector operator), we can write the one-loop Wilson coefficient also as:

$$\begin{aligned} c_j^{s+t,\text{1-loop}} = \frac{\alpha_{\mathrm{s}}}{4\pi}C_F\Big(&c_{j,\circ}^{t,\text{1-loop}}+c_{j,\triangle}^{t,\text{1-loop}}+c_{j,\square}^{t,\text{1-loop}} \\ &+c_{j,\mathrm{CT}}^{t,\text{1-loop}}\Big)c^{t,\text{tree}}\,, \end{aligned} \tag{7.41}$$

which corresponds to Eq. (7.39) without the operator correction.

7.5 Numerical analysis

We now present numerical results for the SI and SD DM-nucleon scattering cross sections, and discuss the effects of the $\mathcal{O}(\alpha_s)$ corrections. Furthermore, we assess the potential of various direct detection experiments to explore regions in their respective parameter spaces when confronted with limits of LHC searches for DM production. As the numerical difference between the proton and neutron contribution to the SI cross section is marginal and the direct detection experiments typically publish limits irrespective of the nature of the nucleon, we limit ourselves to showing only the DM-proton cross sections for SI interactions. On the other hand, since the sensitivities of the experiments for the SD interaction differ between proton and neutron scattering, and the CRESST collaboration has only published limits for neutron scattering, we will focus on the DM-neutron cross sections in the case of SD interactions.

In the following, we do not discuss the pure s-channel model with a vector mediator further since, as we discussed, the $\mathcal{O}(\alpha_s)$ corrections vanish for such a scenario. The impact of s-channel contributions is only considered in the context of interference effects in models that feature s- and t-channel topologies at the same time.

For the t-channel model, we assume the DM particle to be a Dirac fermion. We choose a scenario where all right-handed couplings are turned off, i.e. $\lambda_{u_R} = \lambda_{d_R} = 0$ for all quark flavours, and the mediators thus only couple to the left-handed $\mathrm{SU}(2)_L$ quark doublets. This choice is motivated by the most recent mono-jet searches of the ATLAS experiment [95], where limits are presented for the same selection of couplings. In the following, we use the short-hand notation $\lambda \equiv \lambda_{Q_L}$, and assume the mediators to couple to all left-handed quark doublets with equal strength. Unless explicitly specified otherwise, we choose $\lambda = 1$.

All quarks in our calculations are assumed to be massive and we use for the quark masses the current values compiled by the particle data group [184]. However, as in our models the dominant contributions for the SI and SD scattering processes stem from the vector and axial-vector operators, which receive non-vanishing contributions only from the light u, d, and s quark flavours, the numerical effects of the light quark masses are negligibly small. For the nuclear matrix elements we use the numerical values quoted in Tab. 7.1.

We use the world average for the strong coupling evaluated at the mass of the Z boson, $\alpha_s(M_Z) = 0.1179$ [184], as an input value for determining the value of $\alpha_s(\mu_R)$ at a value of the renormalisation scale μ_R representative for the considered class of reactions via NLO-QCD running of the renormalisation group equation. Since DM scattering reactions at direct detection experiments typically occur at rather low scales, we choose $\mu_R = 2$ GeV as our default value and discuss uncertainties arising from a variation of μ_R by a factor of two around the default value, leading to a variation of the value of α_s in the range from 0.226 to 0.443. We note that for such low scales, the strong coupling assumes rather large values, in particular $\alpha_s(\mu_R = 1\ \mathrm{GeV}) = 0.443$. Thus, contrary to the situation at high-energy colliders such as the LHC, perturbative calculations in the context of direct detection experiments have to be interpreted with caution, and the potential uncertainties associated with perturbative predictions have to be carefully assessed.

Let us briefly comment on the dependence of the NLO SI and SD cross sections on the renormalisation scale μ_R. Because of the particular structure of the reactions we consider in the framework of our simplified models, $\alpha_s(\mu_R)$ enters first in the NLO-QCD corrections, while the hard parts of the LO cross sections are independent of α_s and of μ_R. Schematically, the perturbative expansion of these cross sections, generically

denoted by σ, is of the form

$$\sigma = \sigma^{(0)} + \alpha_s(\mu_R)\sigma^{(1)}(\mu_R) + \mathcal{O}(\alpha_s^2)\,, \tag{7.42}$$

with all dependence on α_s explicitly factored out of the expansion coefficients $\sigma^{(i)}$. Varying μ_R thus affects both, the value of α_s, and the size of the NLO correction term $\sigma^{(1)}$ which depends explicitly on the logarithms of the renormalisation scale. In the following discussion of our results, we will study the effects of varying the renormalisation scale.

The above discussion does not yet include any renormalisation group running of the effective operators and, consequently, of the Wilson coefficients. As discussed in the previous section, the Wilson coefficients, having been determined at a high scale μ_{high}, have to be evolved down to the scale μ_{low} at which the nucleonic matrix elements are evaluated. Then, as the running effects in the product of Wilson coefficient and nucleonic matrix element are inversely proportional and therefore cancel, the identification of μ_{low} with the value of the renormalisation scale μ_R and a subsequent variation of μ_R will not lead to an additional source of scale uncertainty. In principle, μ_{high} could also be varied, leading to an additional uncertainty related to the renormalisation-group running of the Wilson coefficients. We have checked that the effect of this variation is small compared to the other scale uncertainties in our work and we therefore do not discuss it further. We take into account the running effects of the operators appearing in our models including the effects of the resummation of QCD logarithms only, following Ref. [185]. In practice, we find that the running is numerically only relevant for the axial-vector operator, though, for which we apply the two-loop running coefficient: while there are no running effects for the vector operator, the contributions of the scalar and tensor Wilson coefficients are too small for any running effects to be significant.

Using the specified setup, we first discuss the impact of NLO-QCD corrections and scale uncertainties on SI and SD scattering cross sections. After this assessment of the genuine features of experimentally accessible observables we turn to a systematic comparison of limits on DM models from colliders and direct detection experiments in the context of t-channel models. Subsequently, we investigate the impact of interference effects in combined $s + t$-channel models.

7.5.1 Theoretical aspects of the perturbative prediction

Before turning to a phenomenological discussion of the considered DM models, we explore the genuine features and theoretical uncertainties of our perturbative calculation.

In Fig. 7.5 we show the SI and SD DM-nucleon scattering cross sections for the t-channel model as functions of the DM mass for fixed values of the ratio $r = M_{\text{med}}/m_\chi$, together with curves indicating that the entire region of parameter space above is excluded by the CRESST III [28] and XENON1T [29,186] experiments. In contrast to our default assumption of $\lambda = 1$, for this figure we used the MICROMEGAS package to calculate the DM relic abundance and extract, for the given values of m_χ and M_{med}, the value of the coupling λ such that for each point along the curve the model also correctly reproduces the measured DM relic abundance, see Fig. 7.6.

We note that for both, σ_p^{SI} and σ_n^{SD}, the size of the NLO corrections relative to the LO prediction is largest for $r = 1.1$, while it decreases with larger values of r. The difference between the LO and the NLO curves is not covered by the scale dependence of the NLO prediction that is indicated by a red band in the figure. For $r = 1.1$, meaningful values for the cross sections are obtained only for DM masses above ~ 200 GeV. Below that range there are no configurations with a value of λ being compatible with

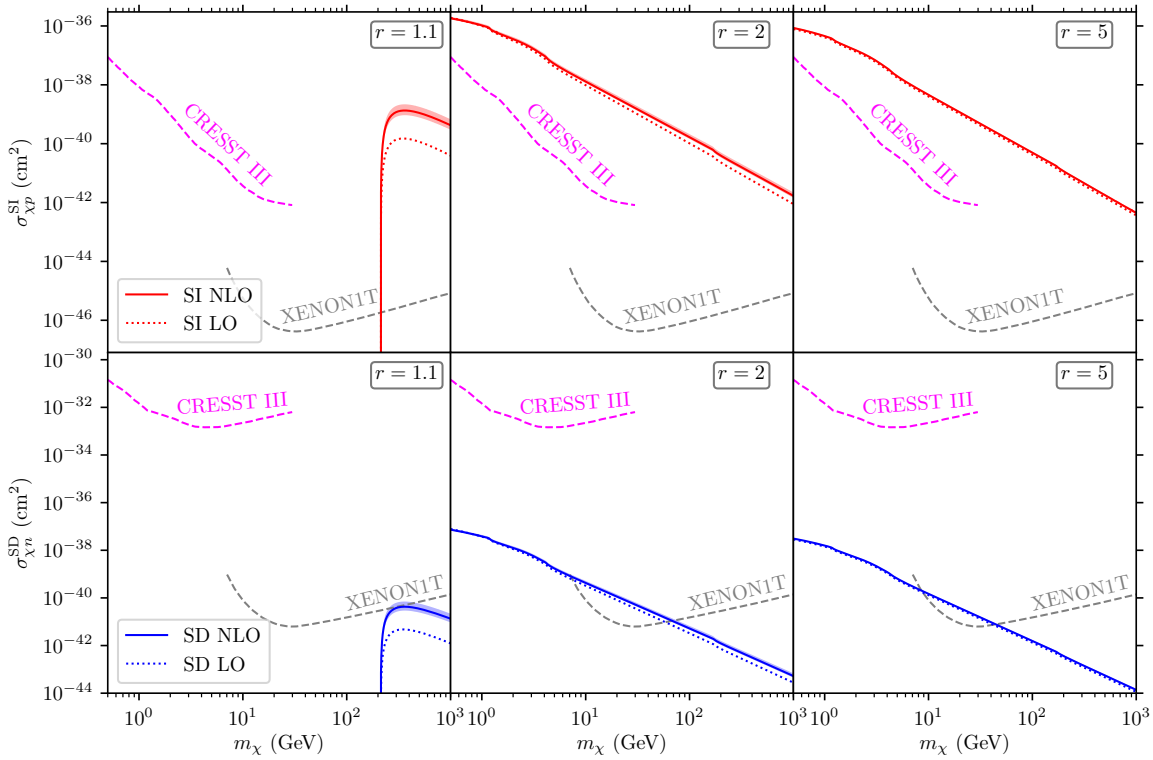

Figure 7.5: SI DM-proton (top) and SD DM-neutron (bottom) scattering cross sections for the t-channel model for given values of $r = M_{\text{med}}/m_\chi$ at LO (dotted) and NLO (solid), with bands indicating their renormalisation scale dependence. Additionally, current exclusion limits from CRESST [28] (dashed magenta) and XENON [29, 186] (dashed grey) are shown. The setting of the coupling λ is discussed in the text.

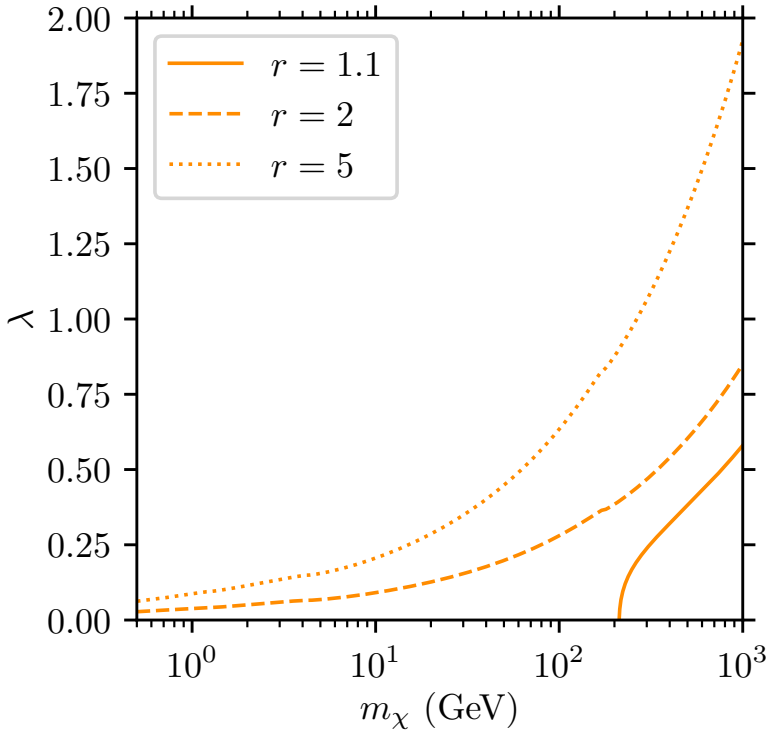

Figure 7.6: Value of the t-channel coupling λ depending on m_χ and $r = M_{\text{med}}/m_\chi$ for which the model correctly predicts the measured DM relic abundance $\Omega_{\text{DM}}h^2 = 0.12$ [184]. For $r = 1.1$ and $m_\chi < 200$ GeV, no phenomenologically viable configurations are found.

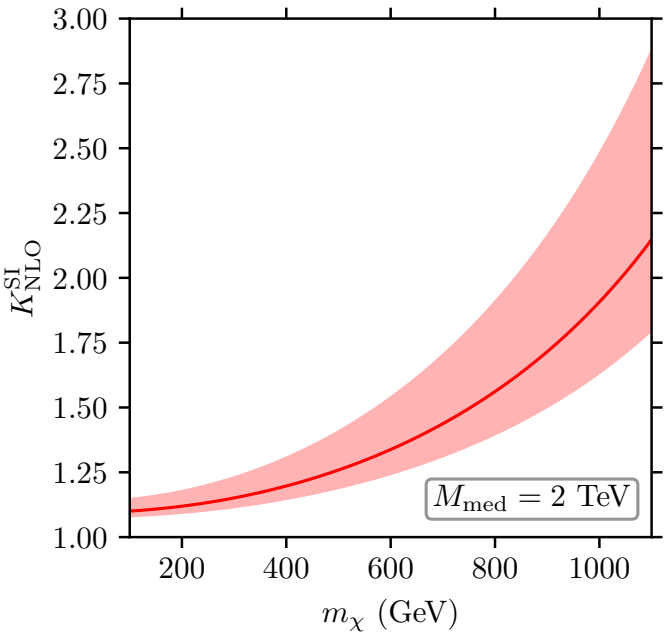

Figure 7.7: K factor for σ_p^{SI} in the t-channel model for a fixed mediator mass $M_{\mathrm{med}} = 2$ TeV, together with bands indicating the renormalisation scale uncertainty. Note that the K factor of σ_n^{SD} is not shown, as it is numerically very similar to the one for σ_p^{SI}, with differences of at most 1-2%.

the measured value of the relic density. This is no longer the case when larger values of r are considered.

Fig. 7.7 depicts the K factor, generally defined as the ratio of a NLO-QCD cross section to the respective LO cross section,

$$K_{\mathrm{NLO}} = \frac{\sigma_{\mathrm{NLO}}}{\sigma_{\mathrm{LO}}}, \tag{7.43}$$

in the spin-independent case, i.e. for σ_p^{SI}, as a function of the DM mass. The value of the coupling λ is now set to 1, and for the renormalisation scale μ_{R} we choose the central value of 2 GeV. The mediator mass M_{med} is fixed to 2 TeV. In order to illustrate the dependence of σ_p^{SI} on μ_{R}, the scale is varied by a factor of two around this central value. The width of the scale uncertainty band clearly indicates the strong dependence of the NLO prediction on this artificial scale. Would one instead consider only the LO approximation, being independent of μ_{R}, an assessment of the perturbative uncertainty of the prediction would not be possible, and uncertainties would be strongly underestimated.

The considered K factor varies from a value of approximately 1.1 for low m_χ to a value in the range of 1.8 to 2.9 beyond $m_\chi = 1$ TeV. It can also be seen that the scale uncertainty grows significantly the closer m_χ is to the threshold $m_\chi = M_{\mathrm{med}}$. Interestingly, we find that the K factor behaves in a nearly identical manner for SI and SD scattering. This feature is due to the similar structure of the NLO corrections for the dominant vector and axial-vector Wilson coefficients.

To analyse the behavior of the K factor for different mediator masses, Fig. 7.8 illustrates instead the size of the NLO corrections depending on m_χ and M_{med} for a fixed renormalisation scale of $\mu_{\mathrm{R}} = 2$ GeV in a two-dimensional colour-coded plot for σ_p^{SI}. As both the LO and the NLO cross sections diverge at the threshold $m_\chi = M_{\mathrm{med}}$, K factors larger than three all correspond to a yellow colour coding. The white region

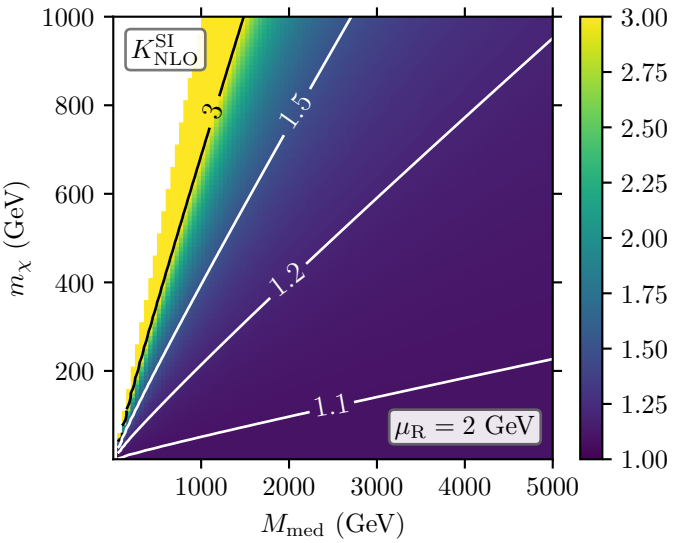

Figure 7.8: K factor for σ_p^{SI} for different values of M_{med} and m_χ with a fixed value of $\mu_{\mathrm{R}} = 2$ GeV.

denotes unphysical parameter points with $m_\chi > M_{\mathrm{med}}$, where the t-channel model does not offer a stable DM candidate. Again, for the same reason as before, we only show the SI case, noting that the SD one looks nearly identical. The K factor ranges from a value close to one at small m_χ and large M_{med} to large values above two for large m_χ and small M_{med}, where, considering the different ranges that we explored, we approach the condition $m_\chi = M_{\mathrm{med}}$. This means that the ratio between the masses is close to one, and the growth of the K factor in this scenario is in agreement with what we observed in Fig. 7.5. As expected from our discussion of Fig. 7.7, we observe a similar behavior for the SI and the SD case.

7.5.2 Comparison of limits from the LHC and direct detection experiments

We now move on to more phenomenological aspects and discuss the effects of the NLO corrections on the comparison between exclusion limits from LHC searches and direct detection experiments. We mentioned some peculiarities of this comparison in Sec. 3.5. As discussed, exclusion limits from collider experiments strongly depend on the studied DM model and they are usually shown in a M_{med}–m_χ parameter plane for a fixed set of coupling parameters, see e.g. [95]. In contrast, direct detection experiments measure the nuclear recoil rate of Eq. (7.1), and the corresponding limits can thus be presented in a model-independent way directly as upper limits on the DM-nucleon scattering cross section, as functions of m_χ. We stress again the different role played by the DM relic abundance in these different DM searches. For collider production of DM, the DM relic abundance is of no relevance. Therefore, in the M_{med}–m_χ plane showing exclusion limits for a specific model, the calculated relic abundance is typically different at each point. In contrast, direct detection experiments measure a scattering rate which depends on the product of the DM-nucleon cross section and the local DM density. Thus, limits from direct detection experiments shown in the DM-nucleon cross section plane assume a fixed relic abundance. When comparing LHC limits to excluded regions from direct detection experiments, these implicit assumptions on the relic abundance have to be taken into account.

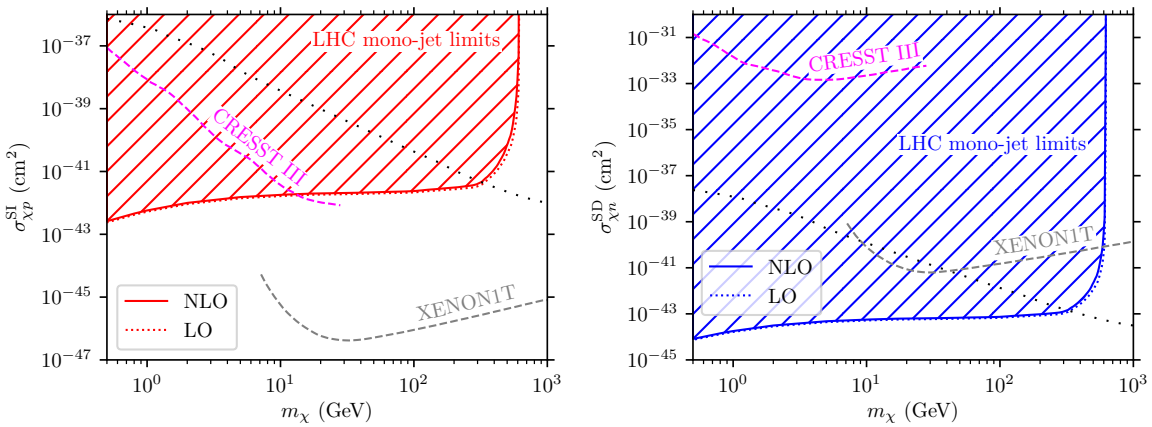

Figure 7.9: Exclusion limits (hatched areas) for $\sigma_p^{\rm SI}$ (left) and $\sigma_n^{\rm SD}$ (right), extracted from ATLAS [95] data at LO and NLO-QCD, and from the CRESST [28] and XENON [29, 186] experiments for the t-channel model, see text for details. Parameter points on the black dotted lines are compatible with the measured relic abundance, the areas above (below) correspond to an under-abundance (over-abundance).

The transformation of LHC limits which are given as points in the $(m_\chi, M_{\rm med}, \lambda)$ parameter space into limits on DM-nucleon cross sections simply amounts to calculating the SI and SD cross sections for parameter points excluded by the LHC. Thus, the limits will be affected by whether LO or NLO expressions for the cross sections are used. For the translation of published LHC limits into the $\sigma_{p/n}^{\rm SI/SD} - m_\chi$ plane we follow the recommendation of Ref. [96]. Another feature of the LHC limits is that, as parameter regions of the t-channel model up to the threshold $m_\chi = M_{\rm med}$ are probed, there is a sharp cutoff for the highest excluded value of m_χ.

In Fig. 7.9 we present exclusion limits for the DM-nucleon scattering cross sections $\sigma_p^{\rm SI}$ and $\sigma_n^{\rm SD}$ at LO and NLO accuracy as derived from ATLAS [95], together with exclusion limits provided by the CRESST III [28] and XENON1T [29,186] experiments. Numbers are obtained in the context of the t-channel model of Eq. (3.25) with its coupling parameter set to $\lambda = 1$. Additionally, we indicate the compatibility of points in the considered parameter space with the measured relic abundance. In the plots, LHC searches for mono-jets as tell-tale signatures of a DM production process yield the hatched red and blue exclusion regions in the two-dimensional plots. Including NLO-QCD corrections slightly reduces the excluded area as compared to the LO estimate for our default scale choice of $\mu_{\rm R} = 2$ GeV. Somewhat larger effects would result for a smaller value of $\mu_{\rm R}$, as apparent from our discussion of the scale dependence of our calculation in Sec. 7.5.1. Direct detection limits of the CRESST and XENON experiments are independent of the perturbative corrections. In particular, CRESST excludes the region above the dashed magenta line, while XENON excludes the entire area above the dashed grey line in the plots. The complementary coverage of the two direct detection experiments comes as no surprise, since CRESST is designed to be particularly sensitive to light DM candidates, while XENON performs best in the domain of larger DM masses. We observe that the considered cross sections diverge for the parameter points of the LHC exclusion limit where the DM mass approaches the mass of the mediator, because of the genuine propagator structure of the scattering amplitude in the t-channel model, $\mathcal{M} \sim 1/(m_\chi^2 - M_{\rm med}^2)$. NLO effects also can be enhanced because of threshold logarithms for $m_\chi \sim M_{\rm med}$. However, generally, the size of the NLO corrections is small, modifying LO results only marginally.

7.5.3 Phenomenology of a combined $s+t$-channel model

Interesting effects can be observed, if instead of the s- or t-channel models a scenario featuring both types of interactions simultaneously is considered. Arguably, such a model could be considered outside of the domain of the more general class of simplified models, and we discuss it in our work as an example of a more complex DM model. Conceptually, such a model, termed *$s+t$-channel model* in the following, is obtained by adding the two interaction Lagrangians of Eq. (3.24) and Eq. (3.25). As a consequence, one obtains a model which in addition to the parameters of the genuine t-channel model considered previously exhibits the extra parameters of the vector mediator mass M_V, the couplings of the (axial) vector mediator to quarks, $g_q^{V(A)}$, and to DM, $g_\chi^{V(A)}$.

In order to assess the features of such a model, we again use $\lambda = 1$ and fix $M_{\text{med}} = 500$ GeV, but keep m_χ as a free parameter, and set the values of the additional parameters in such a way that the pure s-channel and t-channel contributions are roughly of the same size. In particular, we choose the masses of the two mediator particles and their couplings to the DM particle to be identical, $M_V = M_{\text{med}}$, $g_\chi^{V/A} = 1$, and we set $g_q^{V/A} = \pm 1/8$. Both values of the sign factor in the coupling of the vector mediator to quarks are considered.

When computing DM-nucleon cross sections in the framework of this $s+t$-channel model, we find that the Wilson coefficients c^{s+t} in principle just correspond to the sum of the Wilson coefficients of the pure s- and t-channel models, c^s and c^t, respectively, as detailed in Sec. 7.4.3. Thus, the relevant cross sections are sensitive to a relative minus sign between the two contributions and therefore directly to the sign of the g_q^V or g_q^A couplings. Interestingly, because of the relative minus sign between the two terms at LO, a cancellation occurs which becomes maximal for similar magnitudes of both contributions. At NLO, the cancellation pattern is modified, because of the absence of one-loop corrections in the s-channel model, which we disccused in Sec. 7.4.1. Combined with the non-vanishing loop correction to the t-channel model, the perturbative expansion of the SI and SD cross sections, generically referred to as σ^{pert}, is thus, at the perturbative order we consider, schematically of the form

$$\begin{aligned}\sigma^{\text{pert}} \propto \left|c^{s,\text{tree}} + c^{t,\text{tree}}\right|^2 + 2\mathfrak{R}\Big[\left(c^{s,\text{tree}} + c^{t,\text{tree}}\right)\left(c^{s+t,\text{1-loop}}\right)^\star\Big] \\ + \left|c^{s+t,\text{1-loop}}\right|^2 + \mathcal{O}(\alpha_\text{s}^2),\end{aligned} \tag{7.44}$$

where we have explicitly included the squared one-loop correction which is of order $\mathcal{O}(\alpha_\text{s}^2)$ and thus formally only contributes beyond NLO. Note that we did not include this term in any of the results discussed above. When $|c^{s,\text{tree}} + c^{t,\text{tree}}|$ is small, the interference term between the tree-level and the one-loop contributions as well as the squared one-loop term can become the dominant contribution to the cross section. If the relative sign between $c^{s,\text{tree}}$ and $c^{t,\text{tree}}$ changes, the hierarchy of terms is reversed, and the one-loop correction ceases to be the dominant contribution to the cross section.

Fig. 7.10 illustrates the impact of interference effects for the example of the SI DM-proton cross section, σ_p^{SI}. For a positive sign of the g_q^V coupling, no cancellation effects occur at LO, and the NLO contributions constitute only a small correction to the LO results. However, when the sign of the g_q^V coupling is taken negative, the interference pattern of Eq. (7.44) has a strong impact on the theoretical predictions. Because the LO contribution is artificially small, the interference of the tree-level contributions with the one-loop corrections as well as the squared one-loop term are the dominant contributions at NLO, and much larger than the pure LO result. Consequently, the NLO corrections strongly modify the LO results. It can furthermore be seen that

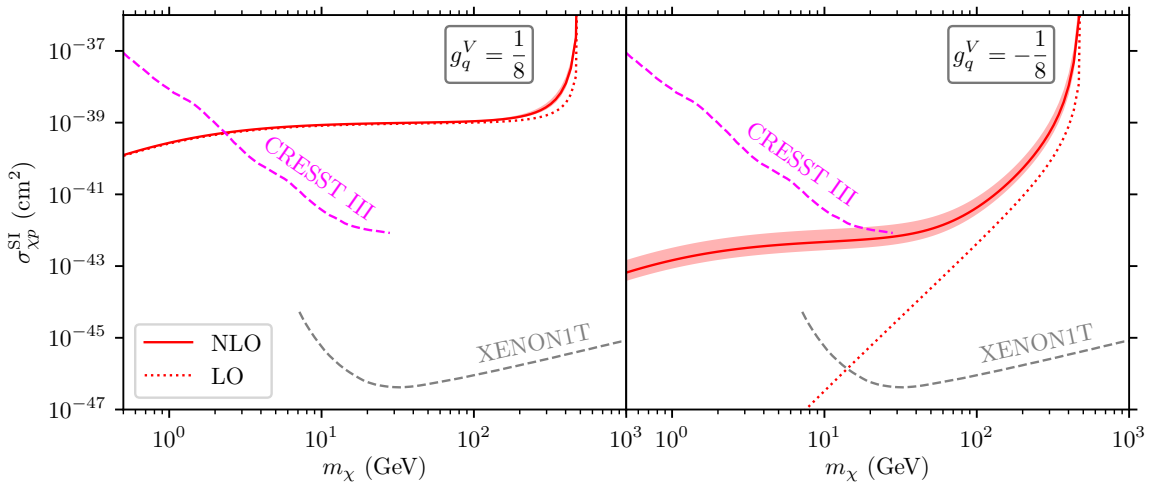

Figure 7.10: Theoretical predictions at LO (dotted blue) and NLO (solid hatched blue area) for σ_p^{SI} together with bounds from CRESST and XENON for an $s+t$-channel model with $g_q^V = 1/8$ (left panel) and $g_q^V = -1/8$ (right panel).

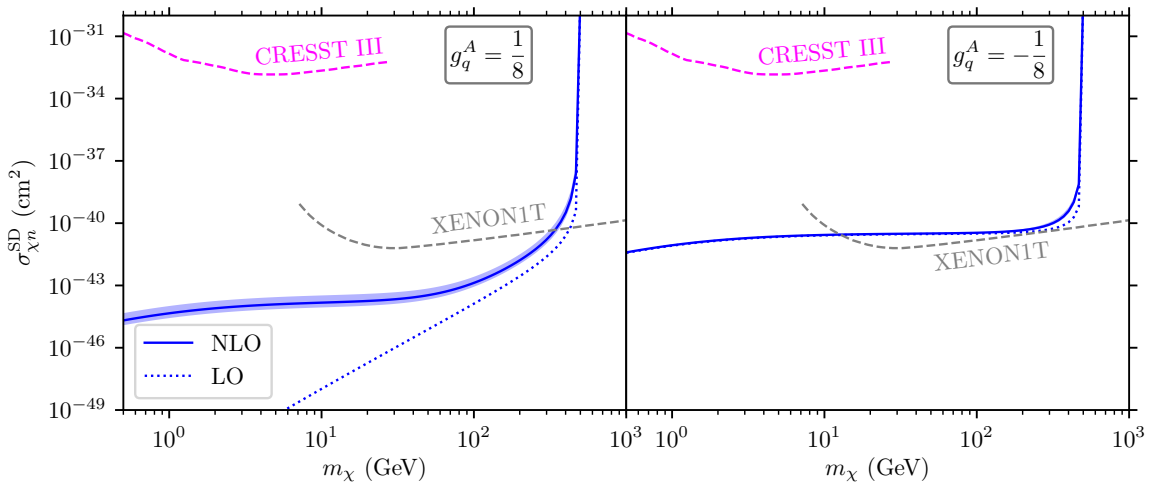

Figure 7.11: Theoretical predictions at LO (dotted blue) and NLO (solid hatched blue area) for σ_n^{SD} together with bounds from CRESST and XENON for an $s+t$-channel model with $g_q^A = 1/8$ (left panel) and $g_q^A = -1/8$ (right panel).

the scale dependence is much more pronounced in the case of a suppression of the LO contribution than in the case of no suppression, denoting a strong perturbative uncertainty and a larger relevance of higher-order effects.

Analogous effects are found for the SD DM-neutron cross section σ_n^{SD}, as shown in Fig. 7.11. We note, however, that due to an opposite sign of the tree-level Wilson coefficient $c_A^{t,\mathrm{tree}}$ compared to $c_V^{t,\mathrm{tree}}$, see Eq. (7.34), the effects are inverted for positive and negative signs of the g_q^A coupling.

Chapter 8

Conclusions

Performing precise calculations for beyond the Standard Model physics might be the key to answer open questions in particle physics and even in astrophysics. We have discussed these open problems and we have linked them to the framework of perturbative quantum field theory.

In Chap. 5, we performed NLO-QCD calculations for weakino-squark production at hadron colliders. We gave an extensive overview of our work, focusing on the most technically challenging aspect, namely the subtraction of on-shell resonances, which are not a genuine part of the NLO QCD corrections. We implemented this process in the framework of the `POWHEG-BOX`, which allows the matching to parton-shower programs. This implementation will be made public at http://powhegbox.mib.infn.it/, thus providing a ready-to-use tool for the experimental and phenomenological communities. We also presented short phenomenological studies, in which we assessed the perturbative stability of our calculation and the relevance of the NLO-QCD corrections. These characteristics depend strongly on the scenario and on the specific process in consideration, but we found that including NLO-QCD corrections leads to a sizeable increase of the cross section, which we found to be around 50% for most of the processes that we considered, and to a reduction of the theoretical uncertainties due to the dependence on the renormalisation and factorisation scale. The latter remain however of around 20%, which is largely due to the large number of quark- and antiquark-induced channels opening up in the real emission corrections. We also performed detailed phenomenological studies, including differential distributions and parton-shower effects, for two SUSY-parameter points in the pMSSM11. We found that, as is to be expected, parton shower effects are more relevant on jet observables than on observables related to the weakinos. In a selected scenario, we included tree-level decays for the SUSY particles.

In Chap. 6, we studied, using our own `POWHEG-BOX` implementations, dark matter pair-production in two simplified models, which we called s- and t-channel simplified models, and we compared the production cross sections and distributions with the ones of pair-production for the lightest neutralino in the MSSM at NLO-QCD. We performed a detailed comparison considering 5000 SUSY parameter space points in two constrained MSSM scenarios, the CMSSM and the pMSSM10. We found that the simplified models are not, in general, capable to fully reproduce the phenomenology of the supersymmetric models. In particular, the neutralino mixing-matrix has a tangible effect on the MSSM phenomenology and the simplified models do not have an equivalent element that can reproduce this behaviour. Comparing the overall cross sections we observed that, exploring the SUSY parameter space, the different mass spectra of the simplified models and of the MSSM lead to large variations of the ratio of the cross sections. Distinct structures are observable, some due to the resonance patterns

of intermediate particles and some due to an effect we called higgsino mixing-matrix suppresion, which is only present in the MSSM. Studying distributions in a few selected SUSY parameter space points we also found that, in some cases, the t-channel simplified model produced results that are very similar to those of the MSSM, in particular considering a Majorana fermion as a DM candidate in the simplified models. These points are the ones in which the lightest neutralino has a negligible higgsino component and is therefore predominantly wino- or bino-like. For wino- and bino-like lightest neutralinos, the relevant topologies are indeed equivalent to those of the simplified t-channel model with a Majorana fermion.

In Chap. 7, we presented NLO-QCD corrections to the dark matter-nucleon scattering cross section in the context of simplified models. We focused on the same s- and t-channel simplified models of the previous chapter. In this case, we also considered the effect of a combined $s+t$-channel model. We matched our results and an effective field theory in the non-relativistic limit. Thus, we obtained NLO-QCD corrections for the Wilson coefficients and effective operators, which are the quantities commonly quoted in the context of direct detection experiments. We provided in this thesis the full expressions for these quantities. We then performed a phenomenological analysis for the t-channel model, as the $\mathcal{O}(\alpha_s)$ corrections to the s-channel model vanish. We discussed the theoretical uncertainties associated with the perturbative treatment used in a low-energy framework and the impact of NLO-QCD corrections on the cross section. Moreover, we compared the constraints on the spin-dependent and spin-independent cross sections set by the LHC and by the direct detection experiments CRESST and XENON. Mono-jet searches from the LHC exclude large regions of parameter space in a model-dependent way, while limits from direct detection experiments do not depend on the specific model. CRESST and XENON, as expected, set complementary limits, as CRESST is more sensitive for low-mass dark matter and XENON to heavier dark matter particles. To conclude, we also studied the phenomenology of a combined $s+t$-channel model, which presents large NLO-QCD corrections when the s- and t-channel contributions interfer destructively at LO.

The research work carried out in this thesis shows, in several different contexts, the relevance of NLO-QCD corrections. In all of these very different frameworks, considering the impact of these corrections is crucial in order to provide accurate predictions. We also found that, while they have limitations, simplified models remain a valuable tool for studying dark matter phenomenology. Diversification, both in terms of the complexity of the models and of the experimental strategies, is very helpful in dark matter searches to cover as much ground as possible in the study of a complex open problem, the solution of which is not yet in sight.

The work of this thesis can be continued in many ways: Predictions for weakino-squark production at hadron colliders can be improved by including NLO-QCD corrections to the decay of unstable supersymmetric particles. Simplified models for dark matter can be modified to include a slightly richer structure, trading some of their simplicity for the possibility of investigating a larger parameter space without yet resorting to a complete theory in all its complexity. Continuing to study the dark matter issue and other open problems in particle physics, studying existing models more precisely and proposing new ones, can only be beneficial.

Bibliography

[1] ATLAS collaboration, G. Aad et al., *Observation of a new particle in the search for the Standard Model Higgs boson with the ATLAS detector at the LHC*, *Phys. Lett. B* **716** (2012) 1 [1207.7214].

[2] S. C. et al., *Observation of a new boson at a mass of 125 GeV with the CMS experiment at the LHC*, *Physics Letters B* **716** (2012) 30.

[3] V. C. Rubin and J. Ford, W. Kent, *Rotation of the Andromeda Nebula from a Spectroscopic Survey of Emission Regions*, *The Astrophysical Journal* **159** (1970) 379.

[4] V. C. Rubin, J. Ford, W. K. and N. Thonnard, *Rotational properties of 21 SC galaxies with a large range of luminosities and radii, from NGC 4605 (R=4kpc) to UGC 2885 (R=122kpc).*, *The Astrophysical Journal* **238** (1980) 471.

[5] W. Tucker, P. Blanco, S. Rappoport, L. David, D. Fabricant, E. E. Falco et al., *1e0657-56: a contender for the hottest known cluster of galaxies*, *Astrophys. J. Lett.* **496** (1998) L5 [astro-ph/9801120].

[6] D. Clowe, A. Gonzalez and M. Markevitch, *Weak-lensing mass reconstruction of the interacting cluster 1e 0657-558: Direct evidence for the existence of dark matter*, *The Astrophysical Journal* **604** (2004) 596.

[7] M. Markevitch, A. H. Gonzalez, D. Clowe, A. Vikhlinin, L. David, W. Forman et al., *Direct constraints on the dark matter self-interaction cross-section from the merging galaxy cluster 1E0657-56*, *Astrophys. J.* **606** (2004) 819 [astro-ph/0309303].

[8] A. Liddle, *An Introduction to Modern Cosmology, 2nd edition*. Wiley, 2013.

[9] V. Springel, S. D. M. White, A. Jenkins, C. S. Frenk, N. Yoshida, L. Gao et al., *Simulations of the formation, evolution and clustering of galaxies and quasars*, *Nature* **435** (2005) 629 [astro-ph/0504097].

[10] A. A. Klypin, S. Trujillo-Gomez and J. Primack, *Dark Matter Halos in the Standard Cosmological Model: Results from the Bolshoi Simulation*, *The Astrophysical Journal* **740** (2011) 102 [1002.3660].

[11] Super-Kamiokande Collaboration collaboration, Y. Fukuda, T. Hayakawa, E. Ichihara, K. Inoue, K. Ishihara, H. Ishino et al., *Evidence for oscillation of atmospheric neutrinos*, *Phys. Rev. Lett.* **81** (1998) 1562.

[12] SNO Collaboration collaboration, Q. R. Ahmad, R. C. Allen, T. C. Andersen, J. D.Anglin, J. C. Barton, E. W. Beier et al., *Direct evidence for*

neutrino flavor transformation from neutral-current interactions in the sudbury neutrino observatory, *Phys. Rev. Lett.* **89** (2002) 011301.

[13] S. Weinberg, *Implications of dynamical symmetry breaking*, *Phys. Rev. D* **13** (1976) 974.

[14] S. Weinberg, *Implications of dynamical symmetry breaking: An addendum*, *Phys. Rev. D* **19** (1979) 1277.

[15] L. Susskind, *Dynamics of spontaneous symmetry breaking in the Weinberg-Salam theory*, *Phys. Rev. D* **20** (1979) 2619.

[16] R. D. Peccei and H. R. Quinn, *CP Conservation in the Presence of Pseudoparticles*, *Phys. Rev. Lett.* **38** (1977) 1440.

[17] R. D. Peccei, *The Strong CP problem and axions*, *Lect. Notes Phys.* **741** (2008) 3 [hep-ph/0607268].

[18] J. Wess and B. Zumino, *Supergauge transformations in four dimensions*, *Nuclear Physics B* **70** (1974) 39.

[19] P. Fayet and S. Ferrara, *Supersymmetry*, *Phys. Rept.* **32** (1977) 249.

[20] J. Baglio, G. Coniglio, B. Jager and M. Spira, *Next-to-leading-order QCD corrections and parton-shower effects for weakino+squark production at the LHC*, 2110.04211.

[21] T. Sjostrand, S. Mrenna and P. Z. Skands, *PYTHIA 6.4 Physics and Manual*, *JHEP* **05** (2006) 026 [hep-ph/0603175].

[22] T. Sjöstrand, S. Ask, J. R. Christiansen, R. Corke, N. Desai, P. Ilten et al., *An introduction to PYTHIA 8.2*, *Comput. Phys. Commun.* **191** (2015) 159 [1410.3012].

[23] P. Nason, *A New method for combining NLO QCD with shower Monte Carlo algorithms*, *JHEP* **11** (2004) 040 [hep-ph/0409146].

[24] S. Frixione, P. Nason and C. Oleari, *Matching NLO QCD computations with Parton Shower simulations: the POWHEG method*, *JHEP* **11** (2007) 070 [0709.2092].

[25] S. Alioli, P. Nason, C. Oleari and E. Re, *A general framework for implementing NLO calculations in shower Monte Carlo programs: the POWHEG BOX*, *JHEP* **06** (2010) 043 [1002.2581].

[26] C. Borschensky, G. Coniglio and B. Jäger, *Dark matter pair production in the MSSM and in simplified dark matter models at the LHC*, *Eur. Phys. J.* **C79** (2019) 428 [1812.08704].

[27] C. Borschensky, G. Coniglio, B. Jäger, J. Jochum and V. Schipperges, *Direct detection of dark matter: Precision predictions in a simplified model framework*, *Eur. Phys. J.* **C81** (2021) 44 [2008.04253].

[28] CRESST collaboration, A. H. Abdelhameed et al., *First results from the CRESST-III low-mass dark matter program*, *Phys. Rev. D* **100** (2019) 102002 [1904.00498].

[29] XENON collaboration, E. Aprile et al., *Dark Matter Search Results from a One Ton-Year Exposure of XENON1T*, *Phys. Rev. Lett.* **121** (2018) 111302 [1805.12562].

[30] S. P. Martin, *A Supersymmetry primer*, *Adv. Ser. Direct. High Energy Phys.* **18** (1998) 1 [hep-ph/9709356].

[31] P. J. E. Peebles and B. Ratra, *The cosmological constant and dark energy*, *Rev. Mod. Phys.* **75** (2003) 559.

[32] P. Hernandez, *Neutrino Physics*, in *8th CERN–Latin-American School of High-Energy Physics*, 2016, 1708.01046, DOI.

[33] S. L. Glashow, *Partial Symmetries of Weak Interactions*, *Nucl. Phys.* **22** (1961) 579.

[34] S. Weinberg, *A model of leptons*, *Phys. Rev. Lett.* **19** (1967) 1264.

[35] S. L. Glashow, J. Iliopoulos and L. Maiani, *Weak interactions with lepton-hadron symmetry*, *Phys. Rev. D* **2** (1970) 1285.

[36] S. Coleman and J. Mandula, *All Possible Symmetries of the S Matrix*, *Phys. Rev.* **159** (1967) 1251.

[37] R. Haag, J. T. Łopuszański and M. Sohnius, *All possible generators of supersymmetries of the S-matrix*, *Nuclear Physics B* **88** (1975) 257.

[38] P. van Nieuwenhuizen, *Supergravity*, *Physics Reports* **68** (1981) 189.

[39] I. J. R. Aitchison, *Supersymmetry and the MSSM: An Elementary introduction*, hep-ph/0505105.

[40] K. A. Intriligator and N. Seiberg, *Lectures on Supersymmetry Breaking*, *Class. Quant. Grav.* **24** (2007) S741 [hep-ph/0702069].

[41] H. Nilles, *Supersymmetry, supergravity and particle physics*, *Physics Reports* **110** (1984) 1.

[42] H. P. Nilles, *Dynamically broken supergravity and the hierarchy problem*, *Physics Letters B* **115** (1982) 193.

[43] P. Fayet and J. Iliopoulos, *Spontaneously broken supergauge symmetries and goldstone spinors*, *Physics Letters B* **51** (1974) 461.

[44] H. E. Haber, *The status of the minimal supersymmetric standard model and beyond*, *Nuclear Physics B - Proceedings Supplements* **62** (1998) 469.

[45] G. R. Farrar and P. Fayet, *Phenomenology of the production, decay, and detection of new hadronic states associated with supersymmetry*, *Physics Letters B* **76** (1978) 575.

[46] R. N. Mohapatra, *Supersymmetry and R-parity: an Overview*, 2015.

[47] J. Ellis, J. L. Evans, A. Mustafayev, N. Nagata and K. A. Olive, *The super-GUT CMSSM revisited*, *The European Physical Journal C* **76** (2016) .

[48] K. J. de Vries, E. A. Bagnaschi, O. Buchmueller, R. Cavanaugh, M. Citron, A. De Roeck et al., *The pMSSM10 after LHC run 1*, *The European Physical Journal C* **75** (2015) .

[49] E. Bagnaschi et al., *Likelihood Analysis of the pMSSM11 in Light of LHC 13-TeV Data*, *Eur. Phys. J. C* **78** (2018) 256 [1710.11091].

[50] "ATLAS experiment public results on Supersymmetry searches." https://twiki.cern.ch/twiki/bin/view/AtlasPublic/SupersymmetryPublicResults.

[51] "CMS Supersymmetry physics results." https://twiki.cern.ch/twiki/bin/view/CMSPublic/PhysicsResultsSUS.

[52] ATLAS Collaboration collaboration, *SUSY Summary Plots June 2021*, tech. rep., CERN, Geneva, Jun, 2021.

[53] CMS collaboration, A. M. Sirunyan et al., *Searches for physics beyond the standard model with the variable in hadronic final states with and without disappearing tracks in proton-proton collisions at 13 TeV*, *Eur. Phys. J. C* **80** (2020) 3 [1909.03460].

[54] J. de Swart, G. Bertone and J. van Dongen, *How Dark Matter Came to Matter*, *Nature Astron.* **1** (2017) 0059 [1703.00013].

[55] T. S. van Albada, J. N. Bahcall, K. Begeman and R. Sancisi, *Distribution of dark matter in the spiral galaxy NGC 3198.*, *The Astrophysical Journal* **295** (1985) 305.

[56] A. Einstein, *Lens-like action of a star by the deviation of light in the gravitational field*, *Science* **84** (1936) 506 [https://science.sciencemag.org/content/84/2188/506.full.pdf].

[57] P. L. Kelly et al., *Extreme magnification of an individual star at redshift 1.5 by a galaxy-cluster lens*, *Nature Astron.* **2** (2018) 334 [1706.10279].

[58] "Abell 2218." esahubble.org/images/heic0814a/.

[59] M. Bradac, S. W. Allen, T. Treu, H. Ebeling, R. Massey, R. G. Morris et al., *Revealing the properties of dark matter in the merging cluster MACSJ0025.4-1222*, *Astrophys. J.* **687** (2008) 959 [0806.2320].

[60] M. Girardi, R. Barrena, W. Boschin and E. Ellingson, *Cluster Abell 520: a perspective based on member galaxies. A cluster forming at the crossing of three filaments?*, *Astron. Astrophys.* **491** (2008) 379 [0809.3139].

[61] G. W. Angus and S. S. McGaugh, *The collision velocity of the bullet cluster in conventional and modified dynamics*, *Monthly Notices of the Royal Astronomical Society* **383** (2007) 417.

[62] https://apod.nasa.gov/apod/ap060824.html.

[63] Supernova Cosmology Project collaboration, S. Perlmutter et al., *Measurements of* Ω *and* Λ *from 42 high redshift supernovae*, *Astrophys. J.* **517** (1999) 565 [astro-ph/9812133].

[64] SDSS collaboration, D. J. Eisenstein et al., *Detection of the Baryon Acoustic Peak in the Large-Scale Correlation Function of SDSS Luminous Red Galaxies*, *Astrophys. J.* **633** (2005) 560 [astro-ph/0501171].

[65] G. Hinshaw, D. Larson, E. Komatsu, D. N. Spergel, C. L. Bennett, J. Dunkley et al., *Nine-year Wilkinson microwave anisotropy probe (WMAP) observations: cosmological parameters reuslts*, *The Astrophysical Journal Supplement Series* **208** (2013) 19.

[66] Planck collaboration, P. A. R. Ade et al., *Planck 2015 results. XIII. Cosmological parameters*, *Astron. Astrophys.* **594** (2016) A13 [1502.01589].

[67] Planck collaboration, N. Aghanim et al., *Planck 2018 results. VI. Cosmological parameters*, *Astron. Astrophys.* **641** (2020) A6 [1807.06209].

[68] J. F. Navarro, C. S. Frenk and S. D. M. White, *The Structure of Cold Dark Matter Halos*, *The Astrophysical Journal* **462** (1996) 563 [astro-ph/9508025].

[69] A. Klypin, A. V. Kravtsov, O. Valenzuela and F. Prada, *Where are the missing galactic satellites?*, *The Astrophysical Journal* **522** (1999) 82.

[70] M. Milgrom, *A modification of the Newtonian dynamics as a possible alternative to the hidden mass hypothesis.*, *The Astrophysical Journal* **270** (1983) 365.

[71] J. Bekenstein and M. Milgrom, *Does the missing mass problem signal the breakdown of Newtonian gravity?*, *The Astrophysical Journal* **286** (1984) 7.

[72] J. D. Bekenstein, *Relativistic gravitation theory for the modified newtonian dynamics paradigm*, *Phys. Rev. D* **70** (2004) 083509.

[73] G. Mamon, F. Combes, C. Deffayet, B. Fort, J. Bekenstein and R. Sanders, *A primer to relativistic mond theory*, *European Astronomical Society Publications Series* **20** (2006) 225–230.

[74] M. Bauer and T. Plehn, *Yet Another Introduction to Dark Matter: The Particle Physics Approach*, vol. 959 of *Lecture Notes in Physics*. Springer, 2019, 10.1007/978-3-030-16234-4, [1705.01987].

[75] G. R. Blumenthal, S. M. Faber, J. R. Primack and M. J. Rees, *Formation of galaxies and large-scale structure with cold dark matter.*, *Nature* **311** (1984) 517.

[76] Tisserand, P., Le Guillou, L., Afonso, C., Albert, J. N., Andersen, J., Ansari, R. et al., *Limits on the Macho content of the Galactic Halo from the EROS-2 Survey of the Magellanic Clouds ****, *A&A* **469** (2007) 387.

[77] M. Hawkins, *A new look at microlensing limits on dark matter in the galactic halo*, *Astronomy & Astrophysics* **575** (2015) .

[78] G. Bélanger, F. Boudjema, A. Pukhov and A. Semenov, *Dark matter direct detection rate in a generic model with micrOMEGAs 2.2*, *Comput. Phys. Commun.* **180** (2009) 747 [0803.2360].

[79] G. Bélanger, F. Boudjema, A. Goudelis, A. Pukhov and B. Zaldivar, *micrOMEGAs5.0 : Freeze-in*, *Comput. Phys. Commun.* **231** (2018) 173 [1801.03509].

[80] F. Ambrogi, C. Arina, M. Backovic, J. Heisig, F. Maltoni, L. Mantani et al., *MadDM v.3.0: a Comprehensive Tool for Dark Matter Studies*, *Phys. Dark Univ.* **24** (2019) 100249 [1804.00044].

[81] T. Bringmann, J. Edsjö, P. Gondolo, P. Ullio and L. Bergström, *DarkSUSY 6 : An Advanced Tool to Compute Dark Matter Properties Numerically*, *JCAP* **07** (2018) 033 [1802.03399].

[82] J. Ipser and P. Sikivie, *Can galactic halos be made of axions?*, *Phys. Rev. Lett.* **50** (1983) 925.

[83] L. Bergström, *Dark matter candidates*, *New Journal of Physics* **11** (2009) 105006 [0903.4849].

[84] J. Abdallah, H. Araujo, A. Arbey, A. Ashkenazi, A. Belyaev, J. Berger et al., *Simplified Models for Dark Matter Searches at the LHC*, *Phys. Dark Universe* **9-10** (2015) 8 [1506.03116].

[85] D. Binosi and L. Theussl, *JaxoDraw: A Graphical user interface for drawing Feynman diagrams*, *Comput. Phys. Commun.* **161** (2004) 76 [hep-ph/0309015].

[86] D. Binosi, J. Collins, C. Kaufhold and L. Theussl, *JaxoDraw: A Graphical user interface for drawing Feynman diagrams. Version 2.0 release notes*, *Comput. Phys. Commun.* **180** (2009) 1709 [0811.4113].

[87] E. Dudas, Y. Mambrini, S. Pokorski and A. Romagnoni, *(In)visible Z-prime and dark matter*, *JHEP* **08** (2009) 014 [0904.1745].

[88] D. Abercrombie et al., *Dark Matter Benchmark Models for Early LHC Run-2 Searches: Report of the ATLAS/CMS Dark Matter Forum*, 1507.00966.

[89] P. Ko, A. Natale, M. Park and H. Yokoya, *Simplified DM models with the full SM gauge symmetry : the case of t-channel colored scalar mediators*, *JHEP* **01** (2017) 086 [1605.07058].

[90] M. A. Ajaib and I. Gogoladze, *Status Update on Selective SUSY GUT Inspired Models*, 1710.07842.

[91] PAMELA collaboration, O. Adriani et al., *Ten years of PAMELA in space*, *Riv. Nuovo Cim.* **40** (2017) 473 [1801.10310].

[92] ANTARES collaboration, A. Albert et al., *Search for dark matter towards the Galactic Centre with 11 years of ANTARES data*, *Phys. Lett. B* **805** (2020) 135439 [1912.05296].

[93] L. Goodenough and D. Hooper, *Possible Evidence For Dark Matter Annihilation In The Inner Milky Way From The Fermi Gamma Ray Space Telescope*, 0910.2998.

[94] LUX collaboration, D. S. Akerib et al., *Results from a search for dark matter in the complete LUX exposure*, *Phys. Rev. Lett.* **118** (2017) 021303 [1608.07648].

[95] ATLAS collaboration, M. Aaboud et al., *Search for dark matter and other new phenomena in events with an energetic jet and large missing transverse momentum using the ATLAS detector*, *JHEP* **01** (2018) 126 [1711.03301].

[96] G. Busoni et al., *Recommendations on presenting LHC searches for missing transverse energy signals using simplified s-channel models of dark matter*, *Phys. Dark Univ.* **27** (2020) 100365 [1603.04156].

[97] J. C. Collins, D. E. Soper and G. F. Sterman, *Factorization of Hard Processes in QCD*, *Adv. Ser. Direct. High Energy Phys.* **5** (1989) 1 [hep-ph/0409313].

[98] G. Munster and M. Walzl, *Lattice gauge theory: A Short primer*, in *Zuoz Summer School on Phenomenology of Gauge Interactions*, 8, 2000, hep-lat/0012005.

[99] H. Lehmann, K. Symanzik and W. Zimmermann, *Zur Formulierung quantisierter Feldtheorien*, *Nuovo Cimento Serie* **1** (1955) 205.

[100] R. P. Feynman, *Space-time approach to quantum electrodynamics*, *Phys. Rev.* **76** (1949) 769.

[101] T. Kinoshita, *Mass singularities of Feynman amplitudes*, *Journal of Mathematical Physics* **3** (1962) 650.

[102] T. D. Lee and M. Nauenberg, *Degenerate systems and mass singularities*, *Phys. Rev.* **133** (1964) B1549.

[103] G. 't Hooft and M. Veltman, *Regularization and renormalization of gauge fields*, *Nuclear Physics B* **44** (1972) 189.

[104] D. Capper, D. Jones and P. Van Nieuwenhuizen, *Regularization by dimensional reduction of supersymmetric and non-supersymmetric gauge theories*, *Nuclear Physics B* **167** (1980) 479.

[105] W. Siegel, *Supersymmetric dimensional regularization via dimensional reduction*, *Physics Letters B* **84** (1979) 193.

[106] G. 't Hooft, *Lattice regularization of gauge theories without loss of chiral symmetry*, *Phys. Lett. B* **349** (1995) 491 [hep-th/9411228].

[107] W. Pauli and F. Villars, *On the invariant regularization in relativistic quantum theory*, *Rev. Mod. Phys.* **21** (1949) 434.

[108] G. 'tHooft, *Renormalization of massless yang-mills fields*, *Nuclear Physics B* **33** (1971) 173.

[109] G. Hooft, *Renormalizable lagrangians for massive yang-mills fields*, *Nuclear Physics B* **35** (1971) 167.

[110] A. Denner, *Techniques for calculation of electroweak radiative corrections at the one loop level and results for W physics at LEP-200*, *Fortsch. Phys.* **41** (1993) 307 [0709.1075].

[111] G. 't Hooft, *Dimensional regularization and the renormalization group*, *Nuclear Physics B* **61** (1973) 455.

[112] W. A. Bardeen, A. J. Buras, D. W. Duke and T. Muta, *Deep-inelastic scattering beyond the leading order in asymptotically free gauge theories*, *Phys. Rev. D* **18** (1978) 3998.

[113] J. Baglio, B. Jäger and M. Kesenheimer, *Precise predictions for electroweakino-pair production in association with a jet at the LHC*, *JHEP* **07** (2018) 055 [1711.00730].

[114] G. Prosperi, M. Raciti and C. Simolo, *On the running coupling constant in qcd*, *Progress in Particle and Nuclear Physics* **58** (2007) 387.

[115] W. Beenakker, R. Hopker, M. Spira and P. M. Zerwas, *Squark and gluino production at hadron colliders*, *Nucl. Phys. B* **492** (1997) 51 [hep-ph/9610490].

[116] L. Landau, *On analytic properties of vertex parts in quantum field theory*, *Nuclear Physics* **13** (1959) 181.

[117] S. Catani and M. H. Seymour, *A General algorithm for calculating jet cross-sections in NLO QCD*, *Nucl. Phys. B* **485** (1997) 291 [hep-ph/9605323].

[118] B. W. Harris and J. F. Owens, *The Two cutoff phase space slicing method*, *Phys. Rev. D* **65** (2002) 094032 [hep-ph/0102128].

[119] A. Gehrmann-De Ridder, T. Gehrmann and E. W. N. Glover, *Antenna subtraction at NNLO*, *JHEP* **09** (2005) 056 [hep-ph/0505111].

[120] A. Daleo, T. Gehrmann and D. Maitre, *Antenna subtraction with hadronic initial states*, *JHEP* **04** (2007) 016 [hep-ph/0612257].

[121] S. Frixione, Z. Kunszt and A. Signer, *Three jet cross-sections to next-to-leading order*, *Nucl. Phys. B* **467** (1996) 399 [hep-ph/9512328].

[122] S. Frixione, *A General approach to jet cross-sections in QCD*, *Nucl. Phys. B* **507** (1997) 295 [hep-ph/9706545].

[123] A. Buckley, J. Butterworth, S. Gieseke, D. Grellscheid, S. Höche, H. Hoeth et al., *General-purpose event generators for LHC physics*, *Physics Reports* **504** (2011) 145.

[124] S. Frixione and B. R. Webber, *Matching NLO QCD computations and parton shower simulations*, *JHEP* **06** (2002) 029 [hep-ph/0204244].

[125] C. Oleari, *The POWHEG-BOX*, *Nucl. Phys. B Proc. Suppl.* **205-206** (2010) 36 [1007.3893].

[126] P. Nason, *MINT: A Computer program for adaptive Monte Carlo integration and generation of unweighted distributions*, 0709.2085.

[127] J. Alwall et al., *A Standard format for Les Houches event files*, *Comput. Phys. Commun.* **176** (2007) 300 [hep-ph/0609017].

[128] R. Gavin, C. Hangst, M. Krämer, M. Mühlleitner, M. Pellen, E. Popenda et al., *Matching Squark Pair Production at NLO with Parton Showers*, *JHEP* **10** (2013) 187 [1305.4061].

[129] R. Gavin, C. Hangst, M. Krämer, M. Mühlleitner, M. Pellen, E. Popenda et al., *Squark Production and Decay matched with Parton Showers at NLO*, *Eur. Phys. J. C* **75** (2015) 29 [1407.7971].

[130] J. Baglio, B. Jäger and M. Kesenheimer, *Electroweakino pair production at the LHC: NLO SUSY-QCD corrections and parton-shower effects*, *JHEP* **07** (2016) 083 [1605.06509].

[131] H. Murayama, I. Watanabe and K. Hagiwara, *HELAS: HELicity amplitude subroutines for Feynman diagram evaluations*, Tech. Rep. KEK-91-11, 1992.

[132] T. Stelzer and W. F. Long, *Automatic generation of tree level helicity amplitudes*, *Comput. Phys. Commun.* **81** (1994) 357 [hep-ph/9401258].

[133] J. Alwall, P. Demin, S. de Visscher, R. Frederix, M. Herquet, F. Maltoni et al., *MadGraph/MadEvent v4: The New Web Generation*, *JHEP* **09** (2007) 028 [0706.2334].

[134] T. Hahn, *Generating Feynman diagrams and amplitudes with FeynArts 3*, *Comput. Phys. Commun.* **140** (2001) 418 [hep-ph/0012260].

[135] T. Hahn and M. Perez-Victoria, *Automatized one loop calculations in four-dimensions and D-dimensions*, *Comput. Phys. Commun.* **118** (1999) 153 [hep-ph/9807565].

[136] T. Fritzsche, T. Hahn, S. Heinemeyer, F. von der Pahlen, H. Rzehak and C. Schappacher, *The Implementation of the Renormalized Complex MSSM in FeynArts and FormCalc*, *Comput. Phys. Commun.* **185** (2014) 1529 [1309.1692].

[137] W. Hollik and D. Stockinger, *Regularization and supersymmetry restoring counterterms in supersymmetric QCD*, *Eur. Phys. J. C* **20** (2001) 105 [hep-ph/0103009].

[138] S. P. Martin and M. T. Vaughn, *Regularization dependence of running couplings in softly broken supersymmetry*, *Phys. Lett. B* **318** (1993) 331 [hep-ph/9308222].

[139] W. Beenakker, M. Klasen, M. Kramer, T. Plehn, M. Spira and P. M. Zerwas, *The Production of charginos / neutralinos and sleptons at hadron colliders*, *Phys. Rev. Lett.* **83** (1999) 3780 [hep-ph/9906298].

[140] E. Re, *Single-top Wt-channel production matched with parton showers using the POWHEG method*, *Eur. Phys. J. C* **71** (2011) 1547 [1009.2450].

[141] D. Berdine, N. Kauer and D. Rainwater, *Breakdown of the Narrow Width Approximation for New Physics*, *Phys. Rev. Lett.* **99** (2007) 111601 [hep-ph/0703058].

[142] S. Catani, S. Dittmaier, M. H. Seymour and Z. Trocsanyi, *The Dipole formalism for next-to-leading order QCD calculations with massive partons*, *Nucl. Phys. B* **627** (2002) 189 [hep-ph/0201036].

[143] W. Beenakker, R. Hopker and M. Spira, *PROSPINO: A Program for the production of supersymmetric particles in next-to-leading order QCD*, hep-ph/9611232.

[144] W. Beenakker, R. Höpker, M. Spira and P. M. Zerwas, *Squark production at the Tevatron*, *Phys. Rev. Lett.* **74** (1995) 2905 [hep-ph/9412272].

[145] W. Beenakker, R. Höpker, M. Spira and P. M. Zerwas, *Gluino pair production at the Tevatron*, *Z. Phys. C* **69** (1995) 163 [hep-ph/9505416].

[146] W. Beenakker, M. Krämer, T. Plehn, M. Spira and P. M. Zerwas, *Stop production at hadron colliders*, *Nucl. Phys. B* **515** (1998) 3 [hep-ph/9710451].

[147] M. Spira, *Higgs and SUSY particle production at hadron colliders*, in *10th International Conference on Supersymmetry and Unification of Fundamental Interactions (SUSY02)*, pp. 217–226, 11, 2002, hep-ph/0211145.

[148] T. Binoth, D. Goncalves Netto, D. Lopez-Val, K. Mawatari, T. Plehn and I. Wigmore, *Automized Squark-Neutralino Production to Next-to-Leading Order*, *Phys. Rev. D* **84** (2011) 075005 [1108.1250].

[149] Muon g-2 collaboration, G. W. Bennett et al., *Measurement of the negative muon anomalous magnetic moment to 0.7 ppm*, *Phys. Rev. Lett.* **92** (2004) 161802 [hep-ex/0401008].

[150] Muon g-2 collaboration, G. W. Bennett et al., *Final Report of the Muon E821 Anomalous Magnetic Moment Measurement at BNL*, *Phys. Rev. D* **73** (2006) 072003 [hep-ex/0602035].

[151] Muon g-2 collaboration, B. Abi et al., *Measurement of the Positive Muon Anomalous Magnetic Moment to 0.46 ppm*, *Phys. Rev. Lett.* **126** (2021) 141801 [2104.03281].

[152] S. Dulat, T.-J. Hou, J. Gao, M. Guzzi, J. Huston, P. Nadolsky et al., *New parton distribution functions from a global analysis of quantum chromodynamics*, *Phys. Rev. D* **93** (2016) 033006 [1506.07443].

[153] A. Buckley, J. Ferrando, S. Lloyd, K. Nordström, B. Page, M. Rüfenacht et al., *LHAPDF6: parton density access in the LHC precision era*, *Eur. Phys. J. C* **75** (2015) 132 [1412.7420].

[154] M. Cacciari, G. P. Salam and G. Soyez, *The anti-k_t jet clustering algorithm*, *JHEP* **04** (2008) 063 [0802.1189].

[155] http://powhegbox.mib.infn.it.

[156] Particle Data Group collaboration, M. Tanabashi, K. Hagiwara, K. Hikasa, K. Nakamura, Y. Sumino, F. Takahashi et al., *Review of particle physics*, *Phys. Rev. D* **98** (2018) 030001.

[157] M. Backović, M. Krämer, F. Maltoni, A. Martini, K. Mawatari and M. Pellen, *Higher-order QCD predictions for dark matter production at the LHC in simplified models with s-channel mediators*, *Eur. Phys. J. C* **75** (2015) 482 [1508.05327].

[158] A. Denner, S. Dittmaier and L. Hofer, *Collier: a fortran-based Complex One-Loop LIbrary in Extended Regularizations*, *Comput. Phys. Commun.* **212** (2017) 220 [1604.06792].

[159] A. Denner and S. Dittmaier, *Reduction of one loop tensor five point integrals*, *Nucl. Phys.* **B658** (2003) 175 [hep-ph/0212259].

[160] A. Denner and S. Dittmaier, *Reduction schemes for one-loop tensor integrals*, *Nucl. Phys.* **B734** (2006) 62 [hep-ph/0509141].

[161] W. Porod, *SPheno, a program for calculating supersymmetric spectra, SUSY particle decays and SUSY particle production at e+ e- colliders*, *Comput. Phys. Commun.* **153** (2003) 275 [hep-ph/0301101].

[162] W. Porod and F. Staub, *SPheno 3.1: Extensions including flavour, CP-phases and models beyond the MSSM*, *Comput. Phys. Commun.* **183** (2012) 2458 [1104.1573].

[163] A. Albert et al., *Recommendations of the LHC Dark Matter Working Group: Comparing LHC searches for dark matter mediators in visible and invisible decay channels and calculations of the thermal relic density*, *Phys. Dark Univ.* **26** (2019) 100377 [1703.05703].

[164] J. Butterworth et al., *PDF4LHC recommendations for LHC Run II*, *J. Phys. G* **43** (2016) 023001 [1510.03865].

[165] M. Cacciari and G. P. Salam, *Dispelling the N^3 myth for the k_t jet-finder*, *Phys. Lett. B* **641** (2006) 57 [hep-ph/0512210].

[166] M. Cacciari, G. P. Salam and G. Soyez, *FastJet User Manual*, *Eur. Phys. J. C* **72** (2012) 1896 [1111.6097].

[167] J. Rosiek, *Complete Set of Feynman Rules for the Minimal Supersymmetric Extension of the Standard Model*, *Phys. Rev.* **D41** (1990) 3464.

[168] J. Rosiek, *Complete set of Feynman rules for the MSSM: Erratum*, hep-ph/9511250.

[169] T. Lin, *Dark matter models and direct detection*, *PoS* **333** (2019) 009 [1904.07915].

[170] M. Schumann, *Direct Detection of WIMP Dark Matter: Concepts and Status*, *J. Phys. G* **46** (2019) 103003 [1903.03026].

[171] K. R. Dienes, J. Kumar, B. Thomas and D. Yaylali, *Overcoming Velocity Suppression in Dark-Matter Direct-Detection Experiments*, *Phys. Rev. D* **90** (2014) 015012 [1312.7772].

[172] M. Klasen, K. Kovarik and P. Steppeler, *SUSY-QCD corrections for direct detection of neutralino dark matter and correlations with relic density*, *Phys. Rev.* **D94** (2016) 095002 [1607.06396].

[173] M. Fierz, *Zur Fermischen Theorie des β-Zerfalls*, *Zeitschrift fur Physik* **104** (1937) 553.

[174] J. B. Dent, L. M. Krauss, J. L. Newstead and S. Sabharwal, *General analysis of direct dark matter detection: From microphysics to observational signatures*, *Phys. Rev. D* **92** (2015) 063515 [1505.03117].

[175] M. Drees and M. M. Nojiri, *New contributions to coherent neutralino - nucleus scattering*, *Phys. Rev. D* **47** (1993) 4226 [hep-ph/9210272].

[176] M. Drees and M. Nojiri, *Neutralino - nucleon scattering revisited*, *Phys. Rev. D* **48** (1993) 3483 [hep-ph/9307208].

[177] J. Hisano, K. Ishiwata and N. Nagata, *Gluon contribution to the dark matter direct detection*, *Phys. Rev. D* **82** (2010) 115007 [1007.2601].

[178] J. Hisano, R. Nagai and N. Nagata, *Effective Theories for Dark Matter Nucleon Scattering*, *JHEP* **05** (2015) 037 [1502.02244].

[179] J. Hisano, K. Ishiwata and N. Nagata, *QCD Effects on Direct Detection of Wino Dark Matter*, *JHEP* **06** (2015) 097 [1504.00915].

[180] R. Mertig, M. Bohm and A. Denner, *FEYN CALC: Computer algebraic calculation of Feynman amplitudes*, *Comput. Phys. Commun.* **64** (1991) 345.

[181] V. Shtabovenko, R. Mertig and F. Orellana, *New Developments in FeynCalc 9.0*, *Comput. Phys. Commun.* **207** (2016) 432 [1601.01167].

[182] V. Shtabovenko, R. Mertig and F. Orellana, *FeynCalc 9.3: New features and improvements*, 2001.04407.

[183] H. H. Patel, *Package-X: A Mathematica package for the analytic calculation of one-loop integrals*, *Comput. Phys. Commun.* **197** (2015) 276 [1503.01469].

[184] Particle Data Group collaboration, Zyla, P. A. et al., *The Review of Particle Physics*, *to be published in Prog. Theor. Exp. Phys. 2020,* **083C01** (2020) .

[185] R. J. Hill and M. P. Solon, *Standard Model anatomy of WIMP dark matter direct detection II: QCD analysis and hadronic matrix elements*, *Phys. Rev. D* **91** (2015) 043505 [1409.8290].

[186] XENON collaboration, E. Aprile et al., *Constraining the spin-dependent WIMP-nucleon cross sections with XENON1T*, *Phys. Rev. Lett.* **122** (2019) 141301 [1902.03234].

Acknowledgements

At the end of this long journey, there are many people I would like to thank. First and foremost, I would like to thank my supervisor Prof. Dr. Barbara Jäger. I am very grateful to her for giving me the opportunity to join her research group to work with her and her great team. Her support has been constant and complete in all scientific and administrative matters. I have learned a great deal from her in a field in which I entered in a quite unconventional way, which made her teachings even more important.

I would like to thank Prof. Dr. Werner Vogelsang for accepting to be my second supervisor and to grade this work. I have enjoyed a lot many nice conversations about physics, running and many other topics. I am grateful to Prof. Dr. Thomas Gutsche for the instructive opportunity to be a tutor in his classes and for telling me many interesting stories and anecdotes about almost everything.

I want to express my gratitude to Dr. Michael Spira for his collaboration on the weakino-squark project. His expertise in Supersymmetry has helped me gain a much deeper understanding of my own work and I always felt encouraged to ask questions.

I want to thank Dr. Christoph Borschensky for his patient guidance during our dark matter projects and for dealing with so many of my questions and doubts. His mentoring role during my years at the Institute of Theoretical Physics has been fundamental. Moreover, I am very happy to have shared a lot of time with him in these years and that he has been here for the entirety of the time I spent in Tübingen.

I am grateful to Dr. Julien Baglio for being a very helpful supervisor in the weakino-squark project and for helping me with his theoretical and technical knowledge anytime I had any issues in my work. I also thank him for many nice moments together discussing football and, occasionally, other things.

I would like to thank Dr. Matthias Kesenheimer for the great times we had in our office and for his unvaluable help in the early stages of my PhD, when he shared with me his great knowledge of the tools I would use in the following years. It was also a great pleasure to share the office, many nice discussions and a lot of Italianness with Dr. Margherita Ghezzi. I am very grateful to Johannes Scheller and Santiago Lopez for being great colleagues and for many enjoyable memories that I will always cherish.

I would also like to thank Ingrid Estiry for all the help with the bureaucracy and for being always kind and available.

I am grateful to the many people who made working in the Institute of Theoretical Physics an unforgettable experience, including Maurizio Abele, Jun.-Prof. Dr. Jan Burde, Dr. Davide Campagnari, Robin Feser, Melih Gül, Dr. Ilkka Helenius, Dr. Felix Hekhorn, Felix Kunzelmann, Dr. Martin Lambertsen, Felix Reichenbach, Dr. Marco Stratmann and Dr. Marina Walt. My heartfelt apologies go to those I am inevitably forgetting.

I am very grateful to my mother and sister for their support despite the great distance. Finally, these years would have been very difficult without the support and company of Nadia in the many adventures we shared over these years.